Adjustable Energy Saving Device for Transom Stern Hulls

Rachit P. Salian

Thesis submitted to the faculty of the Virginia Polytechnic Institute and State University in partial fulfillment of the requirements for the degree of

Master of Science
In
Mechanical Engineering

Stefano Brizzolara, Chair
Alexander Leonessa
John A Palmore Jr.

February 25, 2019
Blacksburg, Virginia

Keywords: CFD, Marine Hydrodynamics, Energy saving devices, Adjustable stern appendages, Transom stern flow, Drag reduction, Interceptor

Adjustable Energy Saving Device for Transom Stern Hulls

Rachit Salian

ABSTRACT

The study presents a numerical investigation about the hydrodynamic characteristics of a transom mounted interceptor on the Oliver Hazard Perry class frigate (FFG-7), in order to assess the potential of propulsion power reduction in a wide range of speeds. This study is aimed to design a stern interceptor with optimal efficiency not only at top speed, but also cruising/transfer speeds, by a simple regulation of its variable geometrical characteristics (from a construction and operational standpoint). A high fidelity numerical model is developed in the open source CFD suite OpenFOAM for the prediction of the longitudinal dynamic equilibrium at speed and the total resistance characteristics of the bare hull. The Reynolds Averaged Navier-Stokes Equations are solved using interDyMFoam, a multiphase volume of fluid solver which allows for a dynamic mesh. The numerical model is validated using the results of the experimental model tests conducted on a $1/80^{th}$ scale model at the United States Naval Academy Hydromechanics Laboratory (NAHL).

The validated numerical model is used to predict the hydrodynamic characteristics of the transom mounted interceptor at different interceptor settings and speeds. The results show that the interceptor reduces the amount of resistance, the running trim, and the sinkage of the ship at high speeds. For a speed of 0.392 Froude number (Fr), a drag reduction of 3.76% was observed, as well as a significant reduction in trim.

Adjustable Energy Saving Device for Transom Stern Hulls

Rachit Salian

GENERAL AUDIENCE ABSTRACT

The drag acting on the hull is an important component that has to be considered during the process of designing the ship. An interceptor is a device that has been developed to improve the performance of hulls by reducing the drag. This research studies the influence of the interceptor on the resistance and motion of the ship across a range of speeds. The geometrical characteristics of the interceptor are varied in order to identify the geometry that would provide optimal performance across the speed range tested.

This study is conducted using the Computational Fluid Dynamics (CFD) software OpenFOAM as well as model tests that were conducted on a $1/80^{th}$ scale model.

CONTENTS

CHAPTER 1

INTRODUCTION

The drag acting on the hull is an important component that has to be considered during the process of designing the ship. Various devices have been developed to improve the performance of hulls by reducing the drag. These devices include stern appendages such as stern wedges, interceptors, vanes and trim tabs. It is well known that the use of fixed stern appendages such as stern wedges or stern flaps (Figure 1-1) can improve the resistance and propulsion efficiency of high speed naval vessels with transom stern. The Maestrale class frigate, commissioned in 1981 by the Italian Navy [1] [2], was the first example of modern transom stern naval vessel to show the advantages of a fixed stern wedge. In the '80s, US Navy started a comprehensive program to investigate the effect of stern wedges [3] [4], which more recently evolved in stern flaps [5] or integrated solutions [6]. These fixed stern appendages, optimized for the high-speed range, show significant powering reductions there, while unfortunately generate a less desirable power increase at lower speed.

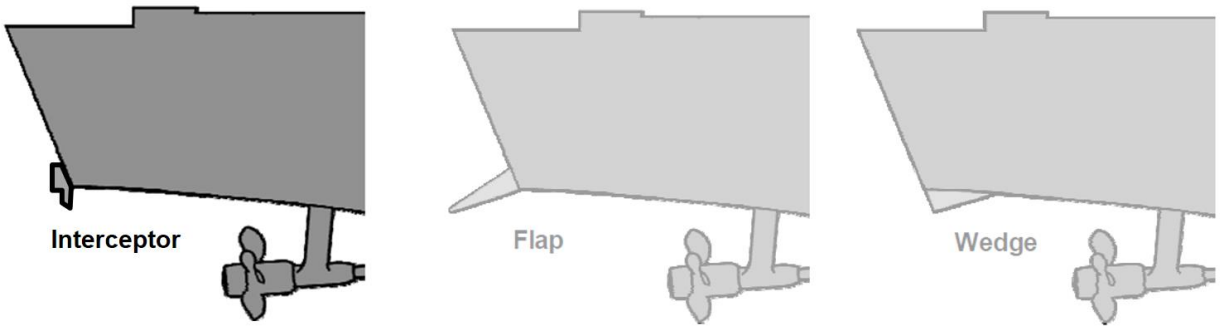

Figure 1-1: Different types of stern appendages

More recently, the use of adjustable stern devices, such as interceptors movable flaps or stern hydrofoils, has been documented also in the case of high speed displacement vessels [7] [8] [9]. These types of devices were introduced first on planing hulls or semi-displacement crafts to correct the dynamic trim and sinkage experienced close or at the hump speed and their design have to be adapted modified and adapted in case of displacement hull forms.

The bare hull resistance and effects of the interceptor on the FFG-7 hull are predicted in this study by CFD using OpenFOAM, as well as with model towing tank tests. OpenFOAM is used to run numerical simulations on a $1/80^{th}$ scaled bare hull model that predicts the behavior in the same conditions as would be observed in towing tank model tests. Model towing tank tests are conducted with the $1/80^{th}$ scaled bare hull model to calculate the resistance coefficients and the hull motion parameters such as the trim and sinkage. The results from the model tests are then used to validate the CFD results obtained in OpenFOAM. After validation, CFD and model tests are run for the hull model with a transom mounted interceptor to observe the changes in the resistance and sailing attitude.

1.1 Stern Energy Saving Devices. State of the art

Over the years, naval architects have developed several stern appendages to reduce the drag on the hull, which is achieved by creating a lift component acting on the hull. Karafiath and Fisher (1987) [15], suggested that the concept of stern appendages, namely stern wedges was implemented by the Italian, US and the German Navies. It was found that the stern wedge reduced the ship resistance by up to 6% at its maximum speed, and reduced the running trim by up to 2°. This was found to reduce the fuel consumption of the ship which resulted in a fuel saving of 2%.

Cave et al. (1993) conducted model experiments which showed that the stern flap resulted in a reduction in fuel consumption and power, which in turn increased the top speed of the ship. It was found that when the stern flap was set with a 10 degree downward trailing edge, it decreased the delivered power of an FFG-7 class ship by 8.4%

at 26 knots. The stern flaps were found to improve the powering performance at high speeds, while at low speeds the flaps degraded performance [12].

On the basis of model and full scale experiments, it was found that the installation of a 1% L_{PP} (length between perpendiculars) length stern flap can result in a 11.7% power reduction and a 0.75 knot increase in the top speed [3]. The wedge performance was found to be due to a combination of the afterbody flow modifications and the wave resistance reduction. The trim of the ship, which is hardly modified by the wedge, was only a secondary effect. Day and Cooper (2011) investigated the effect of interceptors on sailing yachts in calm water and small waves. Their results showed a significant reduction in the calm-water resistance over a wide speed range, with an improvement of 10–18% in the speed range between 8 and 20 knots. A reduction in the sinkage and trim was also observed [10]. The best results throughout the speed range was found for an interceptor with h/L = 0.154%, where h is the height of the interceptor and L is the characteristic length of the hull. At lower speeds it was found that a smaller interceptor with h/L = 0.077% performed marginally better.

Karimi et al. (2013) investigated the impact of interceptors on the hydrodynamic quality of planing craft using model towing tank tests. The experimental results showed a remarkable drag reduction of up to 15% for the mono-hull model and up to 12% for the catamaran model.

Mansoori 1 and Fernandes (2016) showed that the interceptor increases the pressure in its installation area, produces a greater lift at the ship stern, and adjusts the running trim of the ship to achieve the purpose of improving the porpoising instability. Mansoori and Fernandes (2015) studied the hydrodynamic effects of interceptors on a 2-D flat plate and found that as the interceptor was inside the boundary layer, the alteration of the flow speed resulted in changes to the boundary layer thickness. This was fond to affect the efficiency of the interceptor. They achieved similar results from experimental testing, where the height of the interceptor is found to be an important factor in the efficiency of the interceptor. They concluded that the height of the interceptor should be selected according to the length of the vessel and the boundary layer thickness at the transom.

Ghassemi et al. (2011) conducted a numerical study to determine the best geometric characteristics of an interceptor. Their test results showed that the interceptor causes an intense pressure rate at its contact point. It also decreases the wet surface of the craft and drag forces coefficient. Lastly, they found that the height of the interceptor has an important effect on its efficiency and should be selected according to the speed of the craft.

Villa and Brizzolara (2009) performed a CFD numerical simulation to compare the hydrodynamic performance of a planing boat after the installation of an interceptor and stern flap. A correspondence between the angle of the flap and the equivalent interceptor height was defined through their results.

Tsai and Hwang (2003) examined the effect of trim mechanisms (including the interceptor, stern flap, and the integrated interceptor and stern flap) on the resistance performance of planing craft. The tests proved that a well-designed trim mechanism can reduce the running trim and decrease the resistance of the planing craft. It was also shown that an interceptor provides better resistance performance when the volume Froude number ranges from 2.0 to 3.0; however, when the volume Froude number is greater than 3.0, a stern flap reduces the drag more effectively.

1.2 Ship hydrodynamic terms

- Waterline

  It is the line where the hull meets the surface of the water.
- Draft (T)

  It is the vertical distance of the bottom of the hull from the waterline.
- Length overall (LOA)

  It is the distance measured between the extreme points in the fore and aft of the ship.
- Waterline length (LWL)

  It is the length of the waterline when the ship floats.
- Fore perpendicular (FP)

It is the perpendicular line passing through the point of intersection of the forward stem and the waterline.

- Aft perpendicular (AP)

  It is the perpendicular line passing through the point of intersection of the aft stem and the waterline.

- Length between perpendiculars (L_{PP})

  It is the length of the ship along the waterline between the fore and aft perpendiculars.

- Beam (B)

  It is the width of the ship along the waterline at its widest point.

- Displacement

  It is the weight of ship based on the water displaced by the ship calculated using Archimedes' principle.

- Trim

  It is the difference between the forward and aft drafts. If the aft draft is greater, the hull is bow down, and if the aft draft is lesser the hull is bow up. The dynamic trim is the trim due to the hull motion.

- Sinkage

  It is the vertical motion that changes the ship draft.

1.3 Hydrodynamics of an Interceptor

An interceptor is a flat plate that is fitted vertically at the transom of a ship and protrudes below the transom. The functioning principle of the interceptor is the generation of an overpressure caused by a sudden variation in the flow due to the interceptor plate. It creates a discontinuity causing a stagnating flow at the protruding edge, resulting in a lift force at the transom and causes the flow to slow down. The stagnation of the flow in the area ahead of the interceptor blade causes the increase in the local pressure. This idea originated from the aeronautical device, the Gurney flap. The

Gurney flap is a device that is geometrically similar to the interceptor, in which a protruding blade increases the pressure on the upstream side of an aerofoil.

The interceptors induce an overpressure on the bottom zone whose longitudinal extension is sufficient to ensure a twofold effect: a significant lift increase; and a trim reduction. Both these effects produce a resistance reduction over a wide range of speeds, as well as a reduction in the trim and sinkage of the hull.

At low speeds, the added resistance generated by the interceptor due to the stagnation pressure forces acting on it, tend to increase the total resistance. At higher speeds however, the estimated effects of the interceptor have to take into account the induced variation of the of the hull motion. The lift forces produced by the interceptor at high speeds corrects the running trim of the hull. This reduced trim results in lower resistance at higher speeds. It is important to observe that the large longitudinal extension of the overpressure zone puts the resultant of the overpressure forces significantly in a forward position compared to other trim correctors (flaps and stern wedges). In other words, with the same moment the interceptors work with shorter levers and greater forces (larger area and higher pressure).

The height of the interceptor can be adjusted by the use of an actuating system that can be used to protrude or retract the interceptor. This enables setting the height of the interceptor such that the protruding height is ideal depending on the speed of the ship.

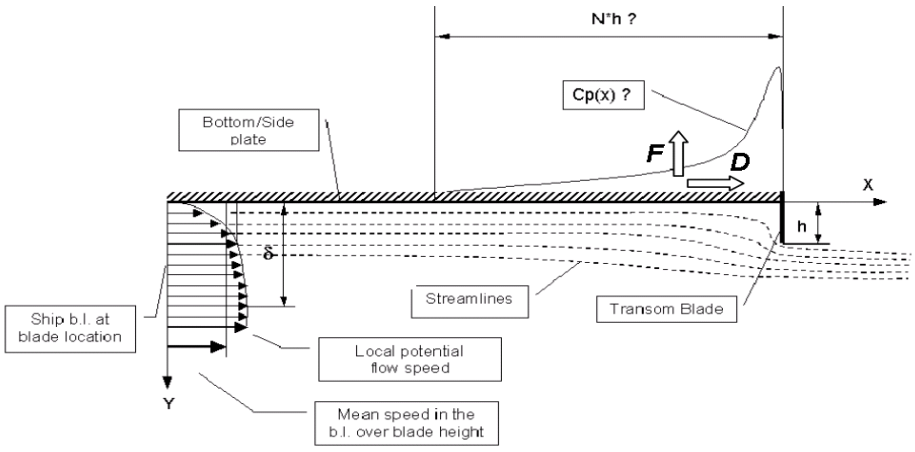

Figure 1-2: Schematization of the hydrodynamics of a 2D interceptor (Courtesy Brizzolara et.al 2003)

Figure 1-2 represents the hydrodynamic schematization of a 2D interceptor protruding downwards off the bottom of a hull [7]. The interceptor blade protrudes off the transom edge with a given height and the blade area (perpendicular to the incoming flow) generates a region of stagnating recirculating flow ahead of it. As a result, the incoming streamlines of the flow bend off hull starting from a relative long distance forward of the interceptor. Hence, the separation point of the streamlines is shifted at the blade tip, while the natural separation of the flow would occur at the transom edge in the case of a bare hull. Aft of the separation point, a free surface flow is established and persists up to the rear boundary of the domain.

The interceptor induces an added resistance (D) and total lift force (F) acting on the hull as depicted in Figure 1-2. The added resistance (D) generated is primarily due to the stagnation pressure force acting on the interceptor, but a correct estimation should also take into account the possible reduction in resistance due to the induced variation of the running trim of the hull and the resultant of pressure forces component in the direction of motion. Since the height of the interceptors is usually lesser than the boundary layer thickness on the hull, the substantial effect of the boundary layer should be taken into account while deciding the geometry of the interceptor.

CHAPTER 2

NUMERICAL INVESTIGATION SETUP

A numerical investigation is conducted on the open source CFD suite OpenFOAM to investigate the calm water resistance of the Oliver Hazard Perry class frigate (FFG-7). A geometric CAD design is prepared on Rhinoceros and modeled as per a $1/80^{th}$ scaled barehull FFG-7 model tested by the United States Naval Academy Hydromechanics Laboratory (NAHL).

The experimental results obtained at NAHL will be used to validate the numerical results obtained for the barehull scaled model in OpenFOAM.

2.1 Reference Case

The Oliver Hazard Perry class frigate (FFG-7), is an existing combatant hull, that has been released to the open literature by the US Navy, hence an ideal candidate to represent a typical hull form of a naval high speed transom stern vessel. As mentioned, several studies about fixed stern energy saving devices have been conducted in the past with model and full scale experimental measurements. A recent experimental investigation on the effect of inversed bow [11] on the FFG-7 hull was conducted at the United States Naval Academy Hydromechanics Laboratory (NAHL) on a $1/80^{th}$ scale model ($\lambda = 80$) without appendages.

The model (Figure -1) was cut from high density closed cell foam and sanded with 400 grit sand paper and coated with DuraTex to achieve a smooth water resistant

finish. Model tests were conducted for calm water conditions as well as with regular and irregular waves. Model was tested at speeds scaled to represent ship speeds from 16 kts to 40 kts, in two unit increments. The results for the calm water model tests are used to validate the numerical results obtained in OpenFOAM. The model was fit with a pitch pivot and attached to a heave post on the towing rig, and was thus free to heave and pitch. Heave and pitch were measured with a pair of potentiometers located at the model's LCB.

The characteristics of the scaled model are given in Table 2-1.

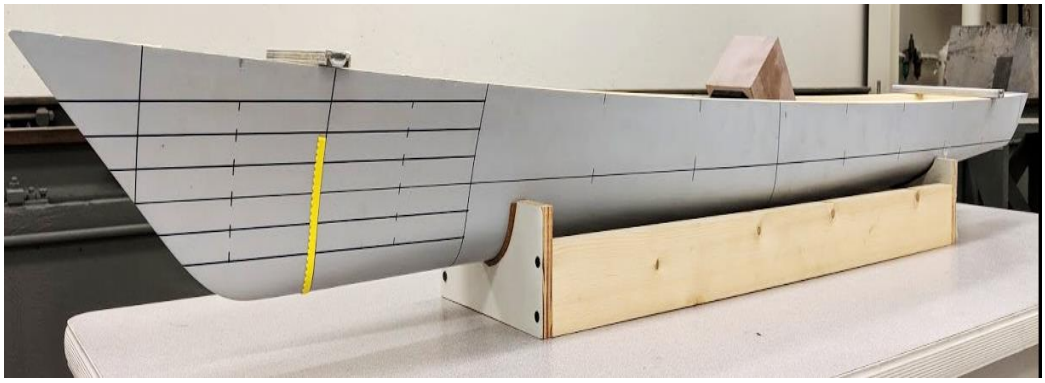

Figure 2-1: FFG-7 model used by NAHL

Table 2-1: Principal characteristics of the FFG7 model (1/80th scale)

Characteristic Lengths	L_{WL} / L_{BP} / L_{OS}	1.569 *m*
Beam molded	BM_L	3.449 *m*
Displacement	Δ	7.996 *kg*
Beam at waterline	B_{WL}	0.172 m
Draft	T	0.0628 *m*
Wetted Surface	S	0.2771 m^2
Waterplane area	A_{WP}	0.2006 m^2
Longitudinal Center of Gravity/Buoyancy	LCG / LCB	0.0107 *m*
Longitudinal Center of Floatation	LCF	0.0843 *m*
Pitch Inertia radius	k_5 (% LBP)	0.394 m (25.2%)

2.2 OpenFOAM

Open Source Field Operation and Manipulation (OpenFOAM), is a free-to-use open source numerical simulation software with extensive CFD and multi-physics capabilities. It is primarily a *C++* library that is used to create executables, known as applications, with the purpose of solving Ordinary and Partial Differential Equations. These applications can be used to solve continuum mechanics problems (solvers), or they can be used for data manipulation (utilities).

OpenFOAM is supplied with pre-processing and post-processing environments with an overall structure as shown in Figure 2-2:

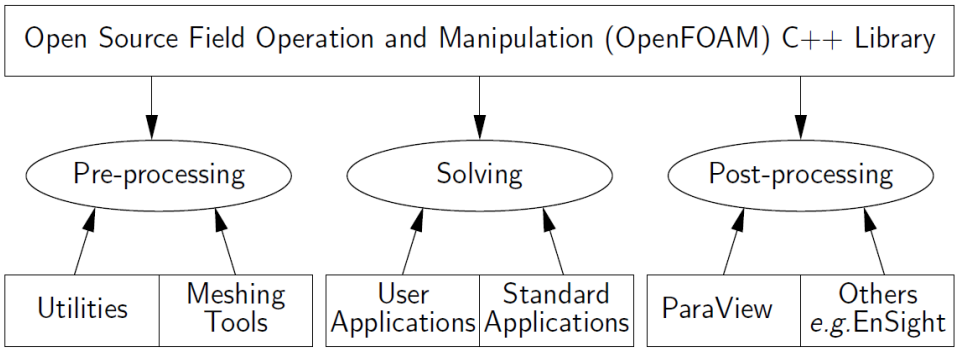

Figure 2-2: OpenFOAM structure (from OpenFOAM User Guide)

2.2.1 OpenFOAM case structure

Each OpenFOAM case has 3 main sub-directories as defined below:

- **system** – This directory contains dictionaries for setting the parameters associated with the solution procedure (time step size, discretization schemes, solution schemes, etc.)
- **constant** – This directory contains the case mesh files in a sub-directory (polyMesh), and files specifying the physical properties for the application concerned (transport properties, gravity, turbulence properties, etc.)

- **time directories** – These contain the solution files for particular fields at each time step. The 0/ time directory contains the initial boundary conditions for the case.

  The file structure and the above sub-directories for each OpenFOAM case is depicted in Figure 2-3.

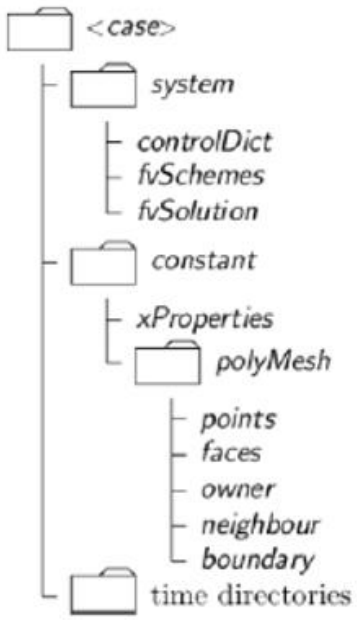

Figure 2-3: OpenFOAM case structure (from OpenFOAM User Guide)

2.2.2 Solver

The OpenFOAM solver most suited for this study was identified to be interDyMFoam.

interDyMFoam is a solver for 2 incompressible, isothermal immiscible fluids using a VOF (volume of fluid) phase-fraction based interface capturing approach. It also permits optional mesh motion and mesh topology changes including adaptive re-meshing.

2.2.3 Co-ordinate system

The co-ordinate system using during the numerical investigation is shown in Figure 2-4. The x-axis is directed towards the fore of the hull, the y-axis is directed towards the port of the hull, and the z-axis is vertically upwards.

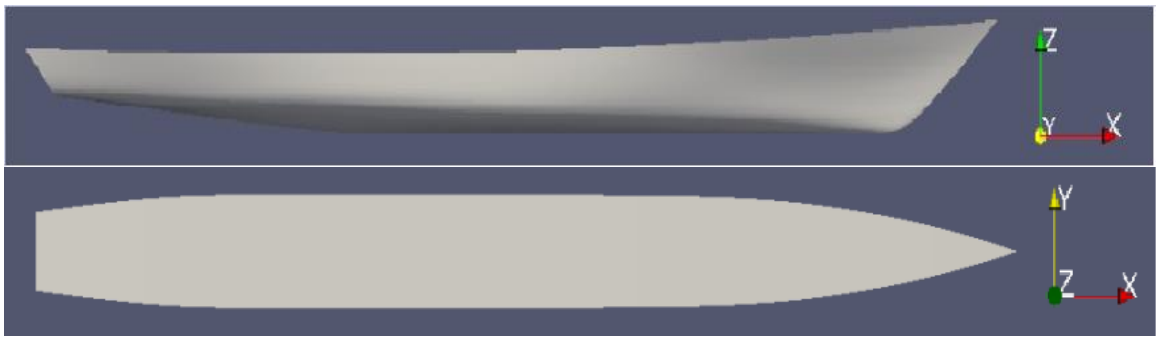

Figure 2-4: Co-ordinate system

2.2.4 Governing Equations

The ship flow in this solver is governed by the incompressible, three dimensional time dependent Reynolds Averaged Navier-Stokes Equations (RANSE) and the conservations laws of mass, momentum and energy. Since the flow around the hull is incompressible and a constant temperature is assumed, the energy equation can be ignored.

The differential form of the continuity equation and the momentum equation are given as:

$$\frac{\partial \rho}{\partial t} + \nabla . (\rho v) = 0 \tag{2.1}$$

$$\frac{\partial (\rho v)}{\partial t} + \nabla . (\rho v v) = \nabla . T + \rho g + f \tag{2.2}$$

Where, ρ is the density of the fluid, v is the velocity of the fluid, T is the Cauchy stress tensor, g is the acceleration due to gravity and f is the force per unit volume. The stress tensor, T, is defined as:

$$T = -PI + \tau \tag{2.3}$$

Where, P is the pressure, I is the identity tensor and τ is the stress tensor. The momentum equation can then be written as:

$$\frac{\partial(\rho v)}{\partial t} + \nabla.(\rho v v) = -\nabla P + \nabla.\tau + \rho g + f \tag{2.4}$$

Since the flow is considered to be an incompressible flow, the equation becomes:

$$\nabla.v = 0 \tag{2.5}$$

$$\rho\{\frac{\partial v}{\partial t} + (v.\nabla)v\} = -\nabla P + \nabla.\tau + \rho g + f \tag{2.6}$$

To solve the multiphase flow, the free surface fluid interface is modeled using the Volume of Fluid (VOF) method. The VOF method uses a quantity called phase volume fraction (α) which defines the percentage of the specific fluid in each cell of the mesh, thereby indicating which fluid properties have to be considered by the solver.

The two fluid phases in this study are water and air, where water is defined by α=1 and air is defined by α = 0.

$$\alpha = \begin{cases} 1 & water \\ 0 & air \end{cases} \tag{2.7}$$

For the case where the interface passes through the cells, α has a value of $0 < \alpha < 1$, such that:

$$\alpha = \frac{V_{water}}{V} \tag{2.8}$$

Where, V_{water} is the volume of water in the cell and V is the total volume of the cell. The governing equation for the volume fraction variable α is as below:

$$\frac{\partial \alpha}{\partial t} + \nabla.(u\alpha) + \nabla.(\alpha(1-\alpha)u_r) = 0 \tag{2.9}$$

Where, u_r is the interface compression velocity. The interface compression term $[\nabla.(\alpha(1-\alpha)u_r)]$ maintains a sharp interface between the two defined phases, whereas the first two terms $[\frac{\partial \alpha}{\partial t} + \nabla.(u\alpha)]$ give the advection equation.

The fluid properties of each phase can be defined throughout the case domain as follows:

$$\mu(x_{cell}, t) = \mu_{water}\alpha(x_{cell}, t) + \mu_{air}(1 - \alpha(x_{cell}, t)) \tag{2.10}$$

Where, μ is a predefined fluid property for the given phases. Therefore the density (ρ) and viscosity (v) for the air and water in the domain can be calculated as:

$$\rho = \alpha\rho_{water} + (1-\alpha)\rho_{air} \tag{2.11}$$

$$v = \alpha v_{water} + (1-\alpha)v_{air} \tag{2.12}$$

2.3 Meshing

The geometric CAD design is prepared on Rhinoceros and modeled as per the NAHL 1/80th scaled barehull FFG-7 model. A mesh is prepared using the in-built OpenFOAM mesh generation tools, blockMesh and snappyHexMesh.

The blockMesh utility is used to create the computational domain, which for this study is a rectangular box. The snappyHexMesh conducts a Boolean operation as well as a series of mesh refinements in order to subtract the hull from the domain.

Since the geometry of the ship is symmetrical along the vertical longitudinal plane, the computational time can be reduced by modeling the domain for only half of the hull. Using a symmetrical condition we would not lose any information while gaining significant advantages in computational cost and computational time.

2.3.1 Computational domain

The computational domain is the boundary within which the analysis of the case and its parameters is carried out. It is a rectangular box from which the hull geometry is subtracted. The size of the domain is determined based on the length of the hull model. The dimensions of the computational domain for this study are taken as 5 L_{PP}× 1.6 L_{PP}× 2.5 L_{PP} in the x, y and z directions respectively.

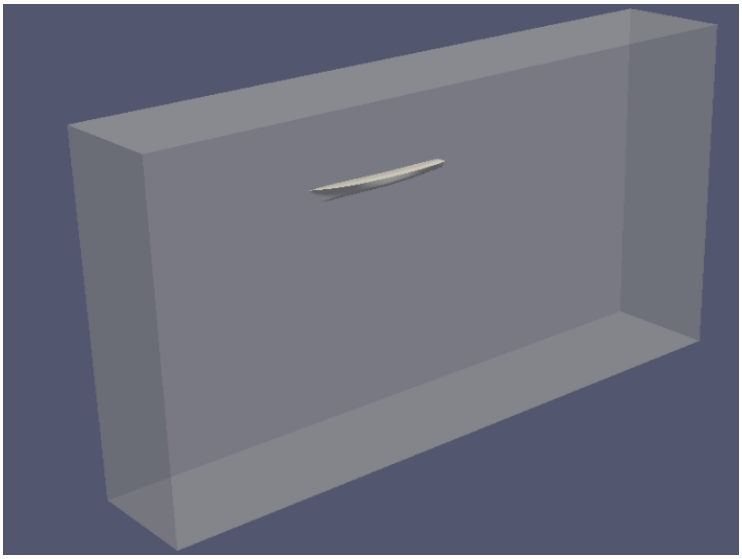

Figure 2-5: Computational Domain

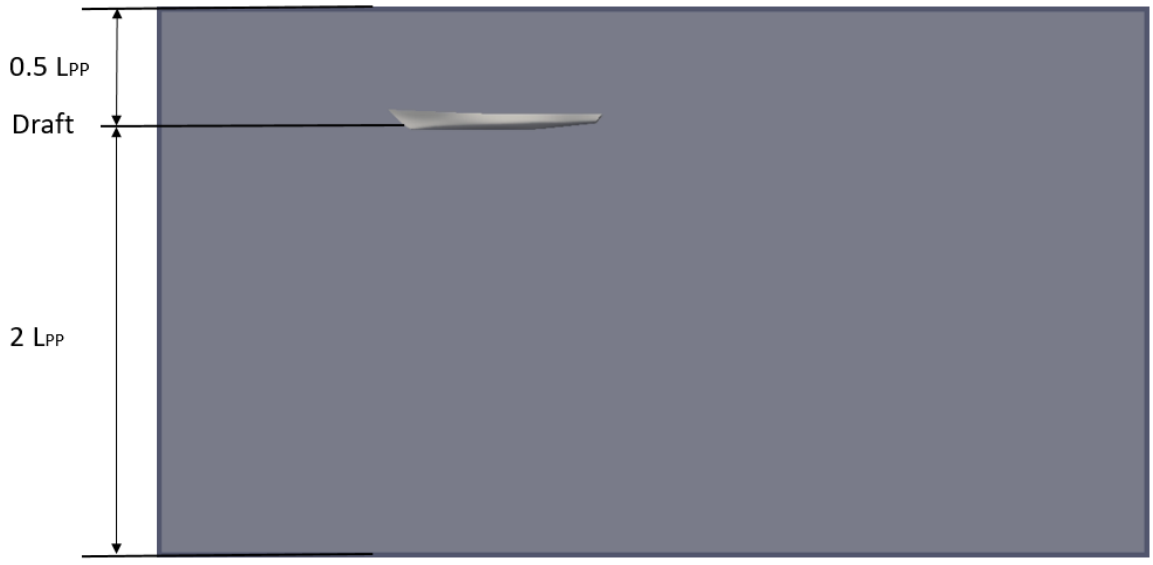

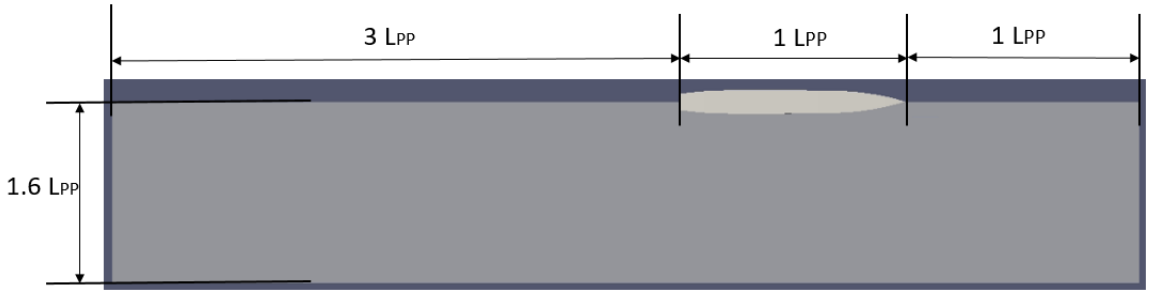

Figure 2-6: Computational Domain Dimensions

2.3.2 blockMesh

The blockMesh utility is used to create the rectangular computational domain by defining the co-ordinates of the vertices in the blockMeshDict file (Figure 2-7). The rectangular domain is then decomposed into a set of 1 or more three dimensional hexahedral blocks.

The decomposition into the hexahedral blocks is done by defining a large number of vertices such that instead of creating one large block, we can create multiple smaller blocks. This enables creating a mesh where we can focus maximum cells in regions important to the computation, in this case the free surface, while at the same time minimizing the total cells in the domain.

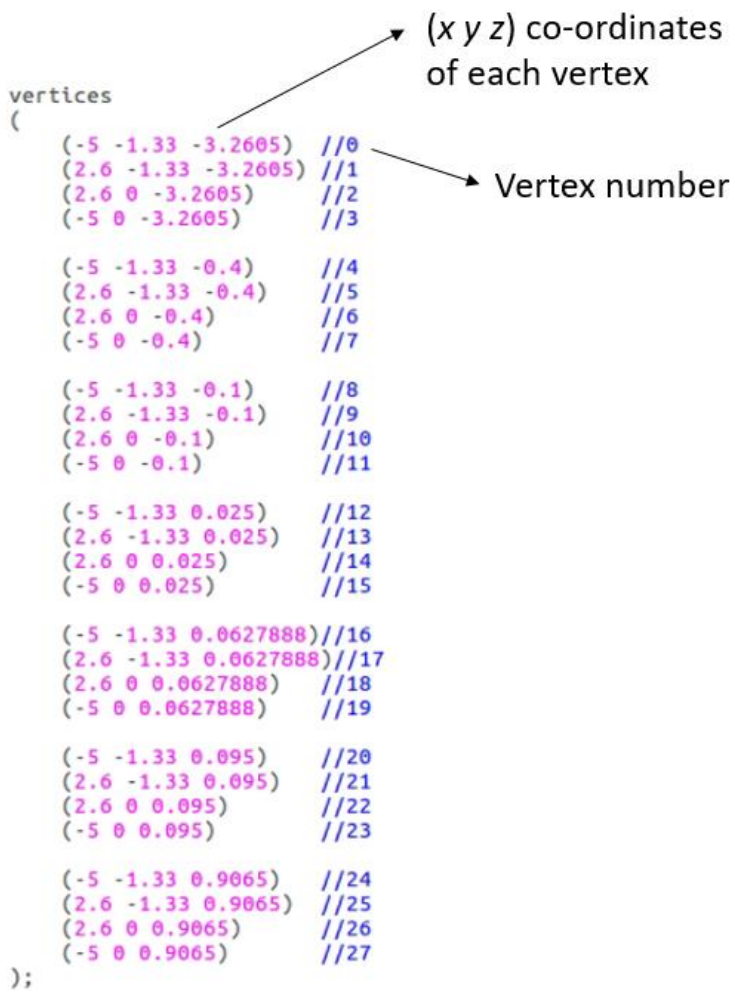

Figure 2-7: Defining the vertices in *blockMeshDict*

The decomposed hexahedral blocks are as shown in *Figure 2-8*, where the red numbers depict the vertices with the vertex numbers as defined in the blockMeshDict. The black lines depict the segregated blocks that are created using the vertices.

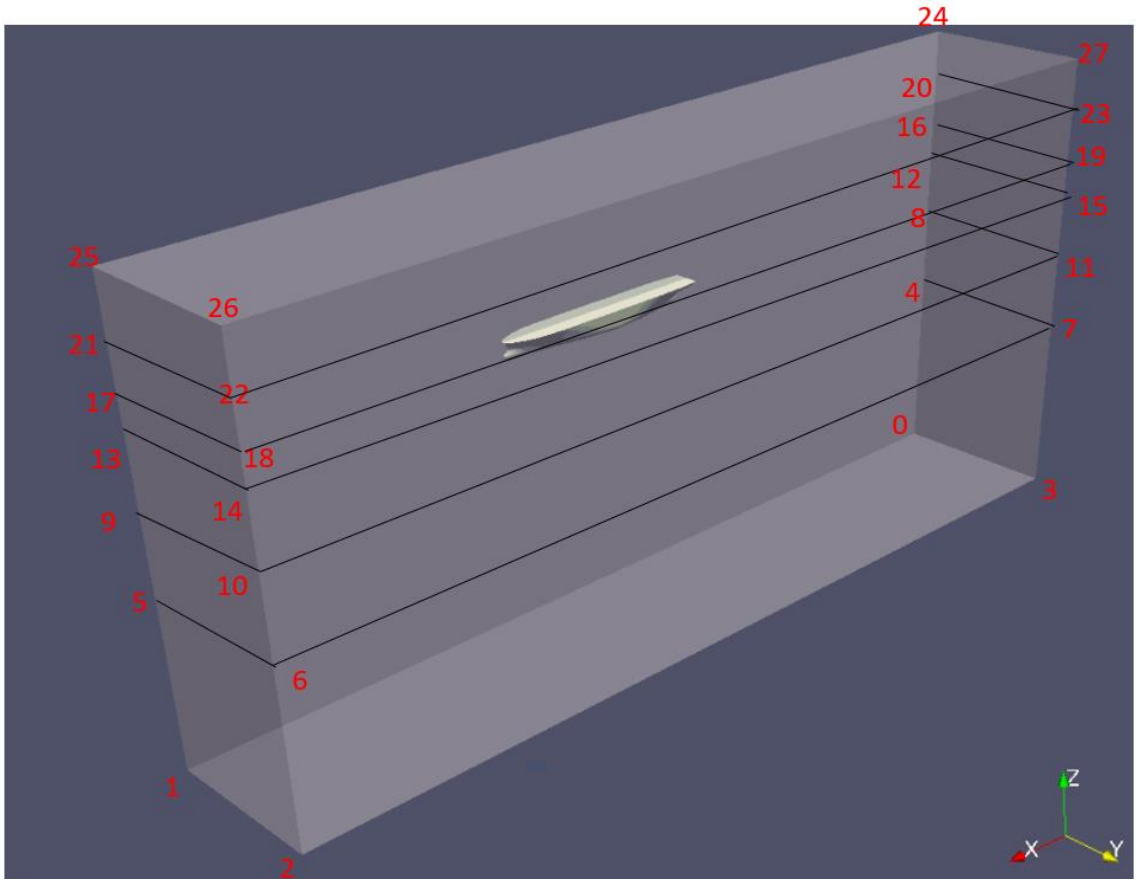

Figure 2-8: Decomposed hexahedral blocks in the domain

The mesh generated by blockMesh is as in Figure 2-9. The separate hexahedral blocks enable having a higher concentration of cells near the free surface as opposed to the outer ends of the domain away from the hull. The blockMesh also defines and generates the patches on the domain where the boundary conditions are applied. The patches defined in the blockMesh are the inlet (front), outlet (back), symmetry plane (midplane), side, atmosphere (top) and bottom, as depicted in Figure 2-10.

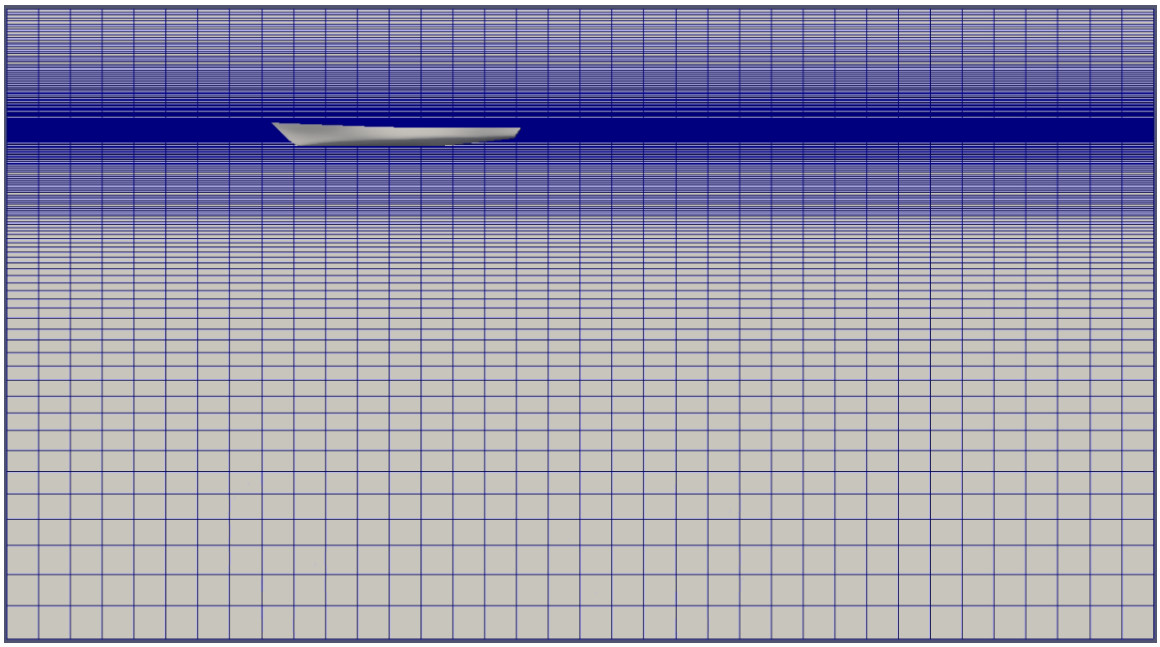

Figure 2-9: blockMesh

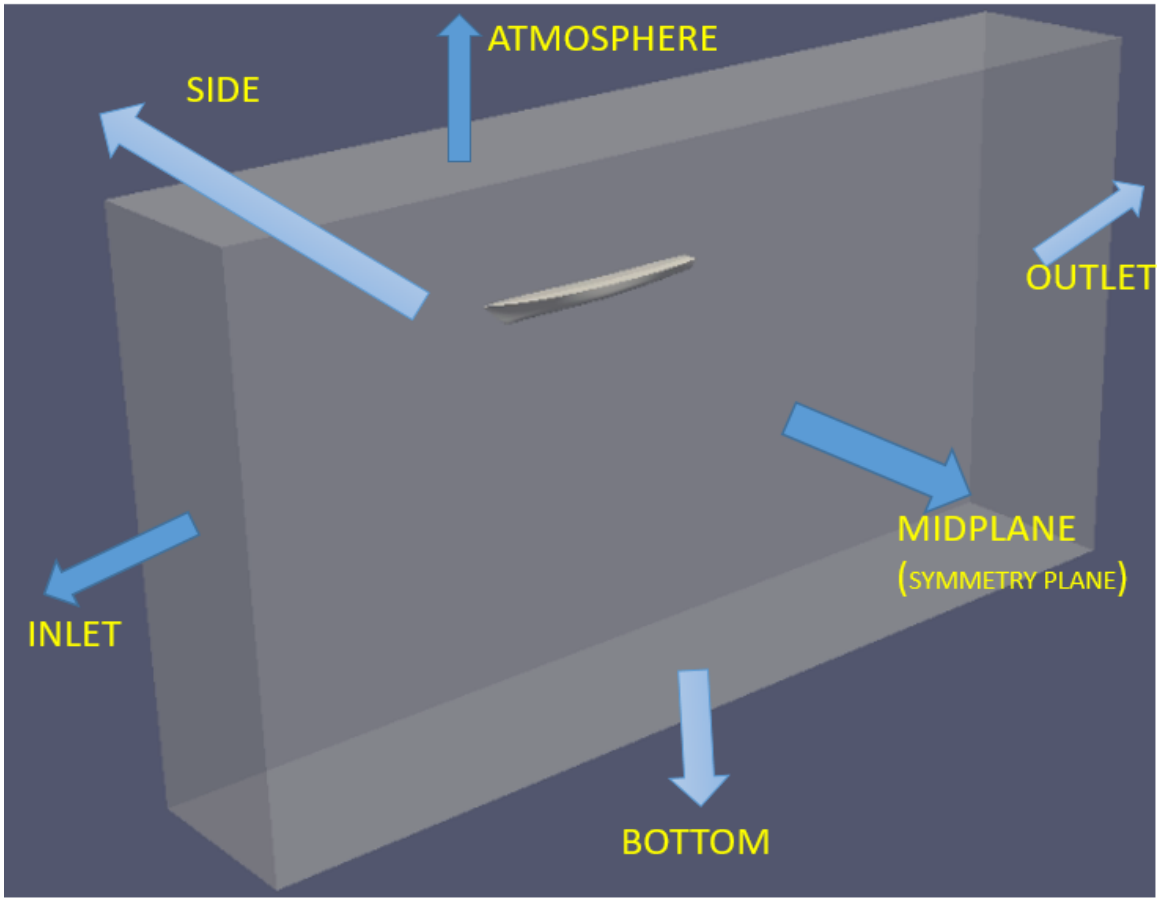

Figure 2-10: Domain patches

Further refinements are made to the blockMesh with the use of the OpenFOAM utilities, topoSet and refineMesh. The topoSet utility defines a block within the domain and a refinement factor and direction as in the refineMesh. All the cells within the defined block get refined. To attain well refined and fine cells around the hull, multiple topoSet blocks are defined as can be seen in Figure 2-11.

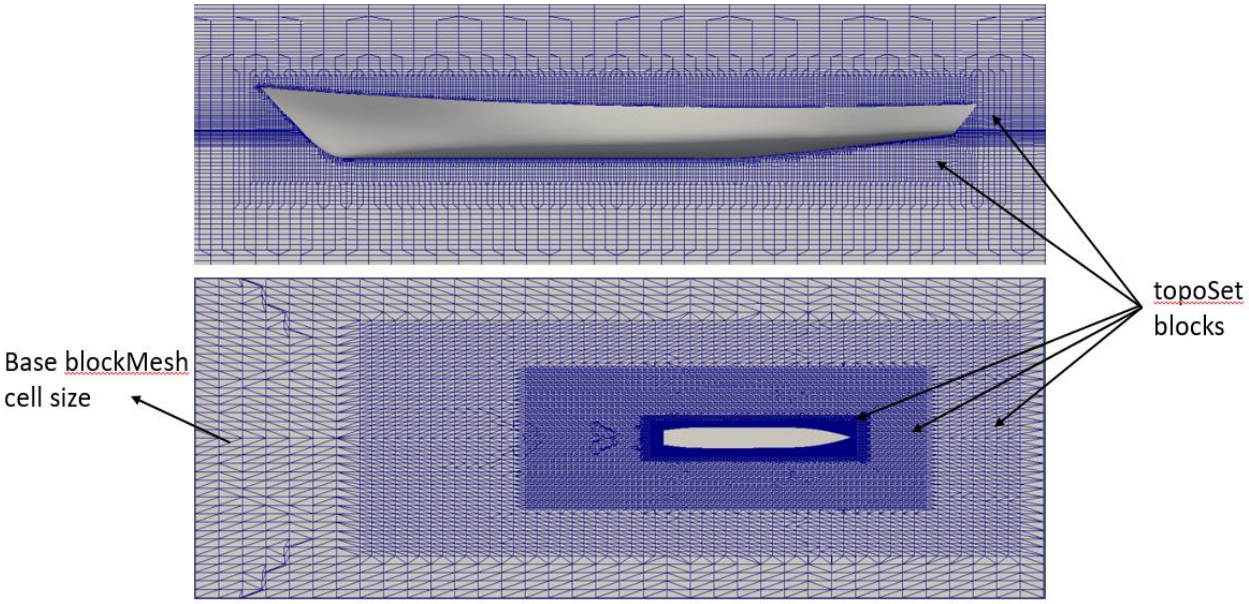

Figure 2-11: Mesh refinement

2.3.3 snappyHexMesh

snappyHexMesh is an OpenFOAM utility that generates three dimensional meshes containing hexahedral and split-hexahedral cells from triangulated surface geometries. The surface geometry is created in the Rhinoceros and used by snappyHexMesh in a stereolithography format (.stl). snappyHexMesh removes the cells within the hull geometry from the hexahedral mesh generated by blockMesh. This is done by iteratively refining the blockMesh and morphing the resulting split-hex mesh to conform to the surface of the hull geometry.

The final snappyHexMesh is obtained by following a series as steps as given below:

1. Creation of a castellated mesh

   Cells splitting of the cells intercepted by the hull surface is performed as per the parameters defined in the castellatedMeshControls in the snappyHexMeshDict. The splitting is done based on the identified edge features of the hull geometry, where a series of refinements split the cells based on the defined parameters.

   After the cell splitting iterations are completed, the cell removal process begins. Cells in the domain are retained if approximately less than 50% of the cell volume is within the hull geometry. Any cell which has more than 50% of its volume within the hull is removed from the mesh.

2. Snapping to surface

   During this step, the cell vertex points near the hull surface are projected onto the surface in order to remove the jagged edges formed during the mesh castellation. The internal mesh is then relaxed and the mesh quality is checked to ensure that it conforms to the required user defined parameters. This process is repeated till the mesh quality parameters are satisfied.

3. Addition of layers

   This step introduces layers of hexahedral cells aligned to the boundary surface of the hull. The internal mesh is then relaxed and the mesh quality is checked. The thickness of the layer is reduced until a satisfactory mesh is obtained. After the validation of the parameters is achieved, the layers are added to the mesh. This step is very important since the quality and thickness of the layers affect the $y+$, which is an important factor in this numerical investigation.

2.4 Boundary conditions

The initial boundary conditions for the domain are defined for all the patches set up in the blockMeshDict. These conditions are set up for each variable (velocity, pressure, kinematic viscosity, turbulence model parameters, etc.), in the *0/* time directory.

In the blockMeshDict, the midplane, bottom and side patches are defined as symmetryPlane type patches. Therefore these 3 patches have zero normal velocity and zero normal gradients for the other boundary condition variables.

2.4.1 Velocity

The initial boundary conditions for each individual patch is defined in m/s. Initially a mean velocity is imposed over the complete domain, after which the individual patch conditions are imposed. The hull model only pitches and heaves at its location while the velocity of the hull is imposed on the domain. Therefore the fluids in the domain move at the required speed in a direction opposite to the hull motion. Therefore the initial velocity is defined as a negative value in the x-direction.

The initial conditions for the velocity are given in Table 2-2. The values for a Froude number of 0.25 is given, which equates to a velocity of 0.9619 m/s.

Table 2-2: Initial boundary conditions for velocity

Boundary	Type	Value (m/s)	Definition
Inlet	fixedValue	uniform (-0.9619 0 0)	It assigns a uniform value of the velocity all over the patch.
Outlet	outletPhaseMeanVelocity	uniform (-0.9619 0 0)	A uniform velocity is assigned over the patch and the fluid phase fraction is adjusted to maintain the mass conservation.
Atmosphere	pressureInletOutletVelocity	uniform (0 0 0)	It is a velocity condition for boundaries where the pressure is specified. It gives a zero gradient condition for the outflow and a patch normal of the cell value for inflow.
Hull	movingWallVelocity	uniform (0 0 0)	It applies a condition in the presence of a moving wall, which in this case is 0.

2.4.2 Pressure

The solver interDyMFoam does not solve for the total pressure in the domain. Instead, it calculates a value which is defined as *p_rgh* which is the total pressure minus the hydrostatic pressure. The solver then calculates the total pressure in post-process by adding the hydrostatic value to the calculated *p_rgh* values. The initial boundary conditions for each individual patch is defined in kg/(m.s^2) or Pascal.

An initial *p_rgh* value of 0 Pascal is imposed on the whole domain after which the individual patch boundary conditions are applied.

Table 2-3: Initial boundary conditions for *p_rgh*

Boundary	Type	Value (Pa)	Definition
Inlet	fixedFluxPressure	uniform 0	This condition adjusts the pressure gradient on the patch to maintain the flux specified in the velocity condition.
Outlet	zeroGradient	-	It extrapolates the value from the domain. Therefore no input value is required.
Atmosphere	totalPressure	uniform 0	It imposes the condition on the total pressure where the inflow velocity is subtracted from the input pressure of 0 Pa to find the pressure.
Hull	fixedFluxPressure	uniform 0	This condition adjusts the pressure gradient on the patch to maintain the flux specified in the velocity condition.

2.4.3 Fluid phase fraction

As explained in Section 2.2.3, the fluid phase fraction (α) defines the percentage of the specific fluid in each cell of the mesh, thereby indicating which fluid properties have to be considered by the solver.

An initial α value of 0 is imposed on the whole domain. Since α = 0 is the value for air, the whole domain is initialised with air. The required water, as per the draft for the hull, is then added to the domain as defined in the setFieldsDict.

Table 2-4: Initial boundary conditions for phase fraction (α)

Boundary	Type	Value	Definition
Inlet	fixedValue	uniform 0	It assigns a uniform value all over the patch.
Outlet	variableHeightFlowRate	lower bound 0 upper bound 1 value uniform 0	It takes the value of the variable from the domain, and if it is within the specified bounds, it behaves as a zeroGradient condition. The lower and upper bound for the variable is defined as 0 and 1 respectively.
Atmosphere	inletOutlet	uniform 0	If there is outflow at the patch, it uses a fixed value condition. Whereas if there is inflow, it applies the zeroGradient condition.
Hull	zeroGradient	-	It extrapolates the value from the domain. Therefore no input value is required.

2.5 Solver setup

2.5.1 CFL number

The Courant-Friedrich-Lewy (CFL) condition is a numerical constraint that determines the permissible time step for the given mesh. The CFL number limits the distance that the fluid can travel in one time-step. This is done to ensure that the results do not diverge resulting in errors during the case run time. The CFL number is given as:

$$Co = \frac{u\Delta t}{\Delta x} \leq Co_{max} \tag{2.13}$$

Where, u is the velocity, Δt is the time-step and Δx is the size of the smallest cell in the mesh. The Co_{max} value is the maximum permitted value for the CFL number. If the CFL value exceeds the Co_{max} value, it might affect the stability of the case. The time-stepping for this solver is done using an adjustable time step method. Therefore the time step adapts according to Equation 2.13 in a way as to ensure that the Co_{max} value is not exceeded.

The Co_{max} value depends on the solver used, and the generally accepted value for Co_{max} is 1. The solver used for this study, interDyMFoam, is an implicit solver which simulates the evolution of the free surface in transient mode, and thus uses a CFL number at the interface which is based on the surface normal velocity. Therefore the maximum CFL number imposed for the domain and the free surface in this case are 5 and 0.5 respectively. This reduces the computational time for the case while ensuring the stability of the solution.

2.5.2 Turbulence model

Turbulent flow is characterized by highly irregular and unsteady behavior in both the spatial and temporal dimensions, and therefore simulating this turbulence with an appropriate turbulence model is important in order to achieve accurate results.

This study requires a turbulence model that can simulate a strong adverse pressure gradient flow field and which can also account for the impact of the shear force exerted by the wall of the hull. The *k-ε* turbulence model predicts more accurately away from the hull due to its insensitivity to the free stream. The *k-ω* is unable to accurately simulate a strong adverse pressure gradient. Therefore the turbulence model most suited for this CFD investigation was found to be the *k-ω Shear Stress Transport (SST)* model. The *k-ω SST* model limits the shear stress in adverse pressure gradient, which results in improved prediction of adverse pressure gradient flows [14].

2.5.3 *k-ω* Shear Stress Transport (SST) model

The *k-ω SST* model is a two-equation eddy viscosity model for the turbulence kinetic energy, *k*, and turbulence specific dissipation rate, *ω*, which utilizes both the *k-ε* and *k-ω* models. It utilizes the free stream independence of the *k-ε* model in the far field with the accuracy of the *k-ω* model near the wall. This is done by a blending function which uses a value of 1 to activate the *k-ω* model in the near-wall region, while a value of 0 activates the *k-ε* model. *k-ω SST* model also has good prediction for flows with

separation. Since we observe flow separation at the stern at high speeds, it is an additional improvement.

The k and ω for this model are initialized with a constant value at the inlet patch, as given by:

$$k = \frac{3}{2}(I\,|u_{ref}|)^2 \tag{2.14}$$

$$\omega = \frac{k^{0.5}}{C_\mu L} \tag{2.15}$$

The *turbulence kinetic energy equation*, k, is given by:

$$\frac{D}{Dt}(\rho k) = \nabla.(\rho D_k \nabla k) + \rho G - \frac{2}{3}\rho k(\nabla.u) - \rho\beta^*\omega k + S_k \tag{2.16}$$

The *turbulence specific dissipation rate equation*, ω, is given by:

$$\frac{D}{Dt}(\rho\omega) = \nabla.(\rho D_\omega \nabla\omega) + \frac{\rho\gamma G}{v} - \frac{2}{3}\rho\gamma\omega(\nabla.u) + -\rho\beta\omega^2 - \rho(F_1 - 1)CD_{k\omega} + S_\omega \tag{2.17}$$

The *turbulence viscosity*, v_t is given by:

$$v_t = a_1 \frac{k}{\max(a_1\omega,\ b_1F_{23}S)} \tag{2.18}$$

The boundary layer is identified by using the non-dimensional wall distance (y^+) term. The y^+ is calculated from:

$$y^+ = \frac{u_t y}{\nu} \tag{2.19}$$

The boundary layer is divided into three regions that can be categorized by the y^+ value as below:

1. *Viscous sub layer* in a region of $0 < y^+ < 5$. In this sub layer the fluid viscosity has the highest effect.
2. *Buffer sub layer* in a region of $5 < y^+ < 30$. In this sub layer the viscous and inertial effects are equal.

3. *Inertial sub layer* in a region of $30 < y^+ < 500$. In this sub layer the effect of the inertia is the highest.

Wall functions corresponding to High Re number flows are used. Wall function for k is set to *kqRWallFunction* on the hull patch, and acts as a Neumann boundary condition. It is initialized with a value of 0.00015 m^2/s^2. For ω, an *omegaWallFunction* is used, which is initialized with a value of 2 s^{-1}. The *nutkRoughWallFunction* is used for ν_t, and is initialized with a value of 5e-07 m^2/s.

2.5.4 Mesh motion

In interDyMFoam, the six degree-of-freedom mesh motion is simulated by solving the equation of motion with the assumption of linearized motions:

$$M(\ddot{\eta}_3 - x_G\ddot{\eta}_5) = F_3(t) = F_3(\eta_3, \eta_5, \dot{\eta}_3, \dot{\eta}_5, \ddot{\eta}_3, \ddot{\eta}_5) \quad (2.20)$$

$$I_{55}\ddot{\eta}_5 - Mx_G\ddot{\eta}_3 = F_5(t) = F_5(\eta_3, \eta_5, \dot{\eta}_3, \dot{\eta}_5, \ddot{\eta}_3, \ddot{\eta}_5) \quad (2.21)$$

Where, i = 1, 2 and 3, are used to represent the translational motion of the body in the x, y and z directions respectively. Similarly, i = 4, 5 and 6, are used to represent the rotational motion of the body in the x, y and z directions.

Where,

$F_j(t)$, where j =1, 2, 3 represent the total forces in the x, y and z directions.

$F_j(t)$, where j =4, 5, 6 represent the total moments about the x, y and z directions.

M = Total mass of the hull.

I_{55} = Moment of inertia about the about the y axis.

x_G = x coordinate of the center of gravity of the hull.

η_3 = Heave

η_5 = Pitch

$\dot{\eta}_j(t)$ = Velocity in the j^{th} degree of freedom

$\ddot{\eta}_j(t)$ = Acceleration in the j^{th} degree of freedom

The motion of the body is restricted to only pitch and heave. A set of constraints are applied to the body which restrain translation to the z-direction (sinkage), and rotational motion about the y-axis (trim).

2.6 Mesh sensitivity analysis

In order to verify the meshing procedure and the accuracy of the numerical results, a mesh sensitivity analysis is conducted on three different meshes at a speed of 0.392 Fr. For the study, a constant refinement ratio (r_k) is used for the mesh refinement, and is defined as:

$$r_k = \Delta x_{k_m} / \Delta x_{k_{m-1}} \tag{2.22}$$

As per ITTC 2008 guidelines, the recommended r_k value of $\sqrt{2}$ is chosen. In OpenFOAM the mesh is created by defining the number of cell divisions in each direction (x, y and z axis) of the domain. Therefore the r_k value of $\sqrt{2}$ was used to modify the number of cells in the three different meshes in order to obtain a coarse, medium and fine mesh. Next, a convergence ratio (R_k) is defined to provide information about the convergence/divergence of a solution. The solution changes($e_{ijk} = S_{ki} - S_{kj}$) for the input parameter *k* between the three solutions including fine (S_{k1}) to medium (S_{k2}) and coarse (S_{k3}) to obtain the R_k value is

$$R_k = \varepsilon_{21_k} / \varepsilon_{32_k} \tag{2.23}$$

The results from the three meshes tested in OpenFOAM, resulted in a R_k value of $0 < R_k < 1$. This implies that there is a monotonic convergence observed in the results between the three meshes. As per ITTC 2008, in the case of a monotonic convergence, the generalized Richardson extrapolation method is used to assess the uncertainty (U_k) or the error estimate(δ_k).

The parameters and results of the three different meshes are provided in Table 2-5 and Table 2-6. The results from the mesh sensitivity analysis suggest that results obtained from the meshing method used is accurate. The computation time of the fine mesh is expectedly higher than that of the coarse and medium meshes, but in order to ensure the highest accuracy in the calculation of the numerical results, the fine mesh is used for all numerical calculations carried out in this study.

Table 2-5: Parameters and results of the 3 meshes

Grid no.	Total cells	r_k	RTm (N)	RFm (N)	Trim (Deg)
1 (Fine)	1,556,679	1.41	2.28	1.42	0.263
2 (Medium)	555,472	1.39	2.21	1.35	0.265
3 (Coarse)	206,865		2.09	1.24	0.268

Table 2-6: Uncertainty and Error estimates for the results

Result	R_k	% Uncertainty (U_k)	% Error estimate (δ_k)
RTm (N)	0.584	2.88	7.15
RFm (N)	0.616	4.2	6.94
Trim (Deg)	0.722	0.29	0.18

CHAPTER 3

NUMERICAL RESULTS AND VALIDATION

Numerical CFD tests for the FFG-7 bare hull are run on OpenFOAM for a speed range corresponding to Froude number 0.205 to 0.44.

The numerical results from OpenFOAM will then be validated using the experimental results obtained at NAHL for the barehull model.

3.1 Resistance

Resistance is the force that is responsible for the motion of the ship at the desired speed. The hull model used for this study does not have any appendages, in which the resistance is referred to as the barehull resistance.

The main factors attributing to the resistance are the distribution of the pressure and the shear forces acting on the hull. The total resistance is divided into two components:

- Shear / Friction resistance

  This is the resistance experienced due to the friction between the hull and water. This is caused due to the viscosity of the fluid medium and is the sum of all the tangential shear stresses on the hull.

- Pressure / Residuary resistance

  This is the sum of the all the pressure forces acting on the hull.

3.1.1 Resistance Coefficients

The resistance data measured from the model tests is used to calculate the total resistance co-efficient, friction resistance co-efficient and the residuary resistance co-efficient for the model.

The *total resistance co-efficient* (C_{T_m}) of the model is calculated as:

$$C_{T_m} = \frac{R_{T_m}}{0.5 * S * \rho * V^2} \tag{3.1}$$

where, R_{T_m} is the total model resistance, S is the nominal wetted surface area, ρ is the density of the water in the tank, and V is the velocity of the model.

The *friction resistance co-efficient* (C_{F_m}) for the model is calculated as per the ITTC-57 formula:

$$C_{F_m} = \frac{0.075}{(\log Re_m - 2)^2} \tag{3.2}$$

where, Re_m is the Reynolds number at the particular speed.

The *residuary resistance co-efficient* (C_{R_m}) of the model is calculated as:

$$C_{R_m} = C_{T_m} - (1 + k)C_{F_m} \tag{3.3}$$

where, (1+*k*) is the form factor.

3.1.2 Corrected Resistance Coefficients

A few corrections are made to the calculation of the resistance coefficients. For the residuary resistance co-efficient, a correction is made to the calculation in order to get a better comparison between the experimental and numerical results. In order to get the

residuary resistance, the friction resistance on the model is calculated and then subtracted from the total model resistance. To get a more accurate approximation of the model friction resistance, there is a correction made to the wetted surface area of the model. The wetted transom area, unlike the rest of the wetted hull area, does not add any component to the model friction resistance. Therefore the wetted transom area is subtracted from the total wetted surface area of the hull so as to obtain only the area that contributes to the friction resistance acting on the model. This new wetted surface area (S^N) is calculated from the numerical data for each tested speed using the visualization application ParaView.

The *corrected friction resistance* (R_{F_m}) of the model is calculated as:

$$R_{F_m} = {C_{F_m}}^{ITTC} * 0.5 * S^N * \rho * V^2 \tag{3.4}$$

The *corrected residuary resistance* (R_{R_m}) of the model is:

$$R_{R_m} = R_{T_m} - R_{F_m} \tag{3.5}$$

The *corrected residuary resistance co-efficient* (C_{R_m}) of the model is then calculated as:

$$C_{R_m} = \frac{R_{R_m}}{0.5 * S * \rho * V^2} \tag{3.6}$$

For the numerical data a similar procedure is followed and the resistance coefficient's are calculated and validated with the experimental data. The formula for the shear resistance co-efficient (friction co-efficient) calculated from the numerical data varies from the ITTC-57 formula used for the experimental data.

The *shear resistance co-efficient* (C_{R_s}) is calculated as:

$$C_{R_s} = \frac{R_F}{0.5 * S^N * \rho * V^2} \tag{3.7}$$

Using the resistance data obtained from OpenFOAM, we calculate the resistance coefficients as well as the corrected resistance coefficients. The results are plotted in Figure 3-1 to Figure 3-3.

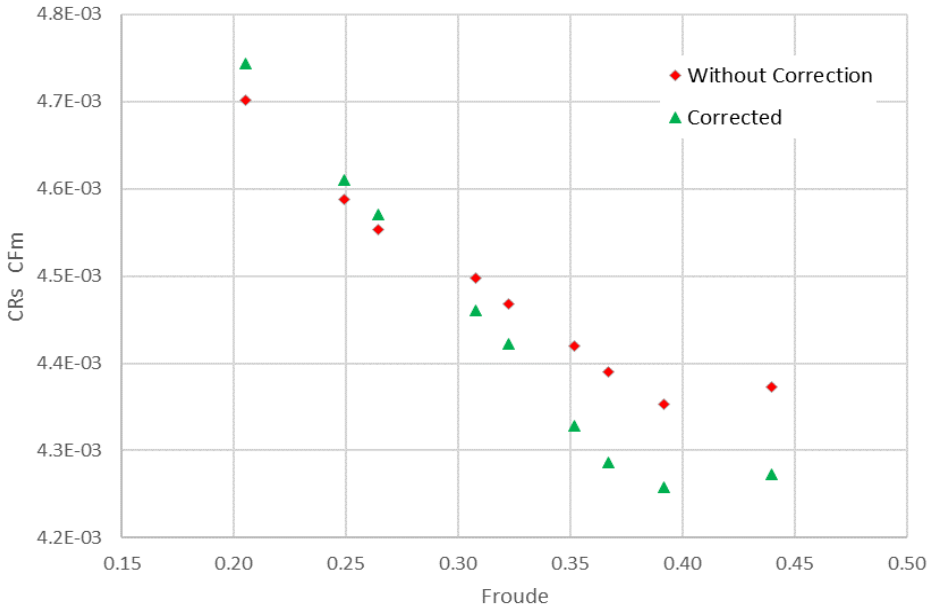

Figure 3-1: Comparison of the shear resistance coefficient

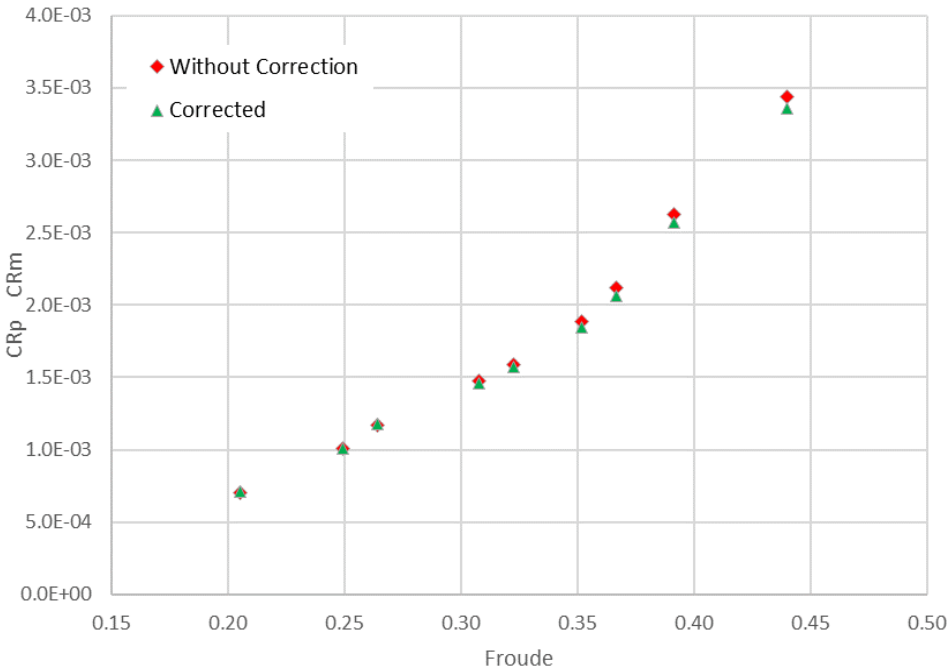

Figure 3-2: Comparison of the pressure resistance coefficient

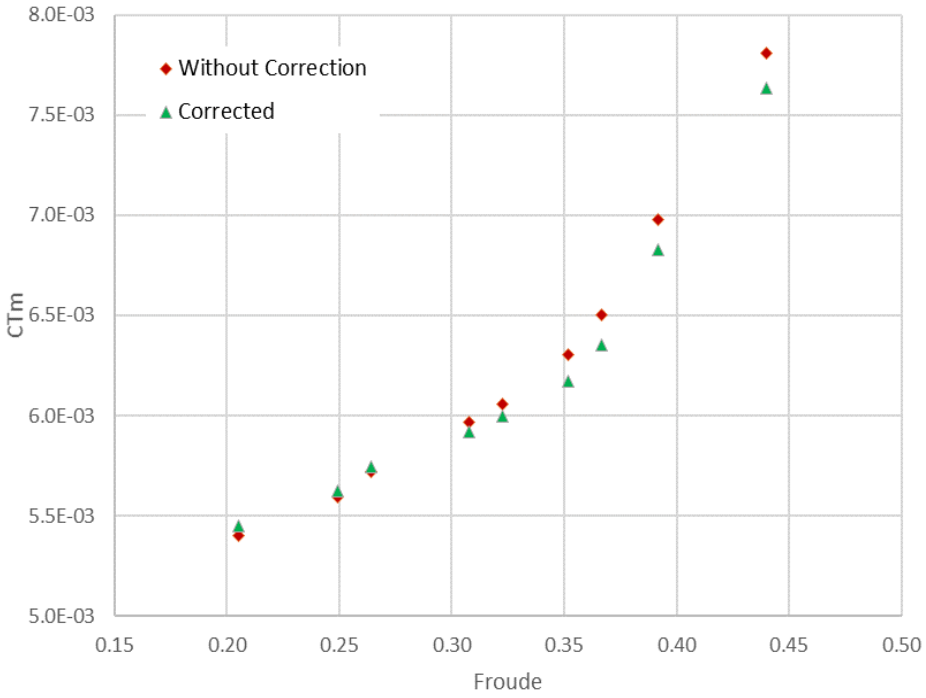

Figure 3-3: Comparison of the total resistance coefficient

At high speed flows, the flow tends to separate at the stern which results in a dry transom and a smaller wetted surface area. Therefore the new calculated wetted surface area is lesser than the nominal wetted surface area that was considered for all speeds. Therefore at high speeds, the friction resistance on the hull would be lesser than initially calculated as the resistance is directly proportional to the wetter surface area (Equation 3.4). This trend can be observed in Figure 3-1 where the corrected resistance coefficients at higher speeds is noticeably lesser than the coefficients without the correction. Therefore if the nominal surface area is used for the calculation of the friction resistance, it tends to under-predict or over-predict the resistance values depending on the speed. This suggests than the proposed correction to the resistance coefficients might give us a more accurate approximation.

The effect of the corrected wetted surface area can also be observed in the residuary resistance and the total resistance (Figure 3-1 and Figure 3-2), where the difference is more evident as the speed increases.

3.1.3 Validation of resistance

The experimental model data obtained at USNA is used to validate the numerical results. The calculated resistance coefficients are plotted as given below:

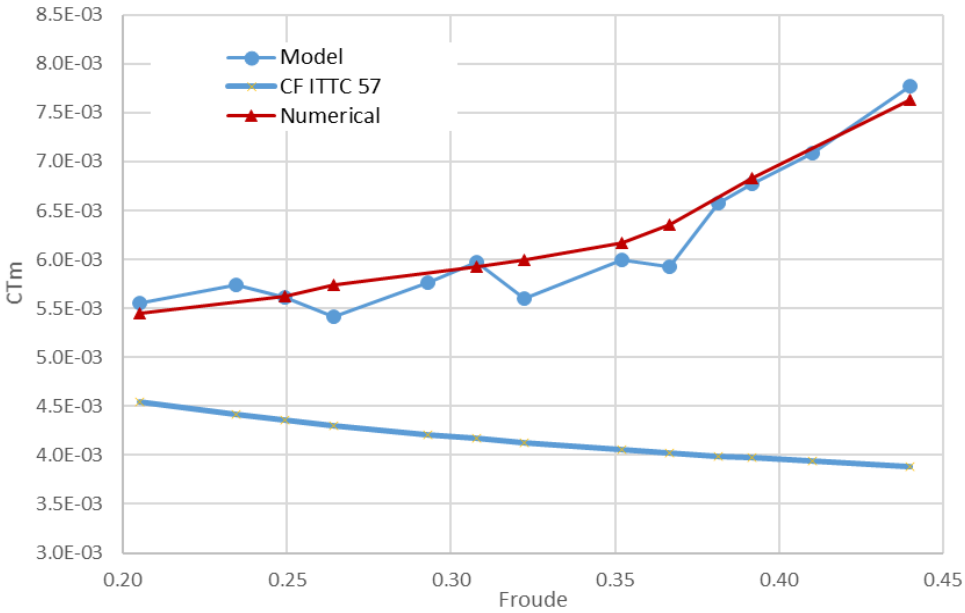

Figure 3-4: Total resistance coefficient vs Froude number

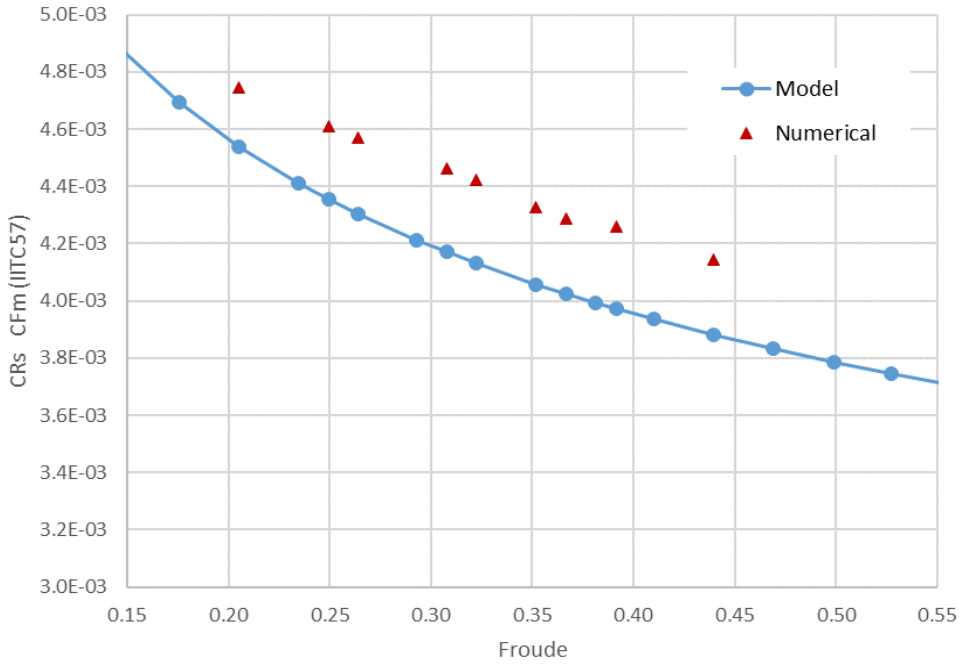

Figure 3-5: Shear resistance coefficient vs Froude number

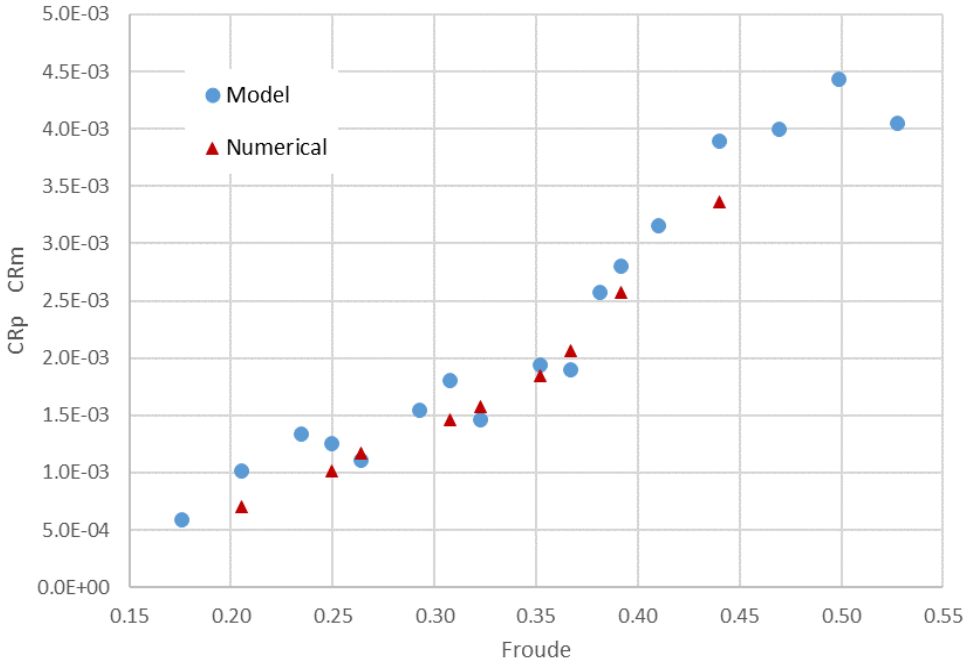

Figure 3-6: Pressure resistance coefficient vs Froude number

From the comparison plots (Figure 3-4 to 3-6), we observe good correspondence for the resistance results obtained from the numerical data from OpenFOAM and the model test data. From the total resistance co-efficient (Figure 3-4) and the residuary resistance co-efficient (Figure 3-6), we observe that OpenFOAM predicts the trend of the resistance values very well.

The friction resistance coefficient for the model tests is calculated using the ITTC-57 formula, which considers the friction coefficient of the ship to be equal to the friction coefficient of a flat plate with the same length as the ship. Therefore when the friction resistance coefficient is calculated in OpenFOAM over the actual form of the hull, the values might vary from the model data by a certain form factor. A form factor (k) value below 0.15 is considered to be acceptable. From the numerical shear resistance coefficient (Figure 3-5), we observe a maximum form factor of 0.07 for the friction coefficient at a speed of 0.440 Fr. Therefore from Figure 3-4 to 3-6 we can say that OpenFOAM provides an accurate prediction of the hull resistance.

3.2 Transom Wetness

3.2.1 Mid-plane

At high speeds, the flow around the hull is characterized by flow separation at the stern. To observe this, we plot the contour at the mid-plane as can seen below:

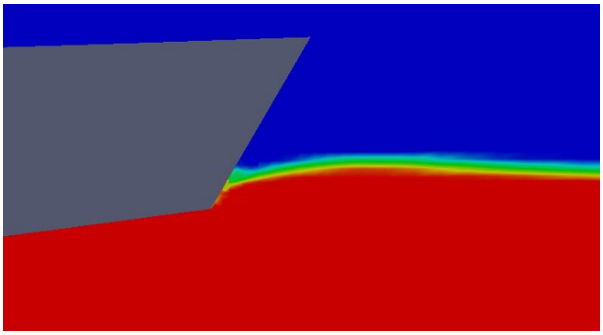

(a) Fr = 0.205

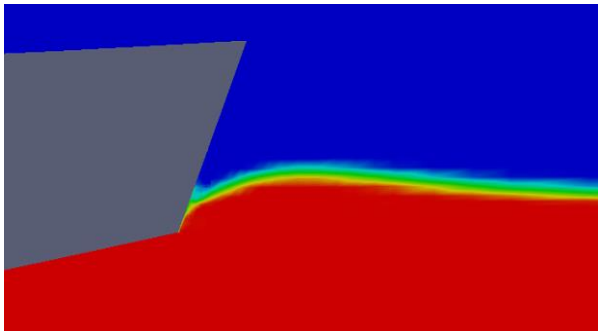

(b) Fr = 0.249

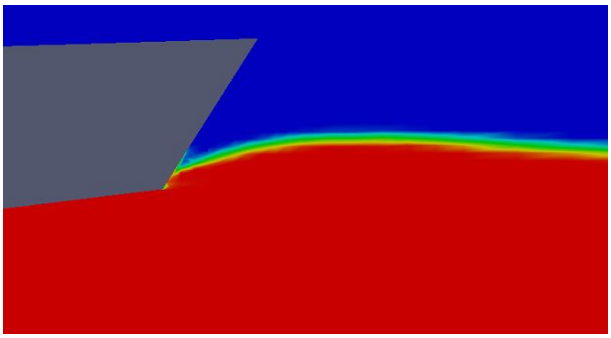

(c) Fr = 0.264

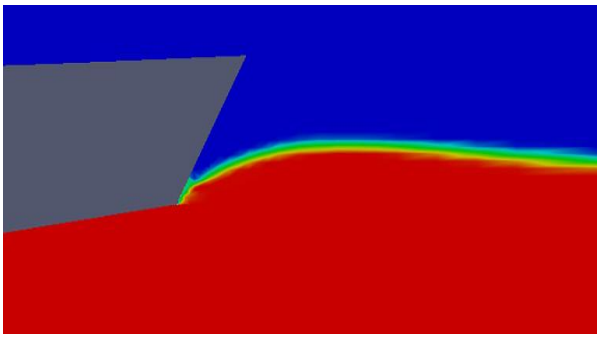

(d) Fr = 0.308

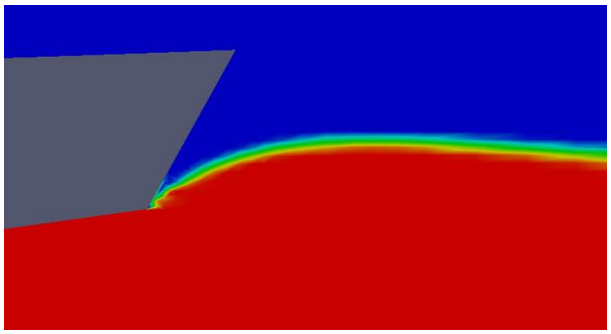

(e) Fr = 0.322

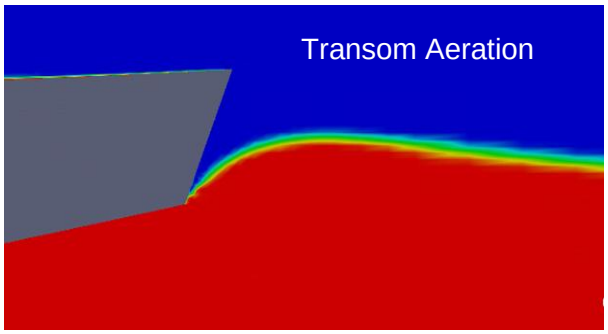

(f) Fr = 0.352

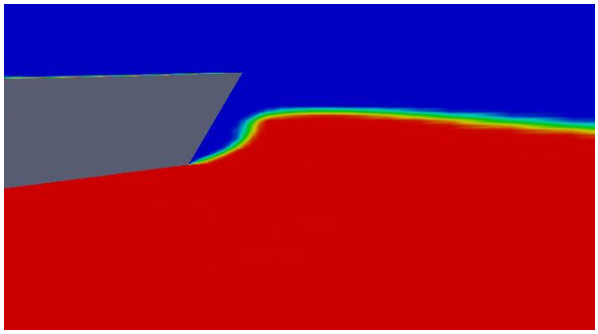

(g) Fr = 0.367

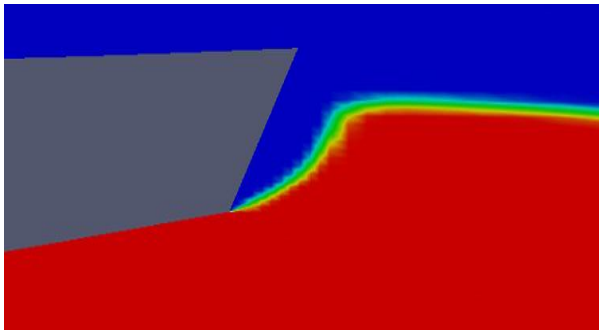

(h) Fr = 0.392

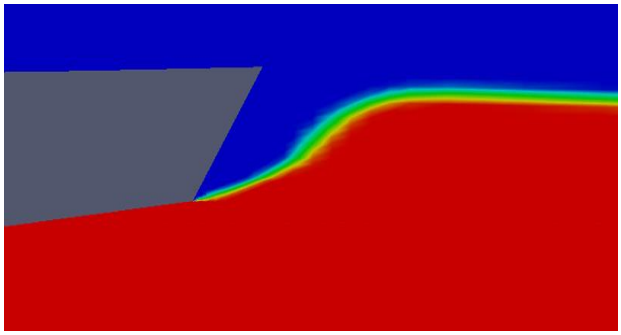

(i) Fr = 0.440

Figure 3-7: Transom un-wetting observed at the mid-plane

It is observed from Figure 3-7 that at low speeds the transom remains wet. At a speed of 0.352 Fr we observe the transom aeration which transitions to a dry transom. The flow separation at the stern is visualized at the higher speeds.

3.2.2 Wetted surface area

In Section 3.1.2 a correction is made to the resistance coefficients using a modified wetted surface area. This new wetted surface area (S^N) is calculated using ParaView, and the values are plotted in Figure 3-8. We observe that the transom is dry for speeds of 0.352 Fr and above.

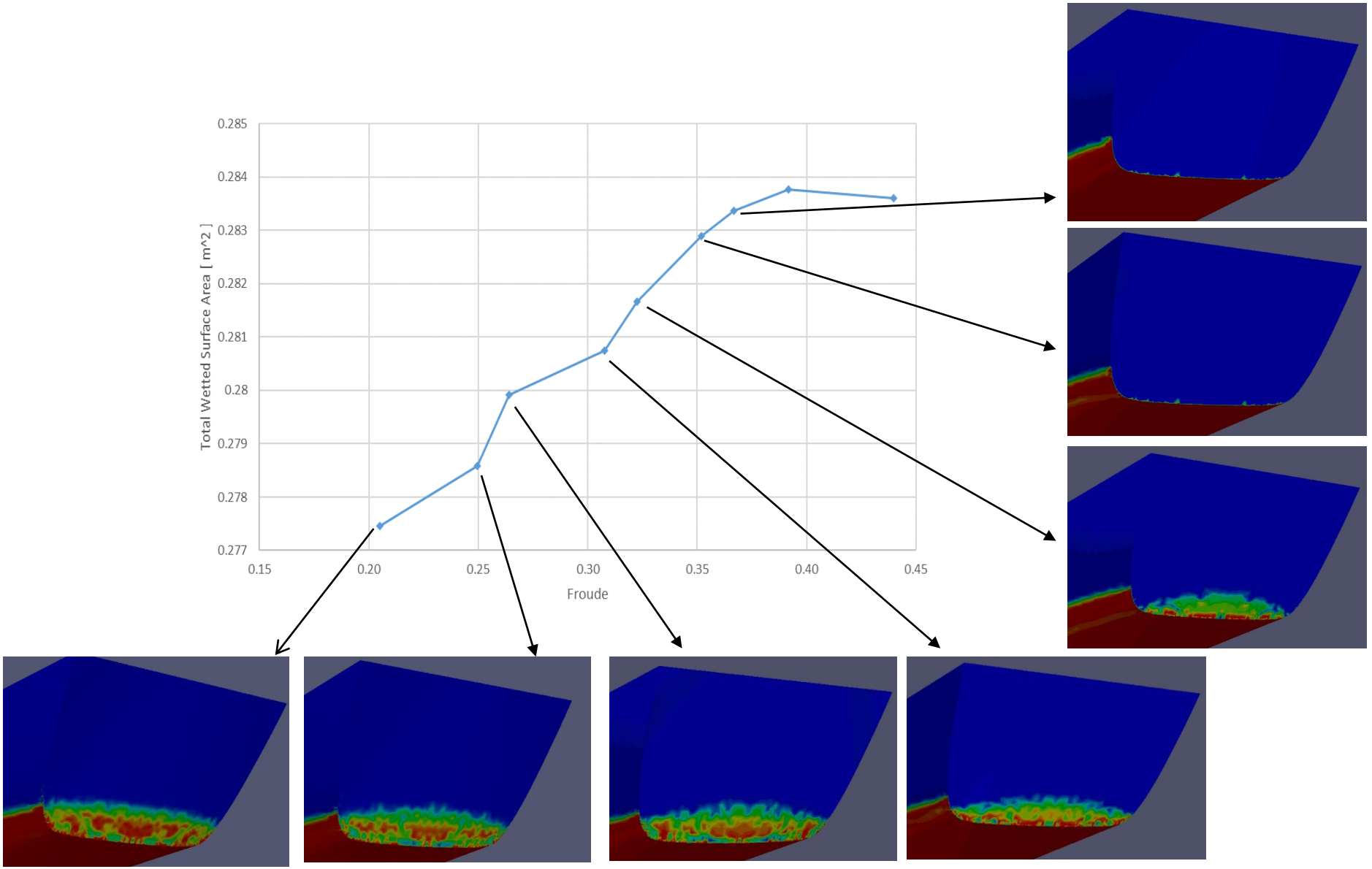

Figure 3-8: Hull wetted surface (excluding transom) and transom clearance as a function of speed. Red = fully wet; Blue = fully aerated; Green 50% wet (wet by a foamy 50% air/water mixture)

3.3 Skin friction co-efficient

Since we know that the un-wetting of the transom occurs between the speed range of 0.322 Fr and 0.352 Fr, we visualize the contour of the skin friction co-efficient on the surface of the hull. The skin friction will help visualize the development of the flow around the hull as the flow begins to separate at the stern.

Skin friction drag is the resistance exerted on the hull by the water, due to the viscosity of the fluid medium. The *skin resistance co-efficient* (C_f) is given as:

$$C_f = \frac{\tau_\omega}{0.5 * \rho * V^2} \tag{3.8}$$

Where, τ_ω is the wall shear stress, ρ is the density and V is the free stream velocity.

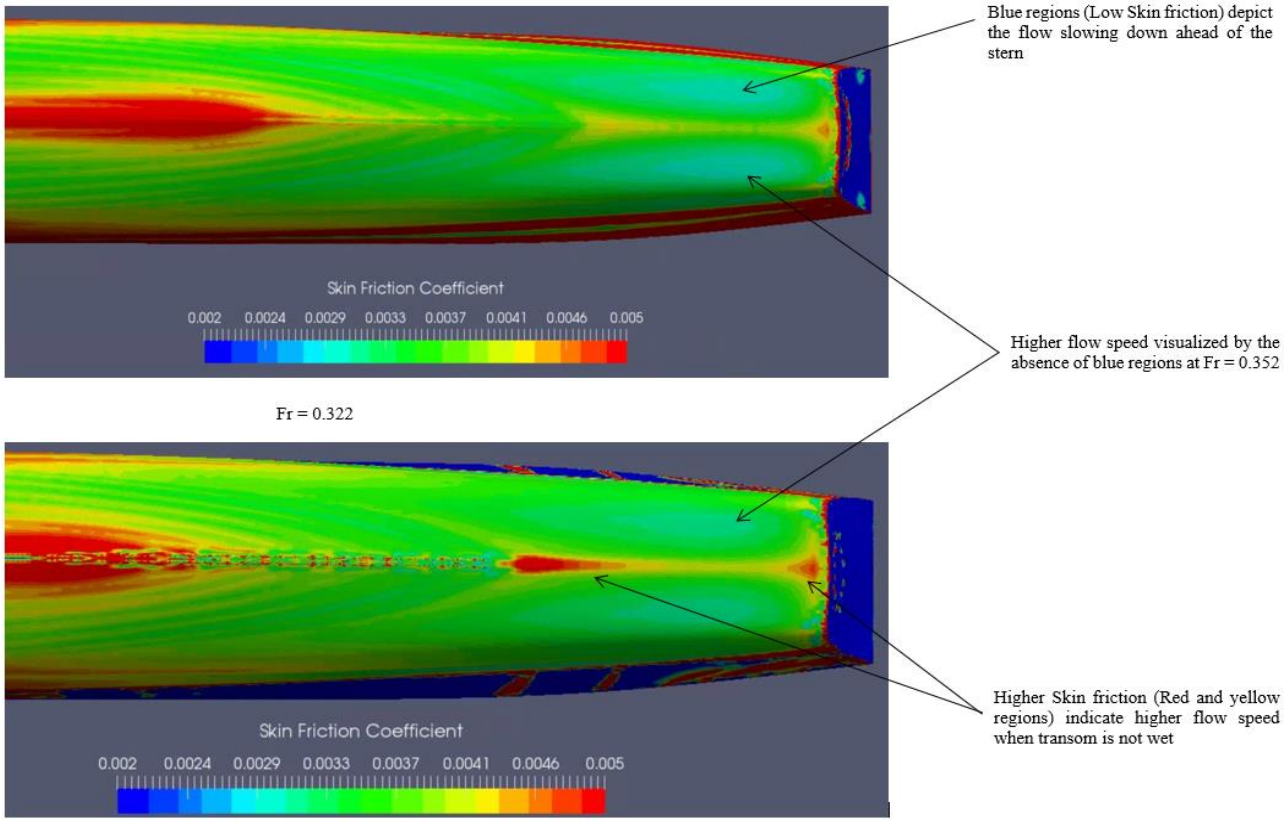

Figure 3-9: Effect of transom un-wetting on Skin Friction coefficient at Fr =0.322 (top) and Fr = 0.352 (bottom)

From the skin friction contours (Figure 3-9), we can confirm that at a speed of Fr=0.352, there is a clear increase in the flow speed along the hull as indicated by the higher skin friction. Therefore the higher flow speeds that result in the observed dry transom, also increase the friction resistance acting on the hull. Therefore this suggests that the un-wetting of the transom affects the flow around the hull and/or the characteristics of the hull motion.

3.4 Free surface wave

The contour for the free surface wave is visualized in ParaView to see the development of the wave as a function of the speed.

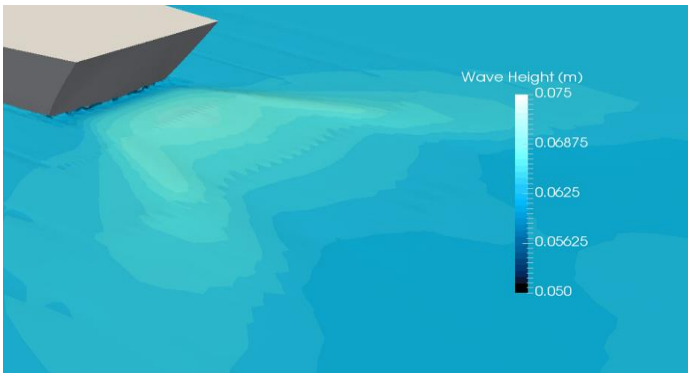

(a) Fr = 0.205

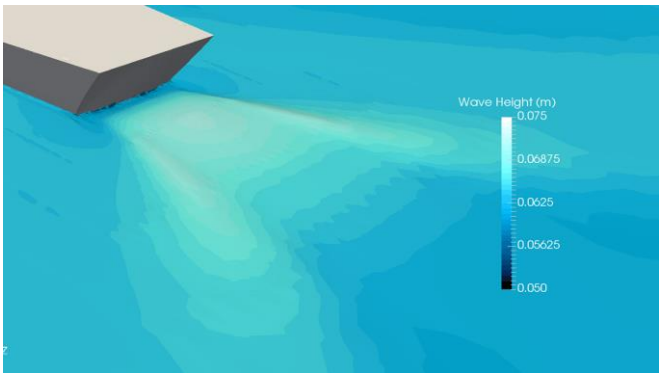

(b) Fr = 0.249

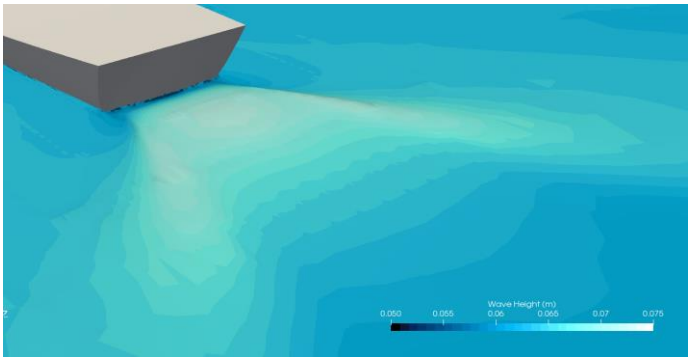

(c) Fr = 0.264

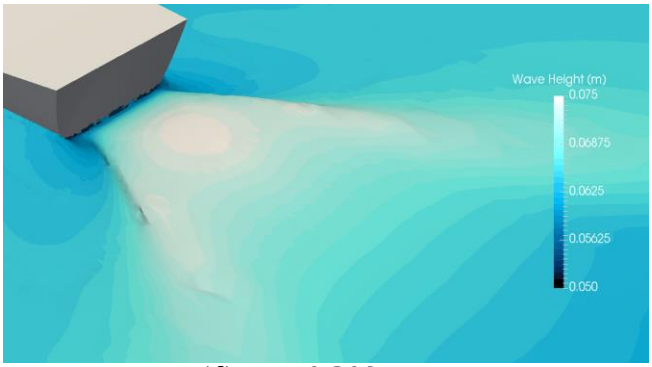

(d) Fr = 0.308

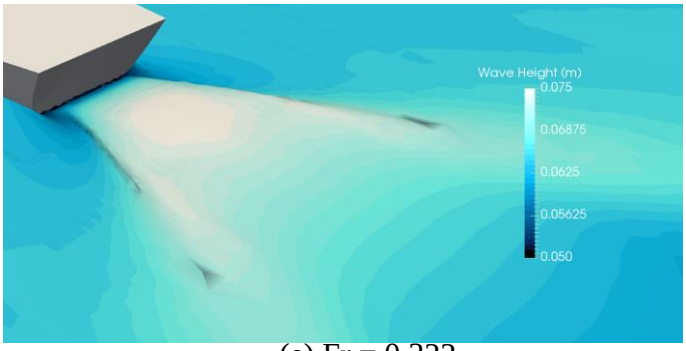

(e) Fr = 0.322

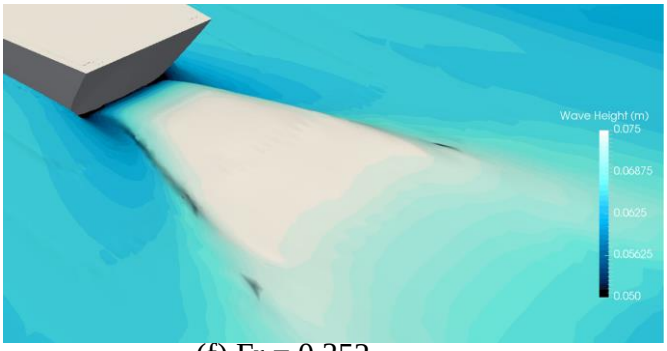

(f) Fr = 0.352

(g) Fr = 0.367

(h) Fr = 0.392

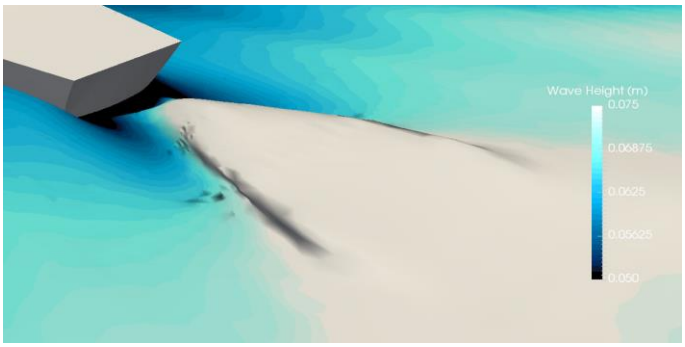

(i) Fr = 0.440

Figure 3-10: Free surface wave at the stern

From Figure 3-10 we can observe that the shape of the free surface wave begins to change as the speed increases. A perceivable change can be observed at the speed where the transom get un-wet. For the dry transom, there is a hollow region at the transom where the flow separates from the stern. The flow then begins converging and forming a wave in the shape of a rooster tail as the speed keeps increasing.

3.5 Pressure distribution

The pressure distribution is plotted on hull by calculating the dynamic pressure co-efficient. The presented dynamic pressure coefficient *Cp* is calculated subtracting the hydrostatic pressure head *ρgz* from the computed total pressure, i.e.:

$$C_p = \frac{p_{tot} - \rho g z}{0.5 * \rho * S * V^2} \tag{3.9}$$

Where, z is the vertical distance of every point of the hull, from the calm water surface.

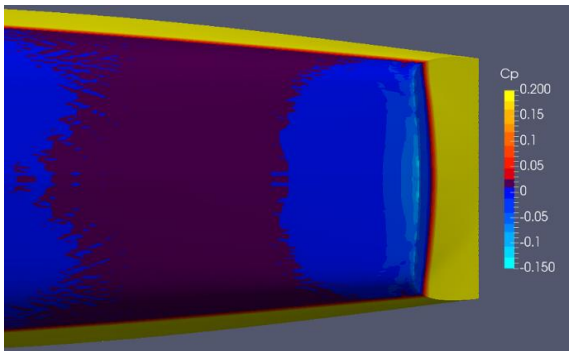

(a) Fr = 0.205

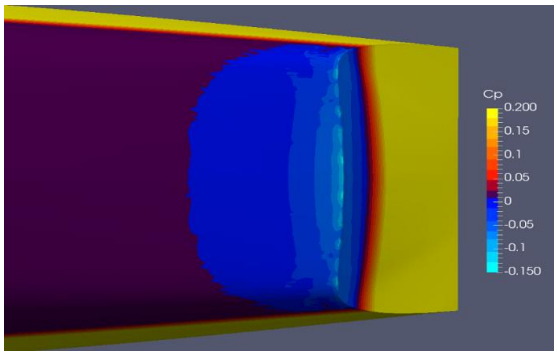

(b) Fr = 0.249

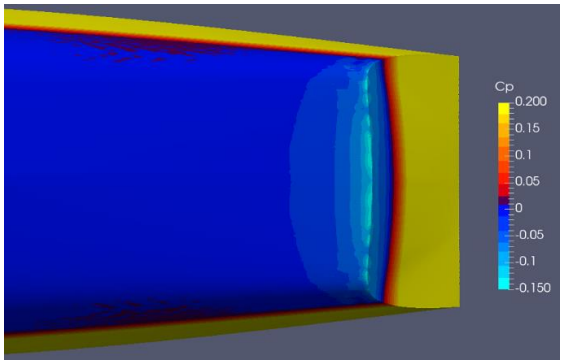

(c) Fr = 0.264

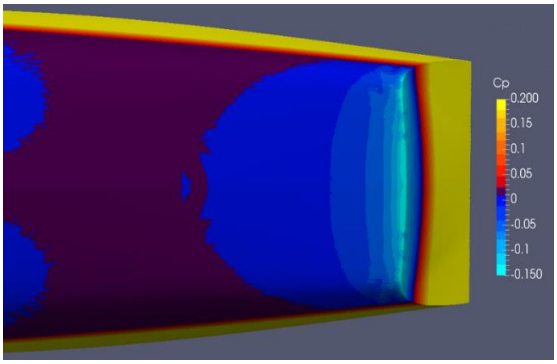

(d) Fr = 0.308

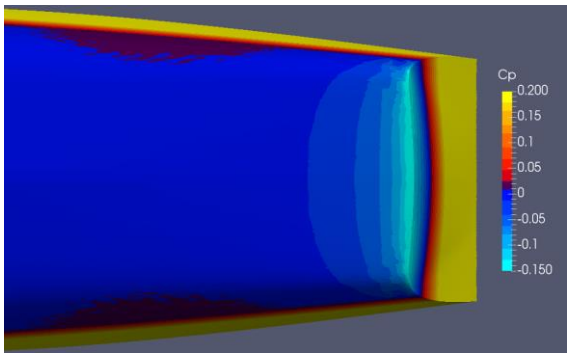

(e) Fr = 0.322

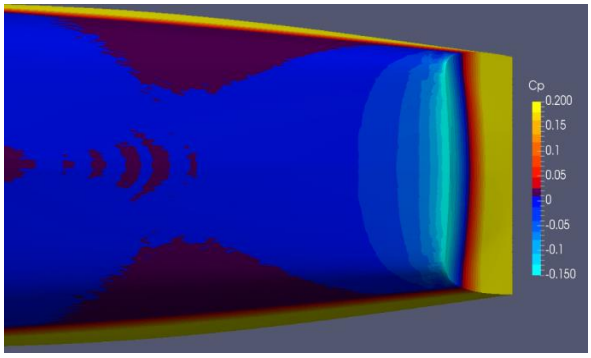

(f) Fr = 0.352

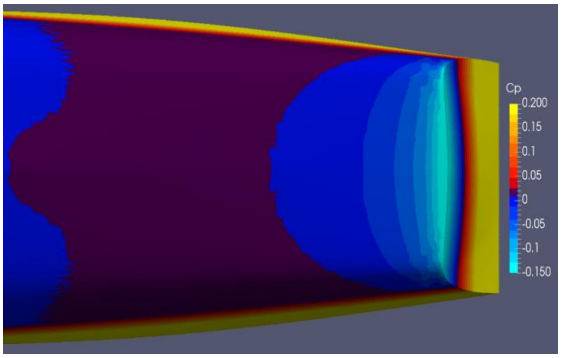

(g) Fr = 0.367

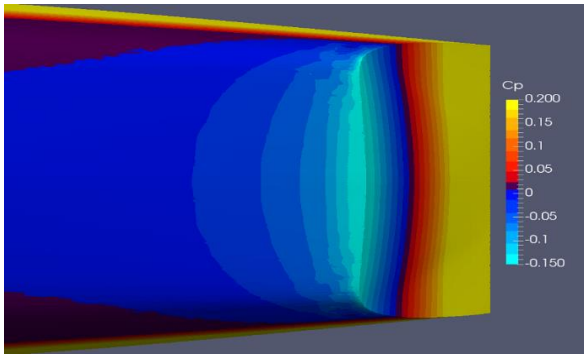

(g) Fr = 0.392

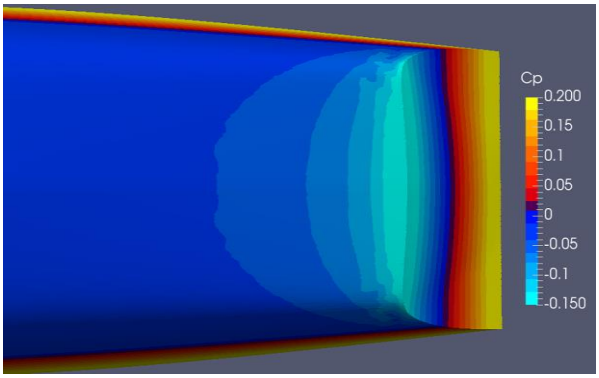

(i) Fr = 0.440

Figure 3-11: Pressure coefficient on the hull

From Figure 3-11 we observe a negative pressure coefficient along the transom edge which increases in area and magnitude as the speed increases. This negative (suction) dynamic pressure steeply increases its magnitude as one approaches the transom edge, causing a concentrated low pressure region at the very aft end of the hull. At a speed of Fr = 0.352 and higher, we observe a large increase in the magnitude of the negative pressure. From the skin friction contours (Figure 3-9), we can confirm that from a speed of Fr = 0.352, there is a clear increase in the flow speed along the hull as indicated by the higher skin friction. Therefore the higher flow speeds that result in the observed dry transom, also increase the friction resistance acting on the hull.

As it is well known, when the transom is dry (the flow sharply separates from the transom edge), as it is the case for Fr=0.392, the total pressure at the transom edge must be atmospheric. This corresponds to a dynamic pressure coefficient $Cp \sim -0.20$, calculated subtracting the hydrostatic pressure head referenced to the calm water level from the calculated total pressure.

This negative dynamic pressure is the cause for the high dynamic trim by stern and dynamic sinkage that is observed at high speeds. These phenomena, in fact, are known to be originated by the high speed flow around the hull and intensifies with an increase of ship speed.

3.6 Hull Motion

For the reference experimental model tests conducted at the NAHL, the model was fit with a pitch pivot and attached to a heave post on the towing rig. The model was free to heave and pitch. Heave and pitch were measured with a pair of potentiometers located at the model's LCB.

Therefore the solver in OpenFOAM is setup so as to calculate the pitch and heave of the model about the LCB. The running trim is defined as positive for bow-up motion, and the CG rise is positive when the displacement of the hull at the LCG location is upward (opposite of sinkage). Comparing the numerical results to the model tests, we

observe good correspondence between the trim and sinkage values, considering the uncertainty of the model test measurements, as seen in Figure 3-12 and Figure 3-13.

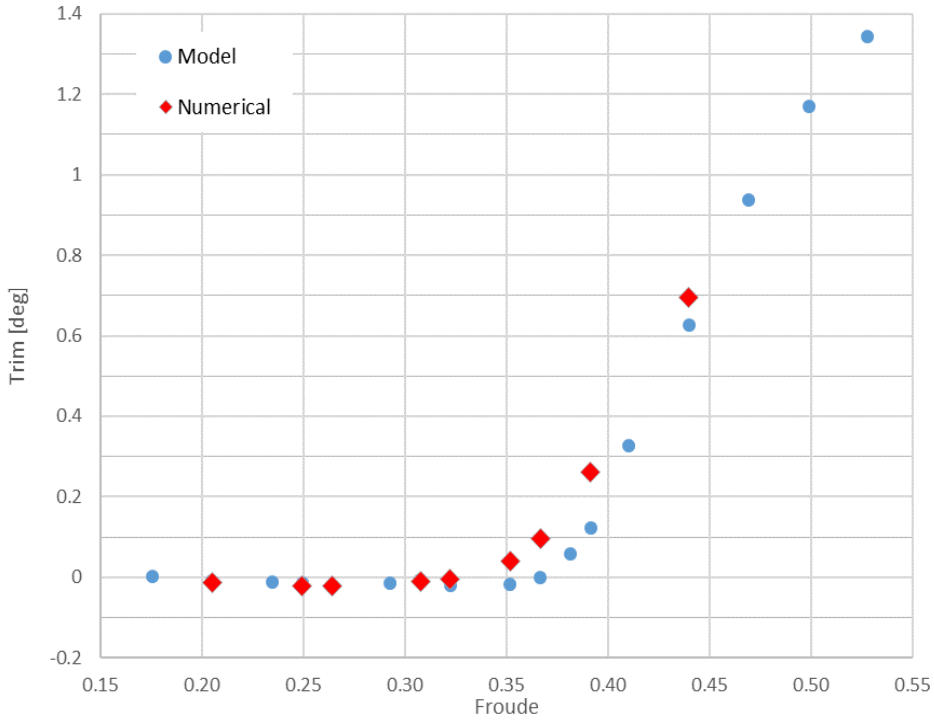

Figure 3-12: Dynamic trim angle

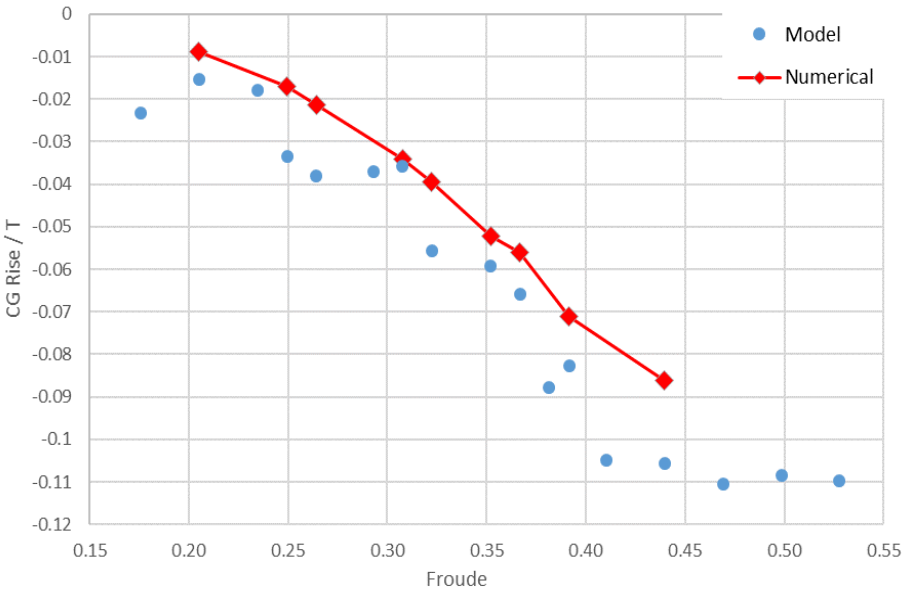

Figure 3-13: CG rise of the hull

CHAPTER 4

INTERCEPTOR

An interceptor is a flat plate that is fitted vertically at the transom of a ship and protrudes below the transom. As per Brizzolara (2003) [7], it is evident that the boundary layer thickness is an important factor in determining the interceptor height. The interceptor should be contained entirely within the boundary layer, and so a L/h = 400 was identified as a suitable maximum height for the interceptor in this case. A height of 0.00375 *m* and a span of 0.07747 *m* is selected as the largest interceptor (in terms of height and span). The height of the interceptor is approximately 1/10 the calculated boundary layer thickness and therefore the interceptor is contained well within the boundary layer. For turbulent flow at Reynolds number of model scale, the boundary layer thickness is estimated by the following equation:

$$\delta(x) = 0.37 \times {Re_x}^{-1/5} \tag{4.1}$$

Where, x is the longitudinal position along the hull and Re_x is the Reynolds number at the given length x.

4.1 Meshing

The geometric CAD design is prepared on Rhinoceros by adding an interceptor with a height of 0.00375 *m* and a span of 0.07747 *m*, to the barehull model. A comparison of the barehull model and the model with the interceptor is given in *Figure 4-1* below:

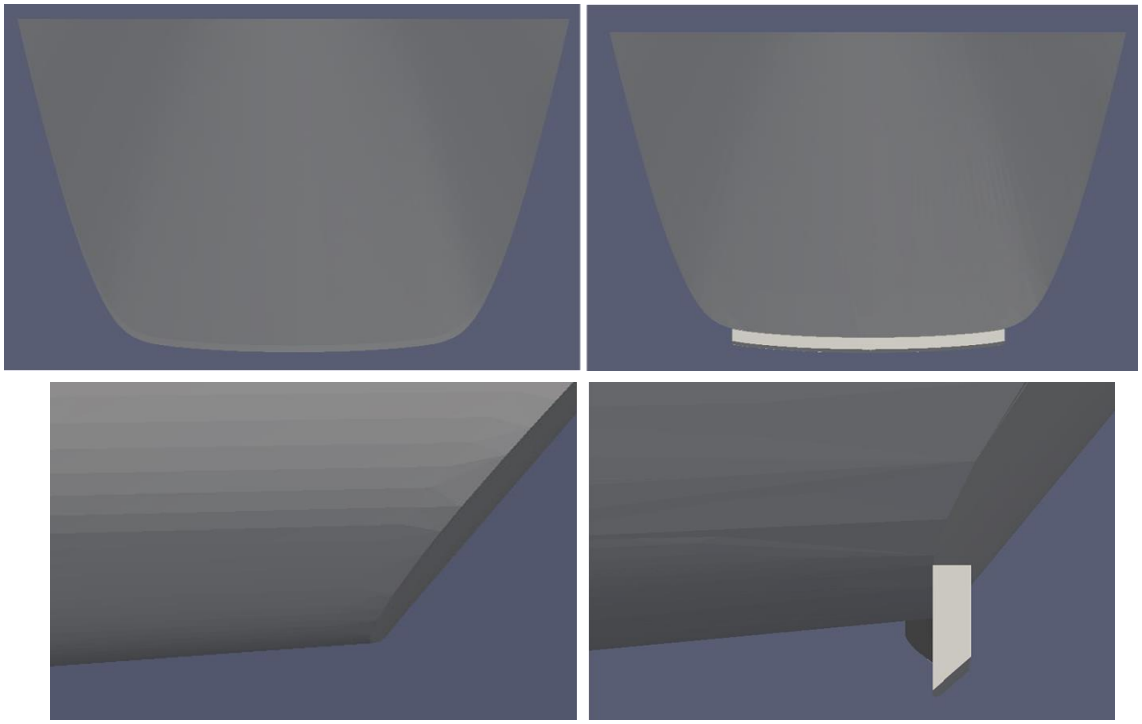

Figure 4-1: Bare transom geometry (left) and full span interceptor fitted on it (right)

The mesh is prepared using the in-built OpenFOAM mesh generation tools, *blockMesh* and *snappyHexMesh*, similar to the procedure described in Section 2.3. Since it is important to solve the various parameters and the flow well in the region around the interceptor, a further refinement was made over the barehull mesh. A local refinement in the proximity of the interceptor blade in order to resolve the flow field variation along the interceptor height. This is done by defining a refinement box in the *snappyHexMeshDict*. A comparison of the refinement at the transom between the barehull and the interceptor meshes is shown in Figure 4-2 and Figure 4-3. A close up of the surface mesh around the interceptor is given in Figure 4-4.

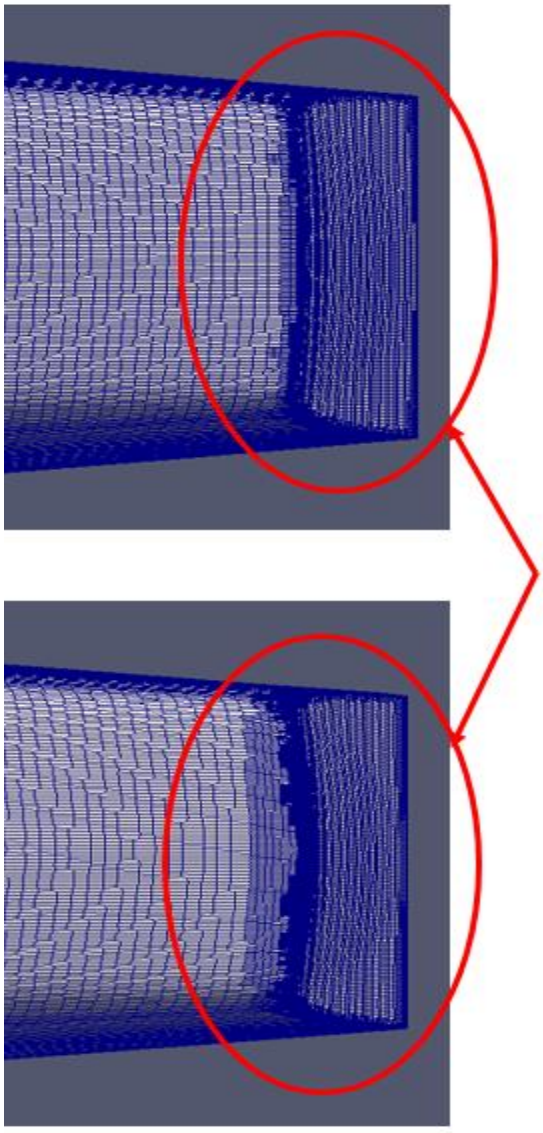

Comparison of the barehull (top) and interceptor (bottom) meshes, with the added local refinement for the interceptor

Figure 4-2: Comparison of the generated meshes

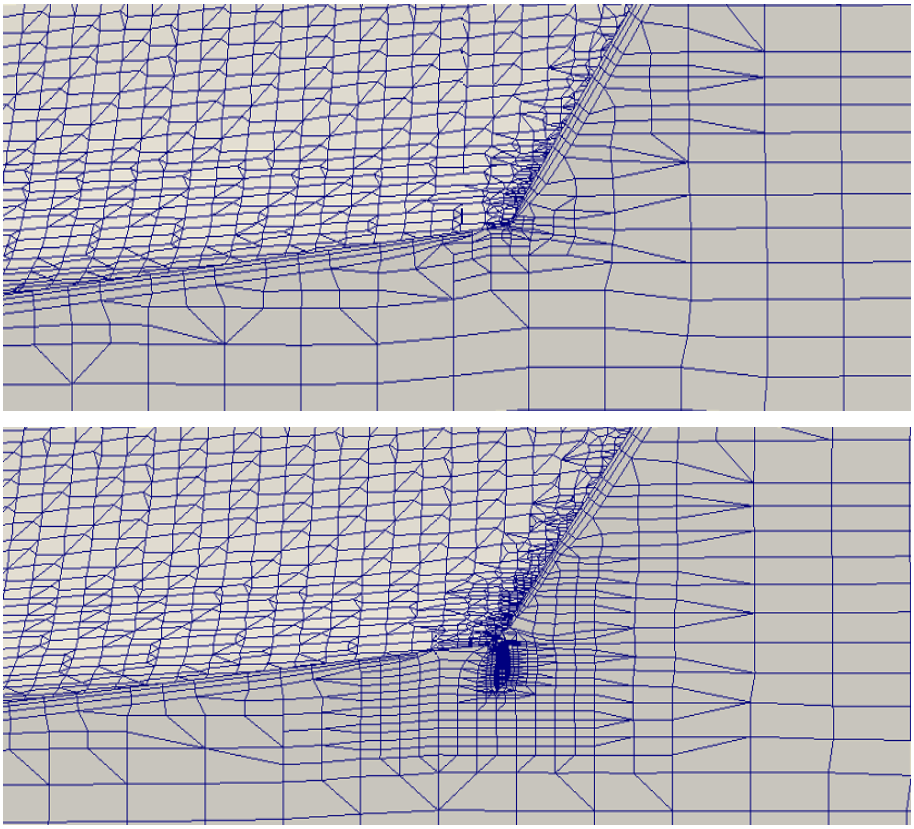

Figure 2-3: Comparison of the barehull (top) and interceptor (bottom) meshes at the mid-plane

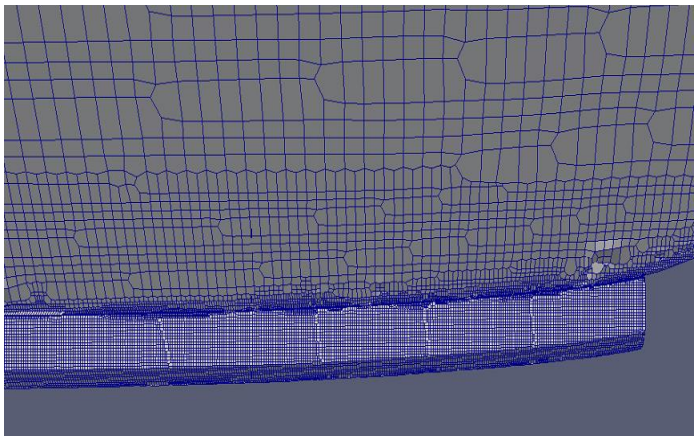

Figure 4-4: Mesh refinement at the interceptor

4.2 Resistance Comparison

The resistance coefficients for the interceptor cases are calculated using the same method as used for the barehull model calculations defined in Section 3.1.1. The correction made to the calculation of the friction resistance coefficient described in Section 3.1.2 is also applied to the interceptor results. Since the interceptor plates protrude vertically down from the transom, it adds to the friction resistance acting on the hull. Therefore while calculating the new wetted surface area (S^N) for the correction in the resistance, the area of the interceptor was accounted for.

Simulations with the interceptor model are run across the same tested speeds of Fr= 0.205 to Fr = 0.44. The comparison of the resistance between the interceptor and barehull models are given in Figure 4-5 to Figure 4-7.

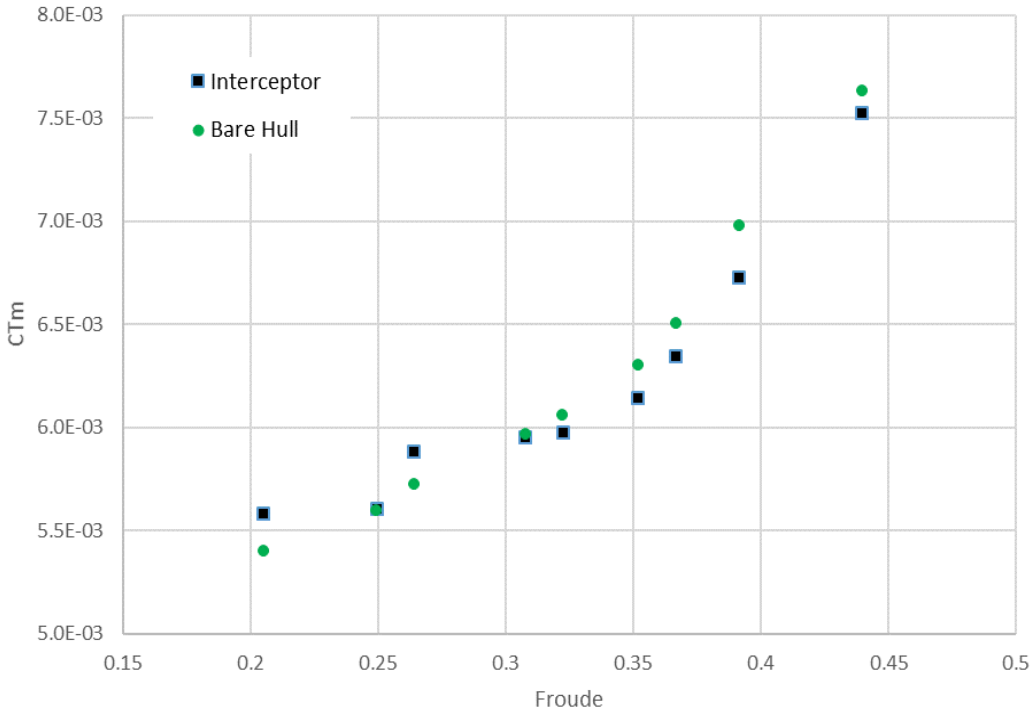

Figure 4-5: Total resistance coefficient comparison of Interceptor vs Barehull

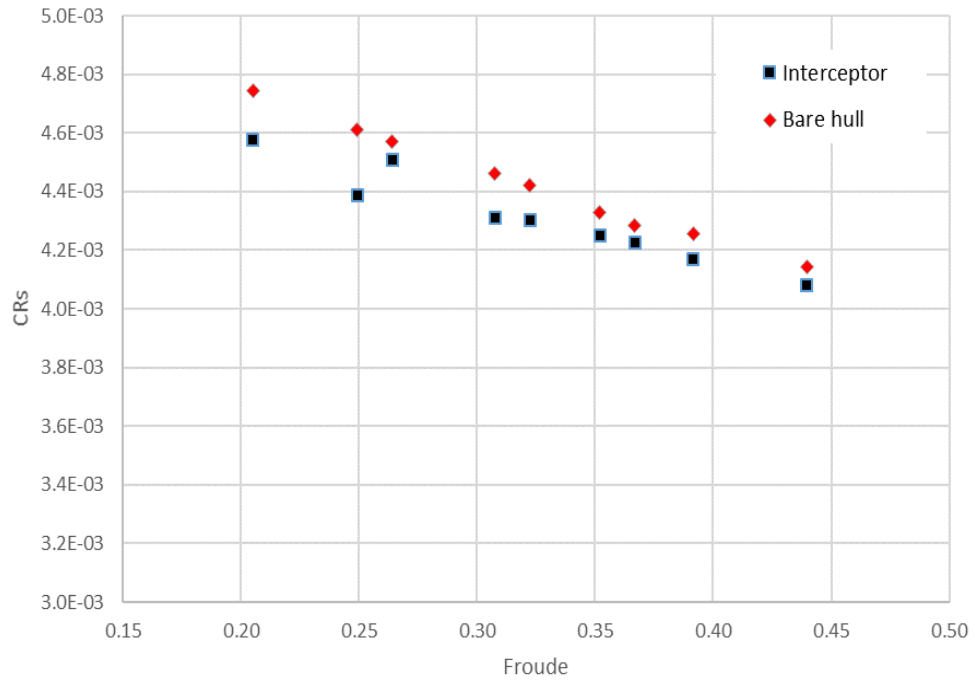

Figure 4-6: Shear resistance coefficient comparison of Interceptor vs Barehull

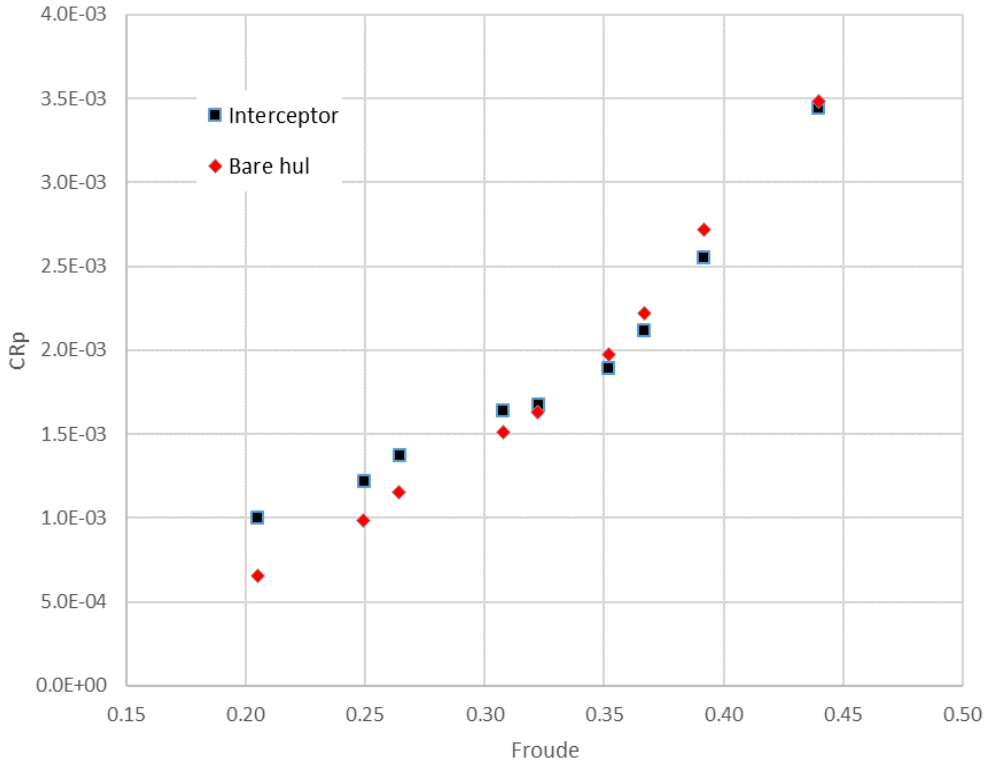

Figure 4-7: Pressure resistance coefficient comparison of Interceptor vs Barehull

From the total resistance coefficient comparison (Figure 4-5), we can see that as expected the interceptor increases the resistance acting on the hull at low speeds, but reduces the resistance at medium to high speeds. From the plot we can see the crossover point after which the resistance begins decreasing is around the speed of Fr = 0.308. Therefore above the speed of 0.308 Fr is when we get an effective improvement in the performance and powering due to the addition of the interceptor. We observe the best improvement in performance at a speed of Fr = 0.392, where the interceptor results in a 3.76% decrease in the total resistance coefficient.

The interceptor causes a change in the motion of the ship (with regards to the trim and sinkage), which in turn results in a change in the wetted surface area of the hull. This affects the friction resistance acting on the hull, as can be seen in Figure 4-6, where the friction resistance coefficient with the interceptor is found to be lower than the bare hull across the speed range.

The difference in the resistance values are listed in Table 4-1.

Table 4-1: Resistance comparison between interceptor and bare hull

Froude No.	V (m/s)	CTm			CRs			CRp		
		Barehull	Int.	% diff.	Barehull	Int.	% diff.	Barehull	Int.	% diff.
0.205	0.80467	0.00540	0.00558	3.24	0.00470	0.00454	-3.59	0.00070	0.00104	32.92
0.249	0.97841	0.00559	0.00561	0.23	0.00459	0.00437	-4.97	0.00101	0.00124	18.64
0.264	1.03632	0.00572	0.00588	2.73	0.00455	0.00451	-1.05	0.00117	0.00138	15.12
0.308	1.20701	0.00597	0.00595	-0.32	0.00450	0.00435	-3.39	0.00147	0.00160	8.03
0.322	1.26492	0.00606	0.00598	-1.34	0.00447	0.00434	-2.94	0.00159	0.00164	2.91
0.352	1.38074	0.00630	0.00614	-2.62	0.00442	0.00432	-2.37	0.00188	0.00182	-3.22
0.367	1.43866	0.00651	0.00634	-2.55	0.00439	0.00430	-2.03	0.00212	0.00204	-3.64
0.392	1.53619	0.00698	0.00673	-3.76	0.00435	0.00427	-1.91	0.00263	0.00245	-7.00
0.440	1.72517	0.00763	0.00753	-1.38	0.00424	0.00417	-1.73	0.00339	0.00336	-0.94

4.3 Trim and Sinkage Comparison

The interceptor alters the flow of the water which results in a high pressure region in front of the blade. This causes a lift force acting upwards on the hull, which influences the trim and sinkage.

The running trim is defined as positive for bow-up motion, and the CG rise is positive when the displacement of the hull at the LCG location is upward (opposite of sinkage). The comparison of the trim and sinkage between the interceptor and barehull models are given in Figure 4-8 and Figure 4-9.

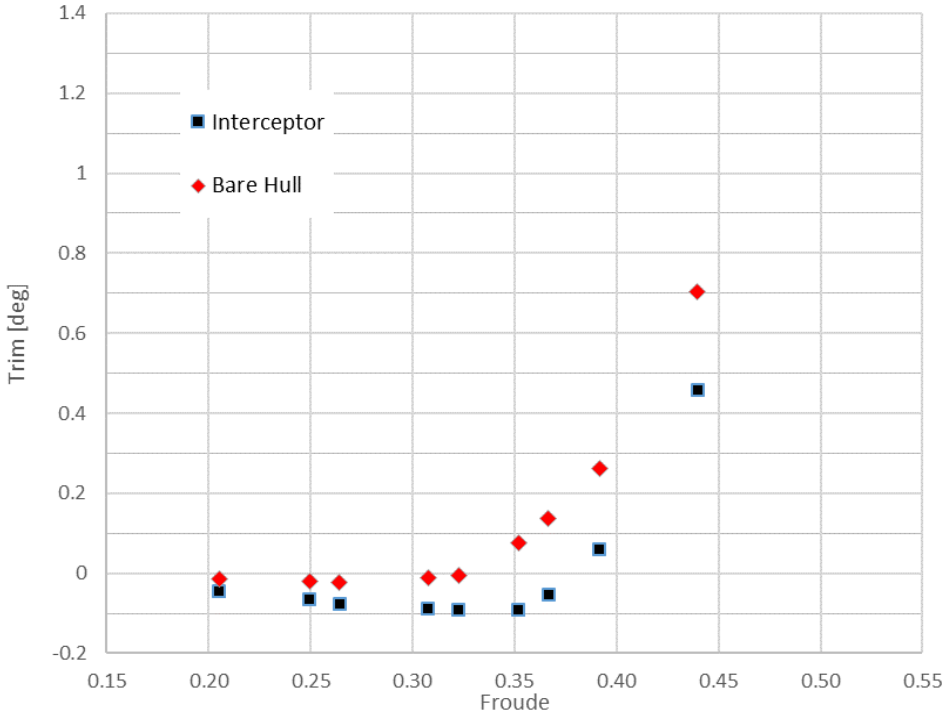

Figure 4-8: Trim comparison between interceptor and bare hull models

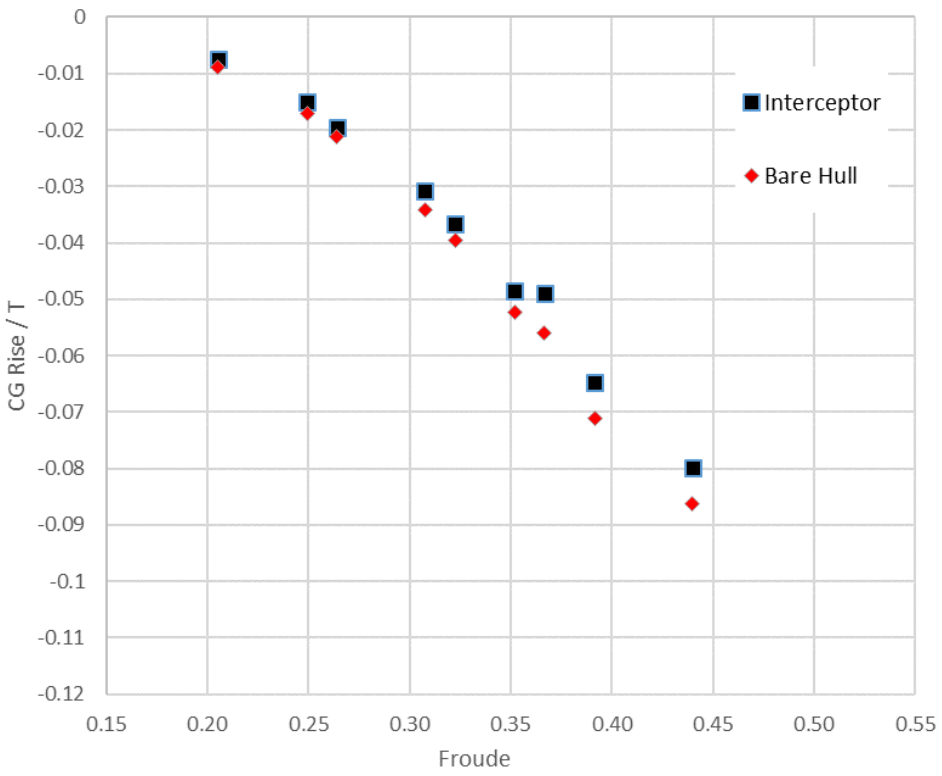

Figure 4-9: CG rise comparison between interceptor and bare hull models

From the trim comparison in Figure 4-8, we observe that the interceptor results in a decrease in trim across the speed range tested. A negative trim (decrease) signifies a bow down motion of the hull which is generally characterized by a decrease in resistance. This corresponds with the resistance results we observe in the previous section, where there is a decrease in the shear resistance coefficient across the speed range (Figure 4-6).

From the sinkage (CG rise) comparison in Figure 4-9, we observe less sinkage across the speed range when the interceptor is used. The reduced trim and sinkage observed with the usage of an interceptor results in a decrease in the wetted surface area of the hull. The outcome of this is lesser friction resistance acting on the hull.

At low speeds an increase in total resistance (Figure 4-5) is still observed since the added drag due to the interceptor is greater than the reduction in resistance due to the change in sailing attitude. At higher speeds however, since there is a significant reduction in the trim and sinkage, we observe an overall decrease in the total resistance.

The difference in the trim and sinkage values are listed in Table 4-2.

Table 4-1: Hull motion comparison between interceptor and bare hull

Froude No.	V (m/s)	Trim (deg)		CG rise/ T	
		Barehull	Int.	Barehull	Int.
0.205	0.80467	-0.014	-0.0435	-0.0088	-0.0076
0.249	0.97841	-0.021	-0.0643	-0.0170	-0.0150
0.264	1.03632	-0.023	-0.0759	-0.0212	-0.0196
0.308	1.20701	-0.011	-0.0888	-0.0341	-0.0308
0.322	1.26492	-0.004	-0.0924	-0.0395	-0.0367
0.352	1.38074	0.041	-0.0916	-0.0523	-0.0485
0.367	1.43866	0.095	-0.0531	-0.0559	-0.0490
0.392	1.53619	0.261	0.0594	-0.0710	-0.0648
0.440	1.72517	0.694	0.4577	-0.0862	-0.0800

4.4 Pressure distribution

The dynamic pressure coefficient is calculated and plotted on the hull in ParaView. The presented dynamic pressure coefficient *Cp* is calculated subtracting the hydrostatic pressure head *ρgz* from the computed total pressure, i.e.:

$$C_p = \frac{p_{tot} - \rho g z}{0.5 * \rho * S * V^2} \tag{4.2}$$

Where, z is the vertical distance of every point of the hull, from the calm water surface.

The pressure distribution, *Cp*, contour plots across the whole hull viewed from the bottom, and the *Cp* plots near the transom, are given below for the speed range.

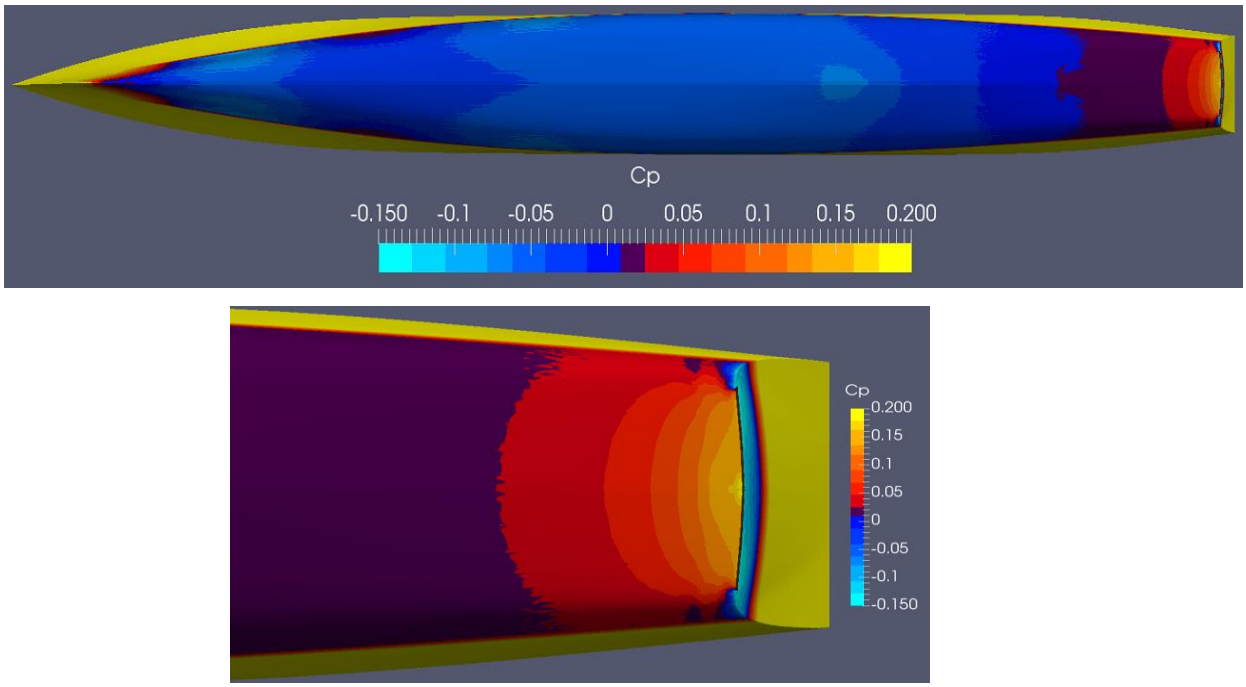

(a) Fr = 0.205

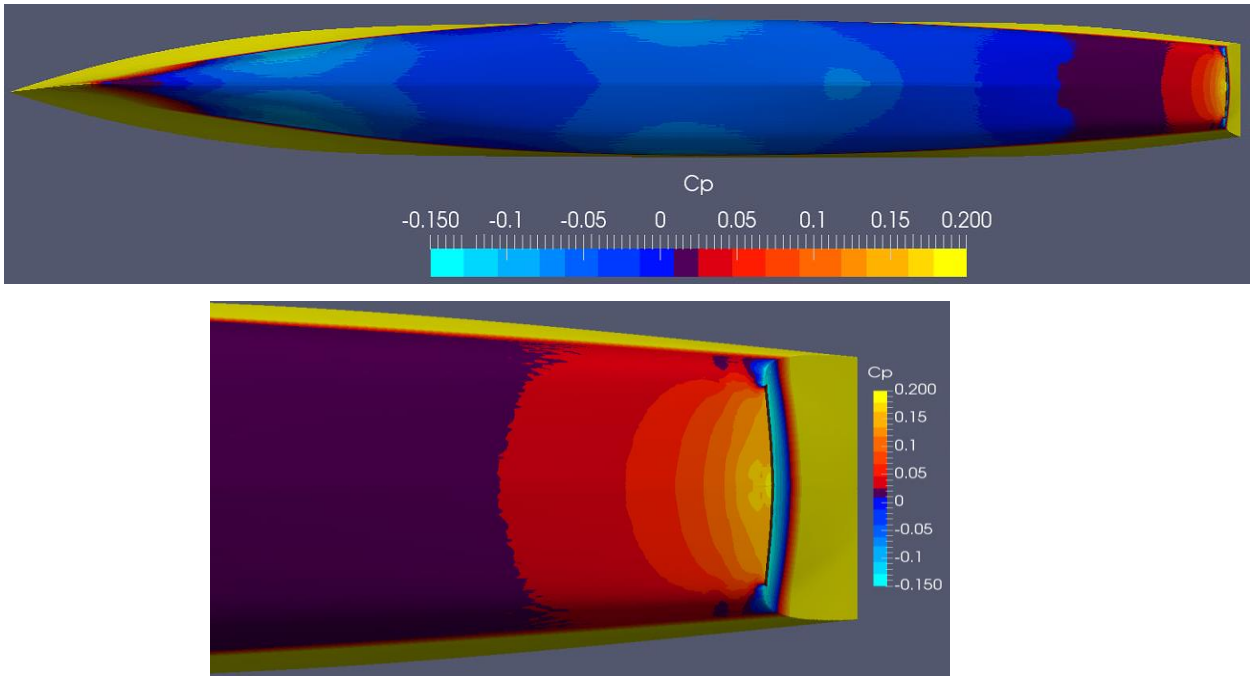

(b) Fr = 0.249

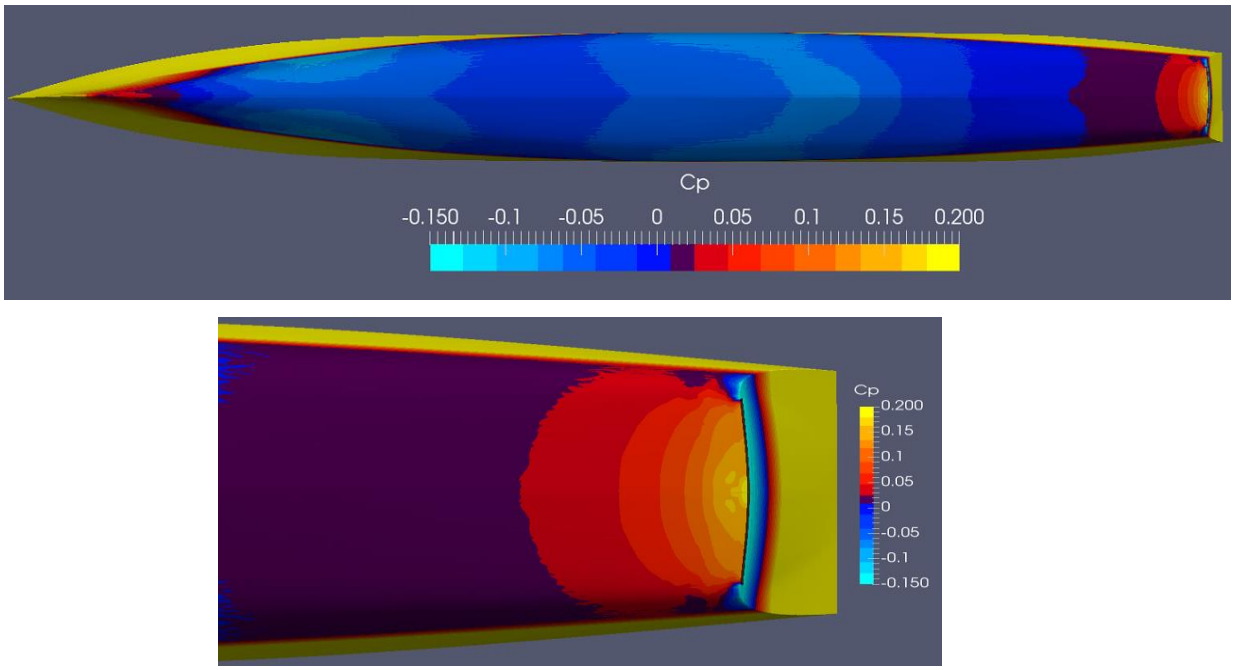

(c) Fr = 0.264

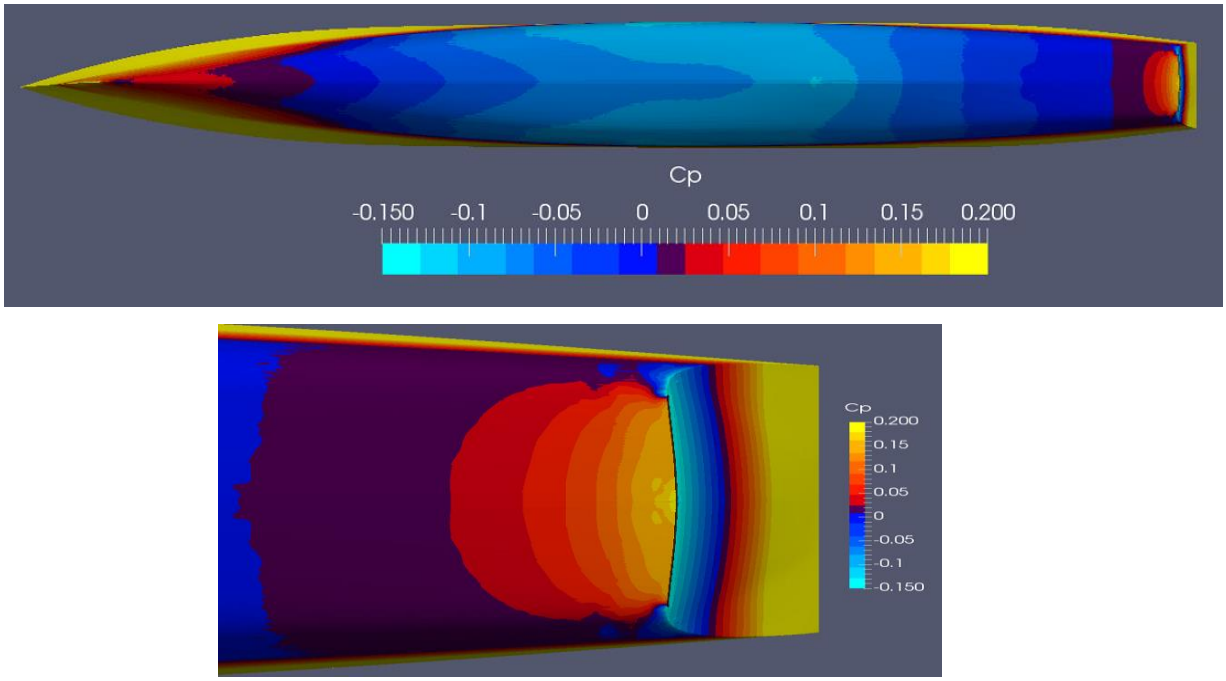

(d) Fr = 0.392

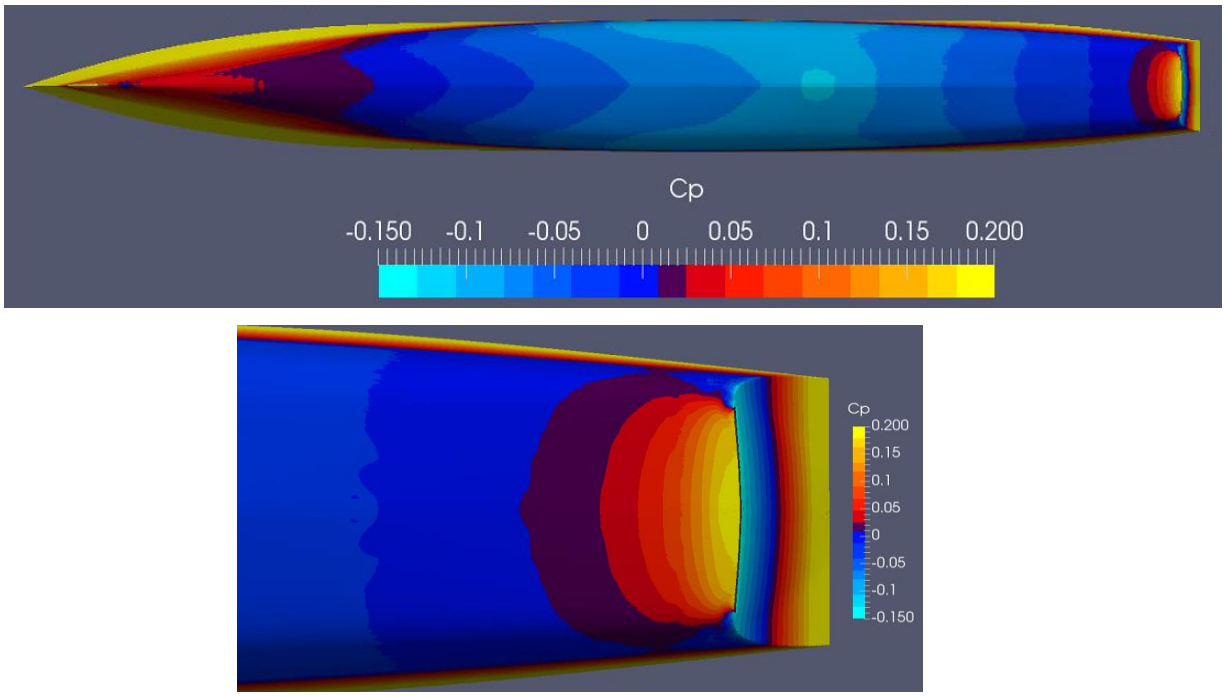

(e) Fr = 0.440

Figure 4-10: Pressure coefficient on the hull with interceptor

From the pressure distribution contour plots we can see that similar to the barehull pressure distribution, the interceptor cases too have a large negative pressure coefficient at the midship. In the barehull cases this negative pressure extends till the stern, where at the stern edge the magnitude of the negative pressure coefficient steeply increases.

From Figure 4-10 however, we can observe the effect of the interceptor on the pressure coefficient ahead of the interceptor plate. The interceptor blocks the flow of water resulting in a high pressure region ahead of it, which is depicted by the red and yellow regions in the contour plot. This high pressure region asserts a lift force acting upwards on the hull, which affects the sailing attitude of the hull. It therefore reduced the trim and sinkage as seen in the previous section.

We can see from the comparison of the *Cp* plots at low and high speeds that the area of effect of the interceptor changes as the speed increases. For the lowers speeds we can see that the increase in pressure as an effect of the interceptor extends quite far forward of the interceptor blade. This area and distance of effect reduces as the speed of

the hull increases, where at Fr = 0.440, the high pressure region extends only a short distance ahead of the blade. The magnitude of the *Cp* increases with the increase in speed. This can be observed in Figure 4-10, where at the higher speeds, a higher localized *Cp* is present at the base of the blade. This is represented by the bright yellow regions ahead of the blade at the higher speeds.

A side by side contour comparison of barehull and interceptor pressure coefficients for a low (Fr = 0.249) and high (Fr = 0.392) speed is given below.

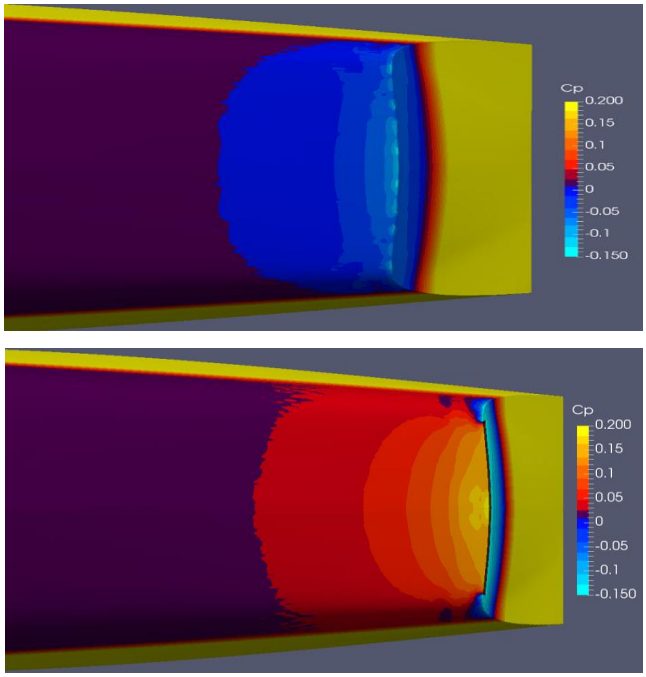

Figure 4-11: Pressure coefficient at Fr = 0.249, for barehull (top) and interceptor (bottom)

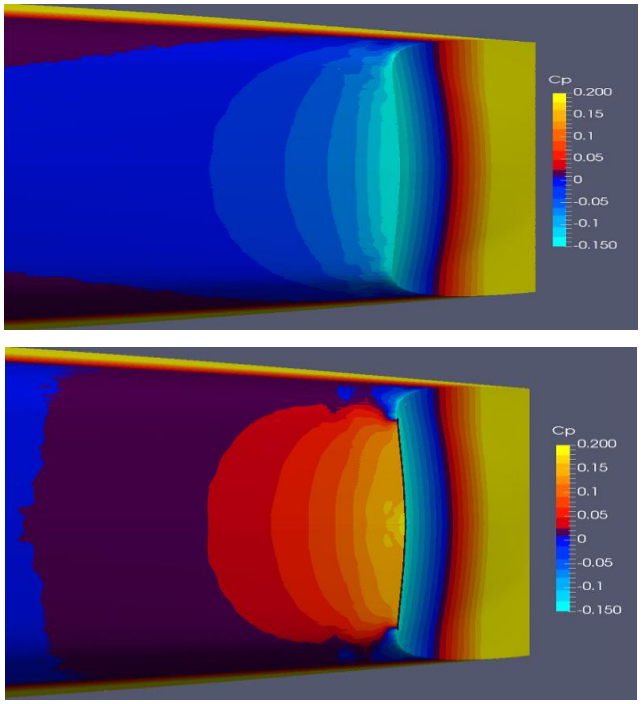

Figure 4-12: Pressure coefficient at Fr = 0.392, for barehull (top) and interceptor (bottom)

To further observe the difference in the pressure coefficient, a graph is plotted for *Cp* along the length of the hull at a distance of 0.0125 m away from the midline of the hull. The blue lines are for the barehull cases while the red lines are for the interceptor cases. The position on the hull is non-dimensionalized dividing it by the length of the hull using x/L. The x/L has a range of -0.5 to 0.5, where a positive value indicates the length of the hull ahead of midship, while a negative value is for the aft of the hull towards the stern. The *Cp* is plotted at different speeds, and we can observe the effect of the interceptors to the left of the plots, where there is spike in the *Cp* compared to the barehull cases.

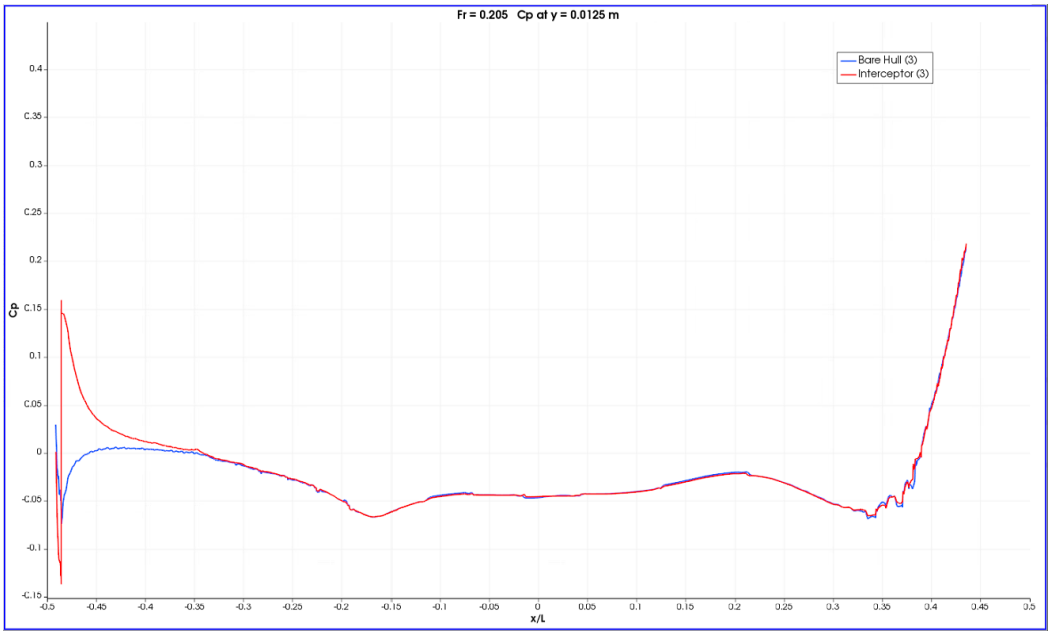

(a) Fr = 0.205

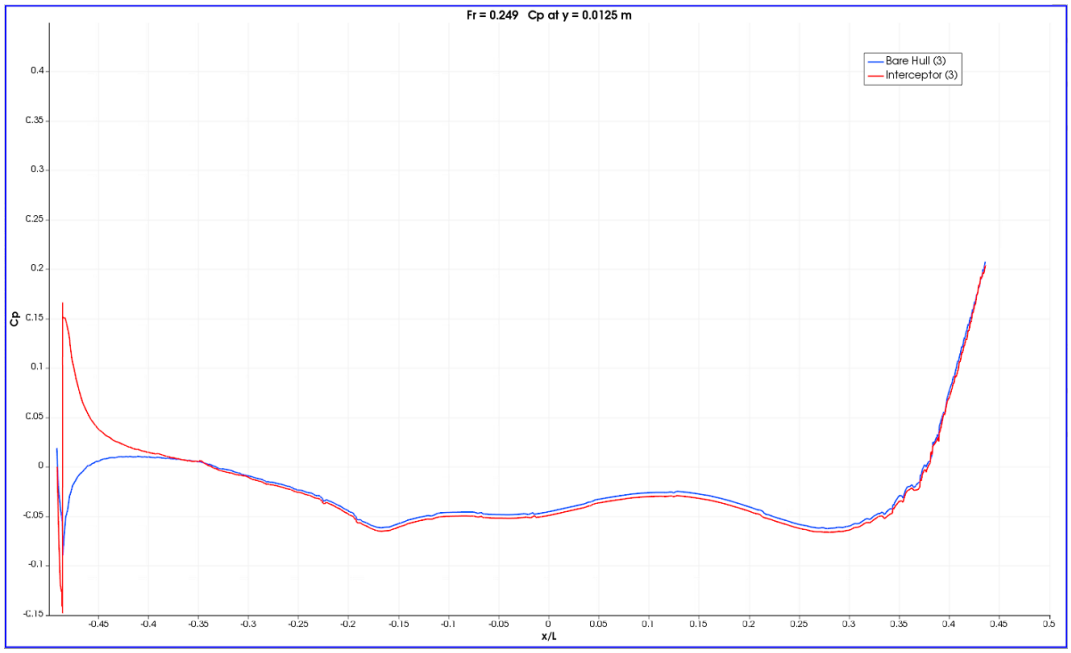

(b) Fr = 0.249

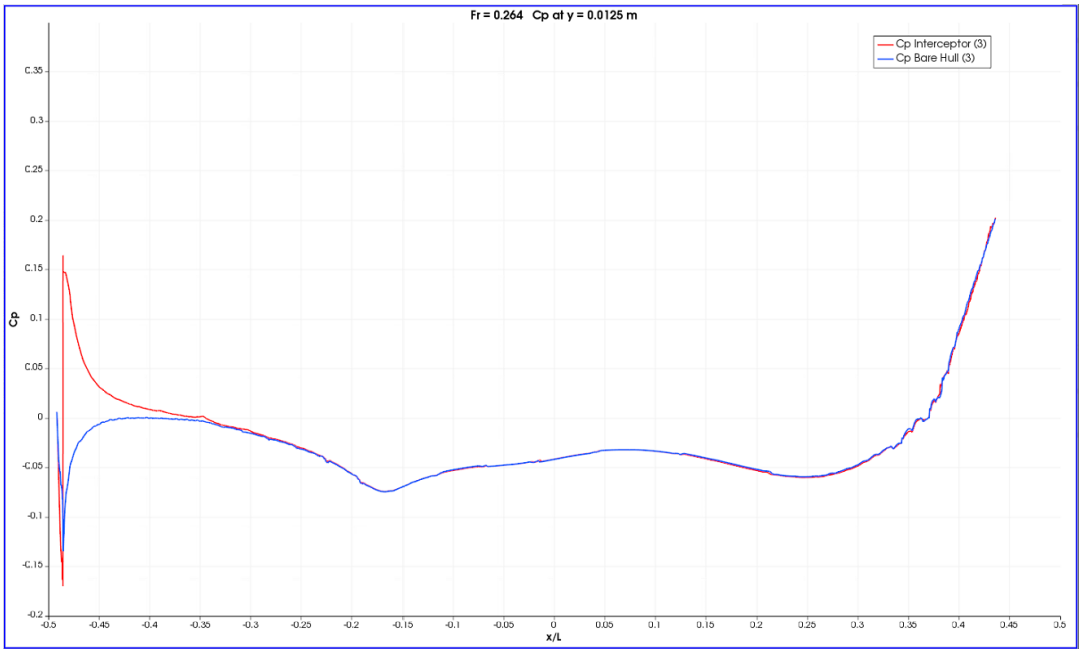

(c) Fr = 0.264

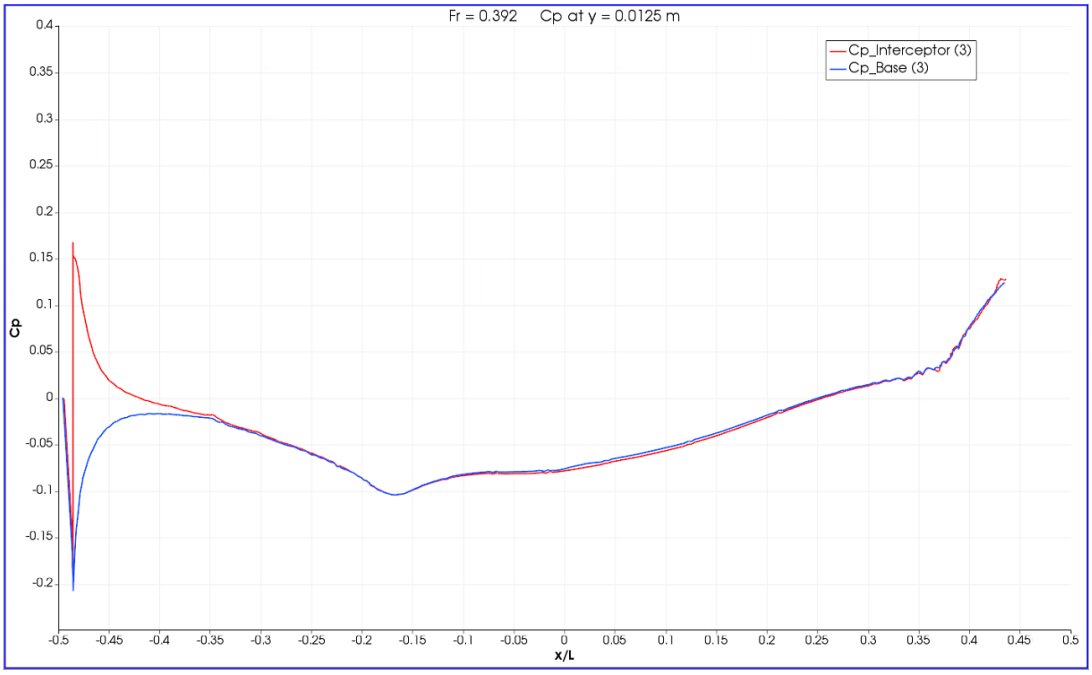

(d) Fr = 0.392

Figure 4-13: Pressure coefficient vs x/L at y = 0.0125 m away from the midline

4.5 Free surface wave

The contour for the free surface wave height is visualized in ParaView, and the contour is compared to the barehull contours to observe the effect of the interceptor.

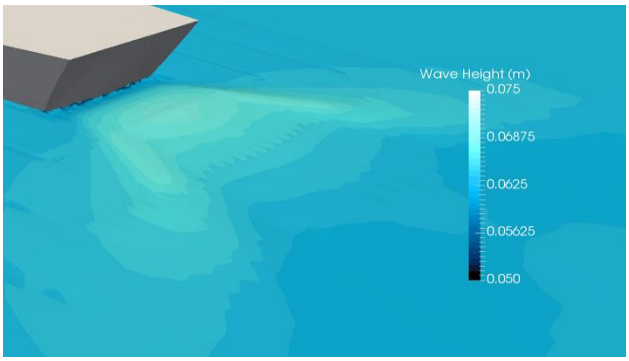

(a) Fr = 0.205 barehull

(b) Fr = 0.205 interceptor

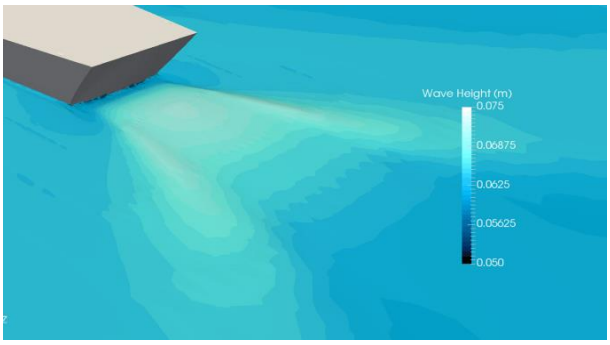

(c) Fr = 0.249 barehull

(d) Fr = 0.249 interceptor

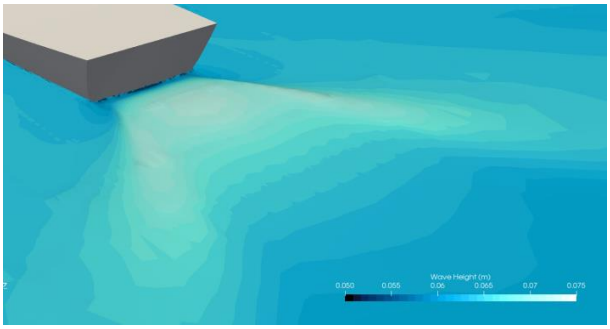

(e) Fr = 0.264 barehull

(f) Fr = 0.264 interceptor

(g) Fr = 0.392 barehull

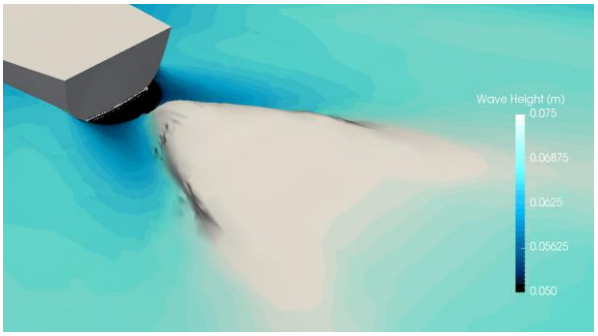

(h) Fr = 0.392 interceptor

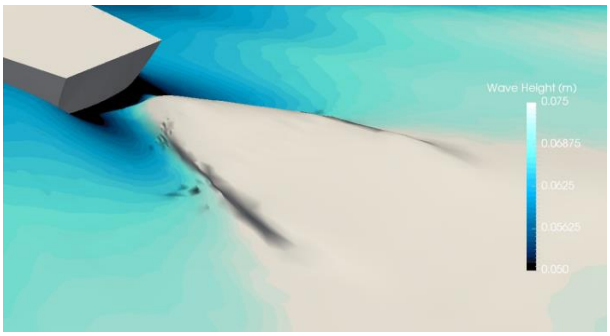

(i) Fr = 0.440 barehull

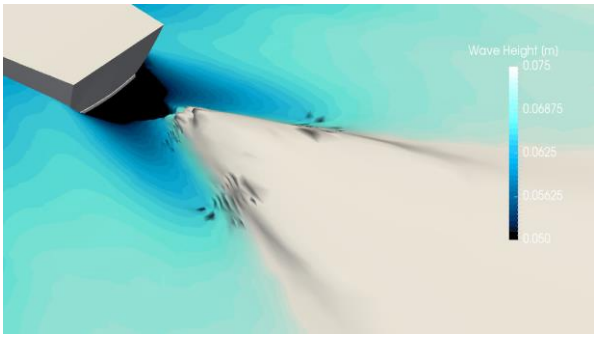

(j) Fr = 0.440 interceptor

Figure 4-14: Free surface wave height comparison between barehull (left) and interceptor (right)

From the comparison of the free surface wave between the barehull and interceptor cases, we can observe a hollow area after the interceptor where the flow separates from the transom. This is depicted by the dark blue/black regions after the transom in the interceptor images (to the right). This hollow area effectively increases the waterline length of the hull, which improves the performance of the interceptor in terms of resistance reduction. At higher speeds we observe that in the interceptor cases, the wave after the stern forms a rooster tail shape. As per Ghadimi et al. (2016), the formation of the rooster tail indicates a reduction in the wave resistance, which is what is observed when comparing the resistance of the interceptor to the barehull cases.

4.6 Wave pattern

The contour for the free surface wave height is visualized in ParaView, and the wave pattern for the interceptor cases across the speeds is compared to the barehull contours to observe the effect of the interceptor.

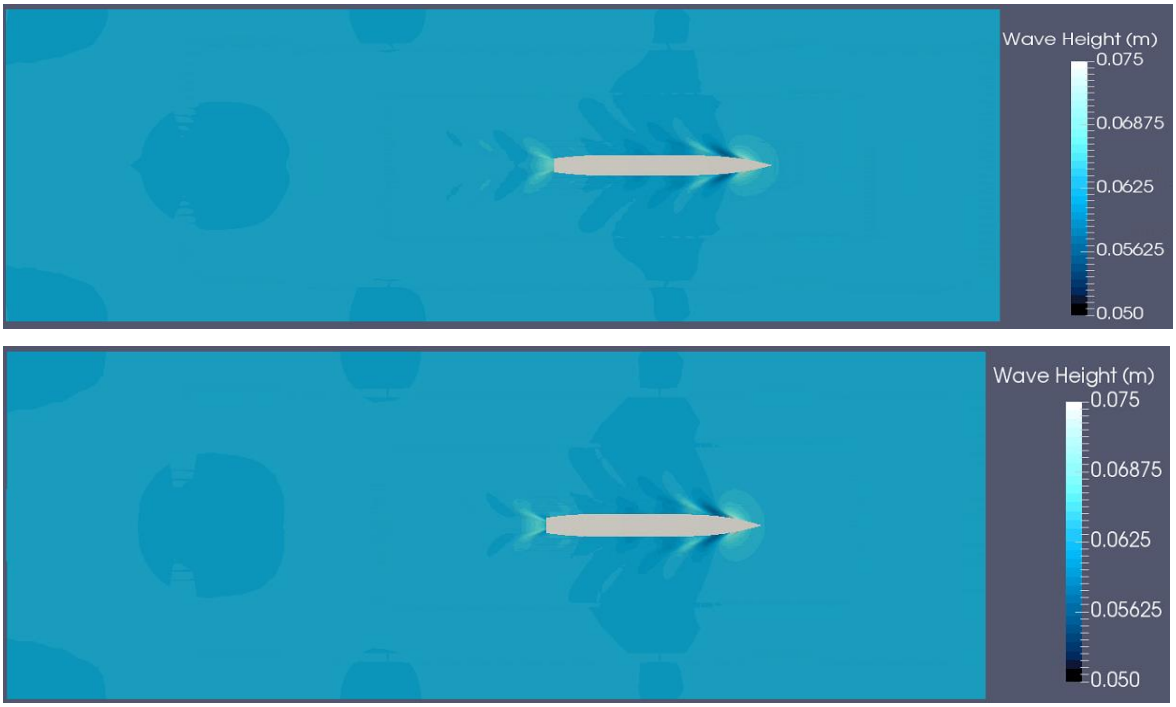

(a) Wave pattern at Fr = 0.205 for barehull (top) and interceptor (bottom)

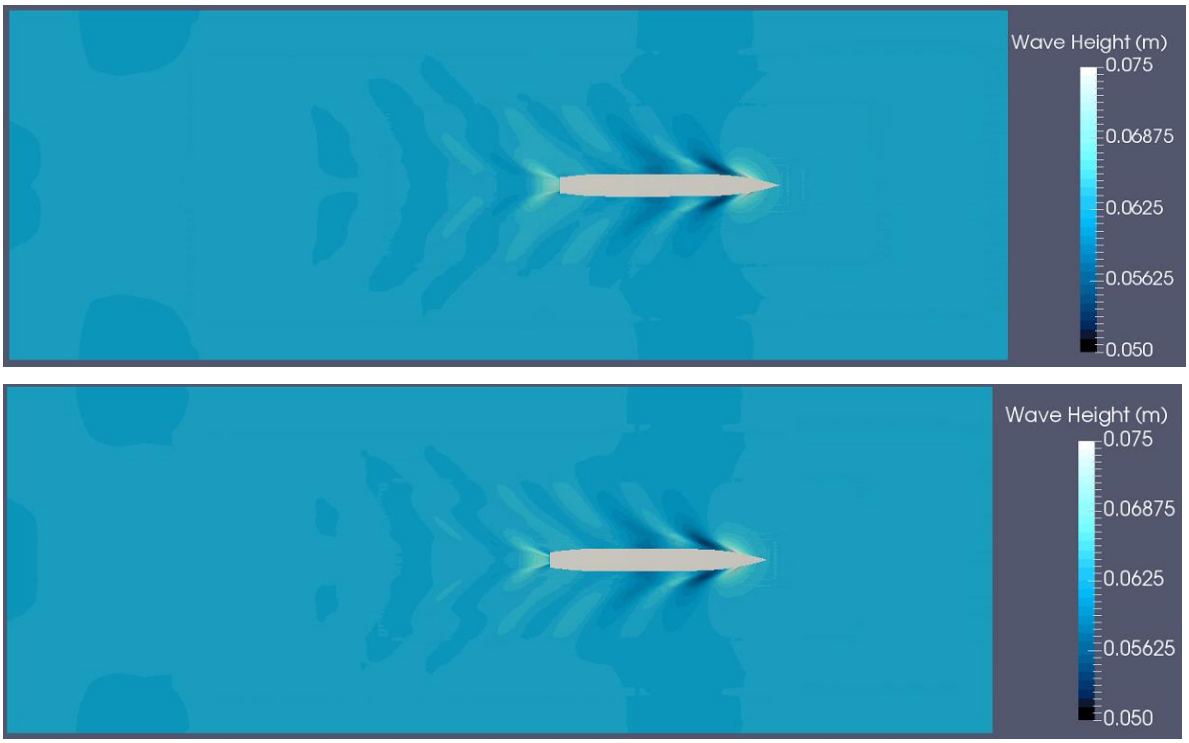

(b) Wave pattern at Fr = 0.249 for barehull (top) and interceptor (bottom)

(c) Wave pattern at Fr = 0.264 for barehull (top) and interceptor (bottom)

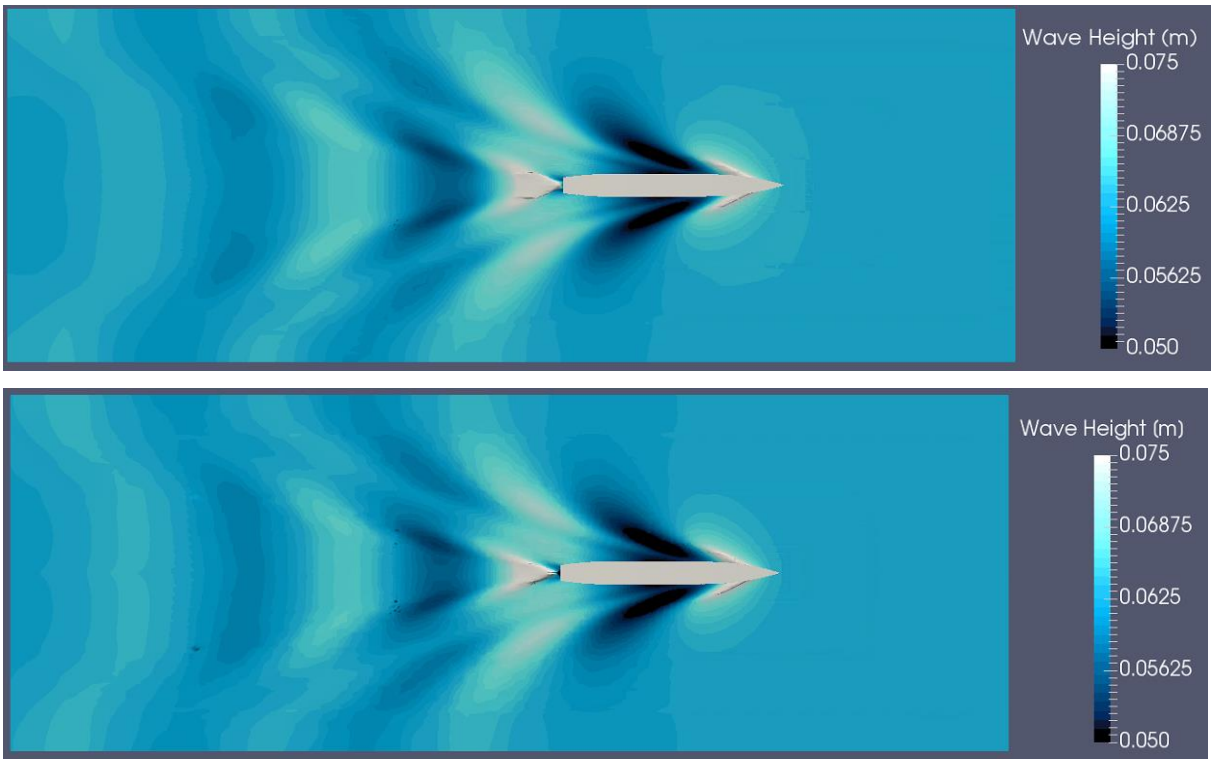

(d) Wave pattern at Fr = 0.392 for barehull (top) and interceptor (bottom)

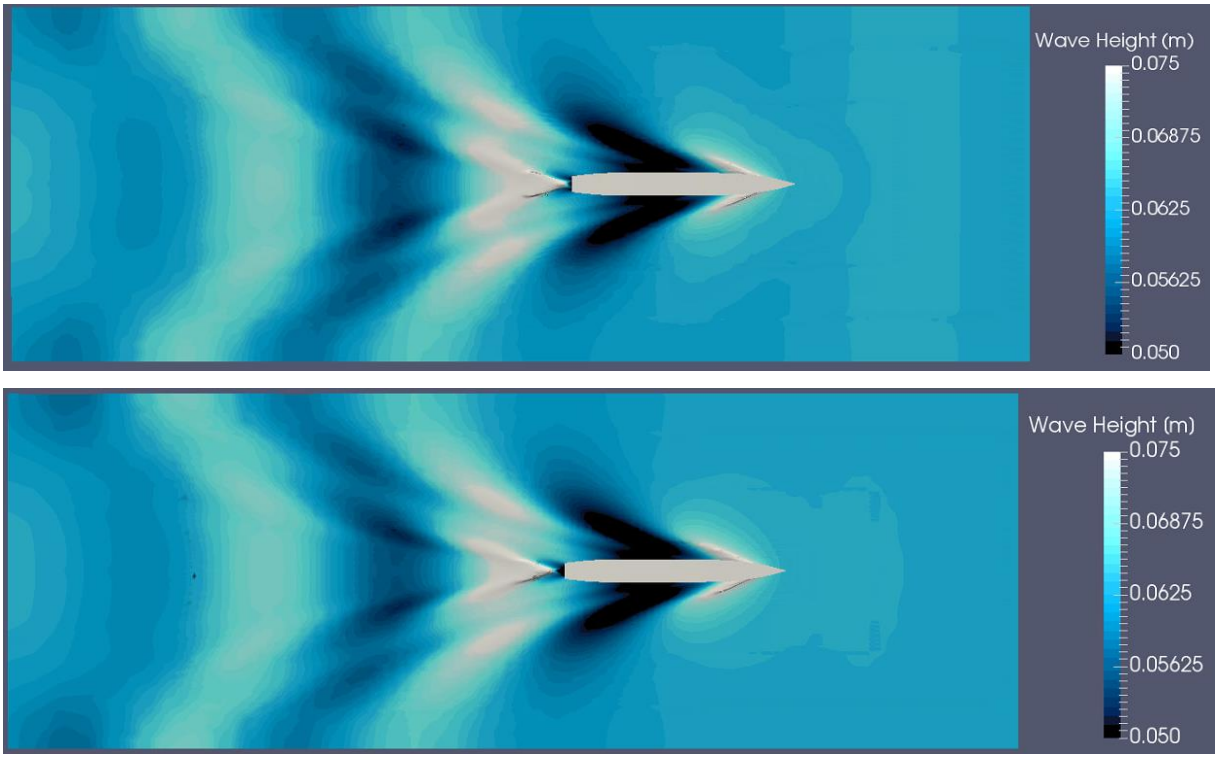

(e) Wave pattern at Fr = 0.440 for barehull (top) and interceptor (bottom)

Figure 4-15: Wave pattern comparison between barehull and interceptor

The wave pattern contours in Figure 4-14 plot the wave height across the computational domain. The dark blue shades depict a height below the draft level (0.06278 m), and the contour colour gets lighter as there is an increase in the wave height. Therefore the white shaded regions in the contour depict the highest wave heights.

Comparing the wave pattern contours for the barehull and interceptor cases, we can observe that the interceptor cases have less white and light blue shades which indicates that the wave heights with the interceptors is lesser than the barehull cases. This could be a result of the reduced trim and sinkage of the hull due to the interceptor, and suggests a reduction in the wave making resistance of the hull.

4.7 Interceptor Comparison

Since this study is aimed to design a stern interceptor with optimal efficiency not only at top speed but also cruising/transfer speeds, different sizes of the interceptor were tested by varying the height and span of the interceptors. Three different interceptors were tested for this study which are listed in Table 4-1. Starting from the interceptor tested in the previous section, the two other interceptors were setup to have two-thirds the height with the same span, and the other had two-thirds the span with the same height. Due to the constraint of the high computational costs and computational time of these cases, it was not possible to test all four interceptors at all speeds. Therefore a low speed (Fr = 0.249) and a high speed (Fr = 0.392) case are run for the four interceptors, and a comparison is made to identify which interceptor provides better performance at the respective speeds.

Table 4-2: Dimensions of the Interceptors

Interceptor No.	Type	Height (m)	Span (m)
1	Large Height, Large Span (LH LS)	0.00375	0.07747
2	Large Height, Small Span (LH SS)	0.00375	0.05164
3	Small Height, Large Span (SH LS)	0.0025	0.07747

The resistance coefficients of the different interceptors are plotted with the barehull resistance coefficients below.

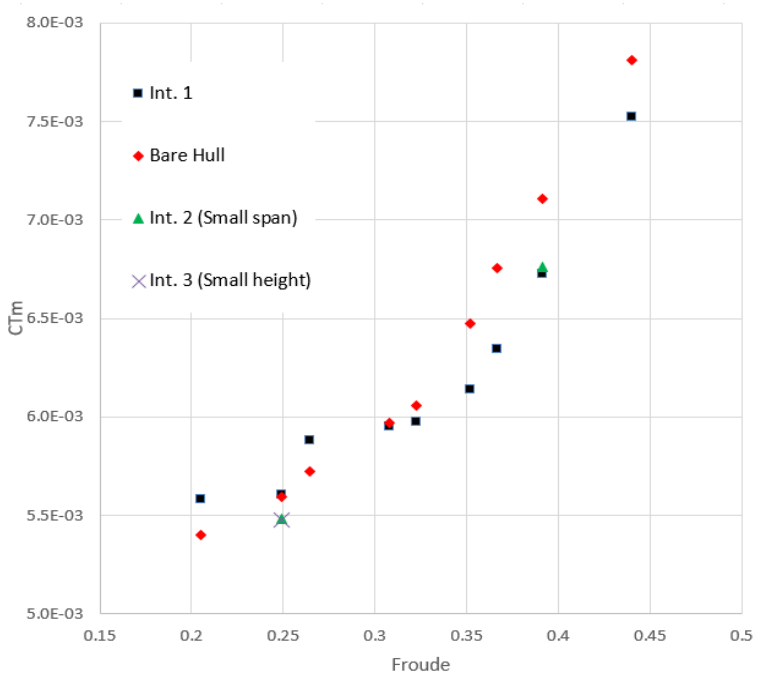

Figure 4-16: Total resistance coefficient comparison of different interceptors

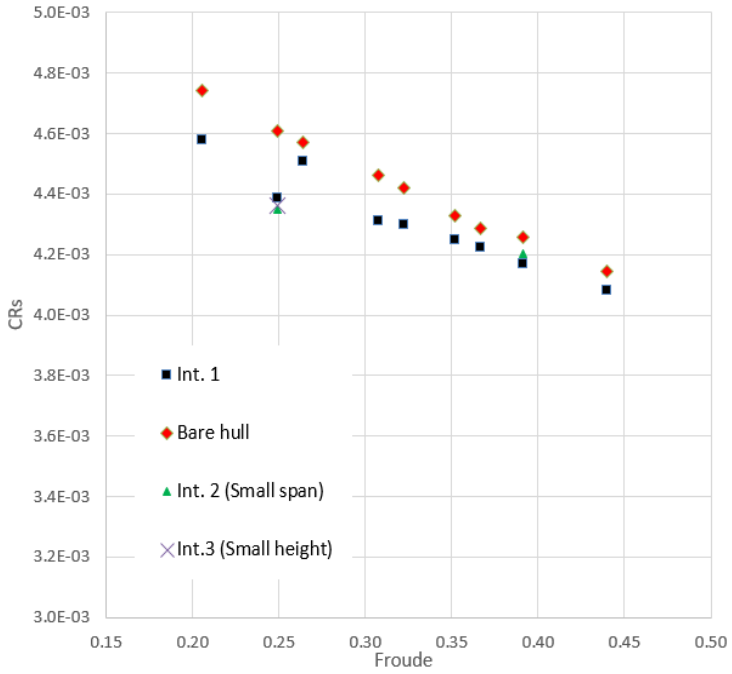

Figure 4-17: Shear resistance coefficient comparison of different interceptors

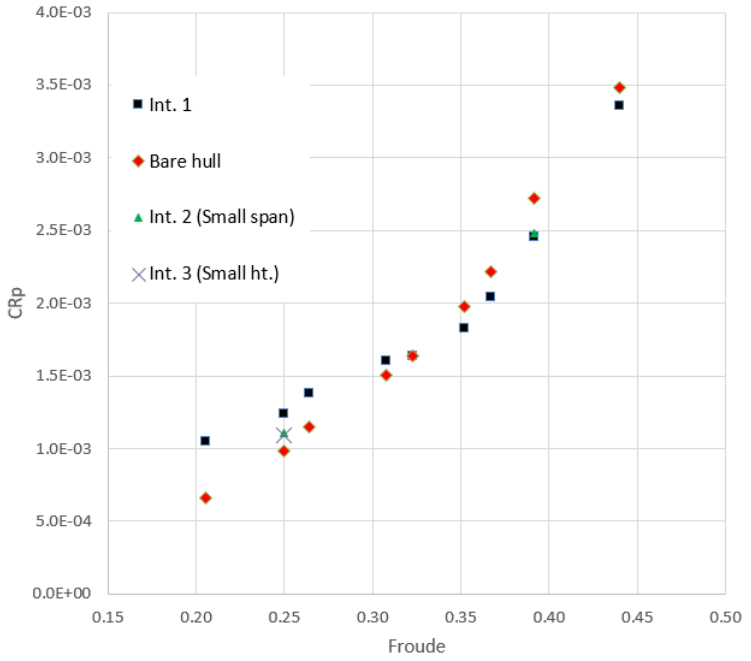

Figure 4-18: Pressure resistance coefficient comparison of different interceptors

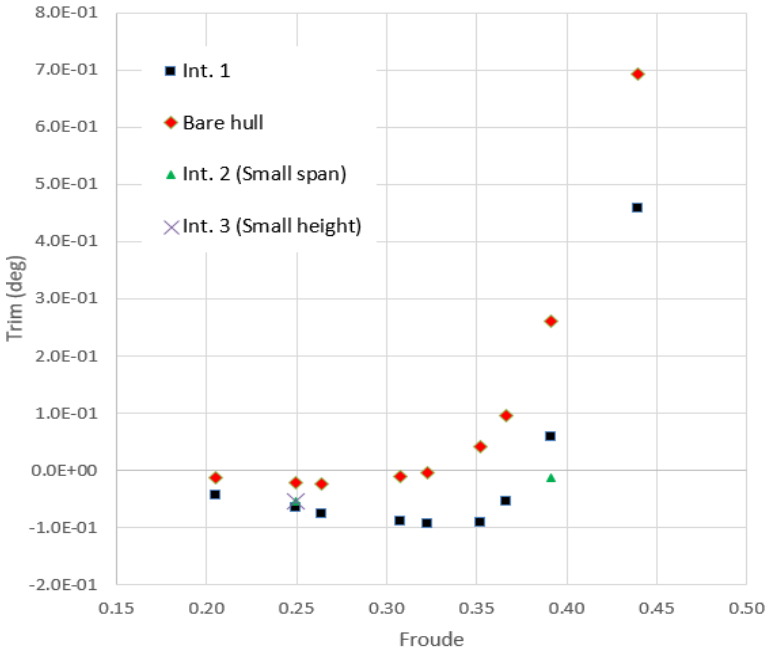

Figure 4-19: Trim comparison of different interceptors

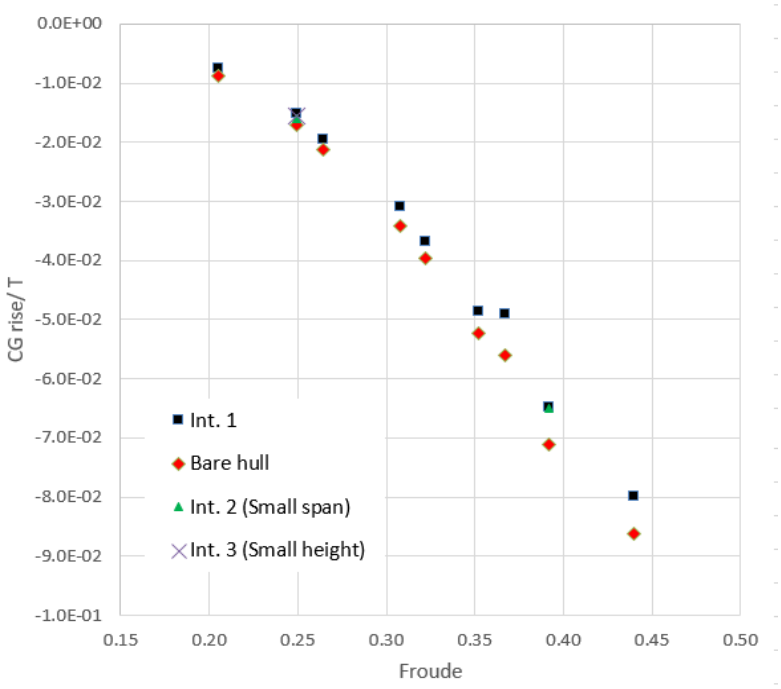

Figure 4-20: CG rise/T comparison of different interceptors

From the resistance comparison plots, we can observe that at the low speed (Fr = 0.249), the smaller span and height interceptors (Int. 2 and 3) provides better performance with lesser resistance in comparison to the large interceptor (Int. 1), as well as the barehull. At higher speeds, both Int. 1 and 2 reduce the resistance compared to the barehull, but Int. 1 provides the best resistance.

For the large interceptor (Int. 1) at low speeds, the added drag component due to the interceptor will be greater than the reduction due to the improvement in the trim and sinkage. As a result an increase in the resistance is observed for the lower speeds. For the smaller interceptors (Int. 2 and 3), the added drag is lesser and the reduction in resistance due to improved trim and sinkage results in an overall improvement in resistance performance. At high speeds, the reduction in resistance due to the reduced trim and sinkage for the large interceptor will be much greater than the added drag, as a result of which we observe much better performance with Int. 1.

From these simulations, we observe very promising results in terms of energy savings while using interceptors. A reduction in resistance is observed at both high and low speeds (Int. 2 and 3), which indicates that by adjusting the interceptor blades

depending on the speed, we can achieve optimal efficiency at both low and high speeds. Further simulations need to be conducted for Int. 2 and 3 for the intermediate speeds so as to identify which interceptor geometry provides the best performance at different points along the speed range.

CHAPTER 5

EXPERIMENTAL SETUP

Calm water experimental tests are conducted at the towing tank facility at Virginia Tech. The model used for the tests is the same FFG-7 model used at the NAHL as given in Section 2.1. The aim of these tests is to verify the results obtained in OpenFOAM, as well as to study the improvement observed by the use of the interceptors in the experimental model. This chapter will discuss the experimental setup used for the models tests, the instrumentation used for the measurement of data, as well as signal acquisition and signal processing of the data. Data was measured for the resistance, trim and sinkage of the model, for a speed range of Froude number 0.205 to 0.405.

5.1 Towing tank facility

The Virginia Tech towing tank basin has a width of 6 feet and a maximum water depth of 4 feet. The overall length of the basin is 98 feet, but the first 4 feet and the last 24 feet are used for braking the carriage. The usable test length of the basin is approximately 70 feet. The tank is fitted with a beach at one end for absorbing wave energy, and a wavemaker at the other end. The wavemaker is not utilized for this study, since only calm water resistance tests are conducted. There are two glass walled observation pits along the side of the tank, one located approximately in the middle of the test region and the other pit located at the starting end.

The carriage and rails were designed and constructed by the firm of Kempf and Remmers of Hamburg, Germany and were shipped in sub-assemblies to Virginia Tech. The allowable tolerance on rail height was ±0.1mm. Wedges were used to give final straight alignment of each rail. The allowable tolerance on alignment was ±0.2mm. Final alignment was done optically. After final adjustments in height were made, the space between the bearing plates and the bottom of the rail was filled with concrete.

The tank is fitted with a carriage that is driven by a 400 V DC motor through a gear reduction box. The DC power is supplied from a 220 V AC motor-generator set. A maximum speed of 3.0 meters per second at 3000 RPM can be obtained. The carriage braking is done automatically using trips installed at both ends. The brake is of the magnetic clutch type and brakes the DC motor directly. The brake is applied if power to the carriage is interrupted. Braking deceleration is 0.7 meter per second per second.

Figure 5-1: Virginia Tech towing tank facility

Figure 5-2: Towing Carriage

5.2 Instrumentation

A towing rig was assembled, instrumented and calibrated for the carriage in order to measure the resistance, trim and sinkage of the model. The model is fit with a pitch pivot that is attached to a heave post on the rig. Since we are interested in studying the trim and sinkage, the model is free to heave and pitch, while the motion is fixed in other directions.

The resistance of the model is measured with a 5 lb. variable reluctance block gauge that is fixed at the LCB. The block gauge is connected to the pitch pivot attached to the model. The trim is measured by using a pair of lasers attached to the towing rig. The lasers are used to calculate the distance of the model away from the towing rig at 2 separate locations. This data is then used to calculate the pitch angle. The sinkage of the model is measured using a string potentiometer attached to the towing rig. Schematics and the pictures of the towing rig are shown in Figure 4-3 to Figure 4-5.

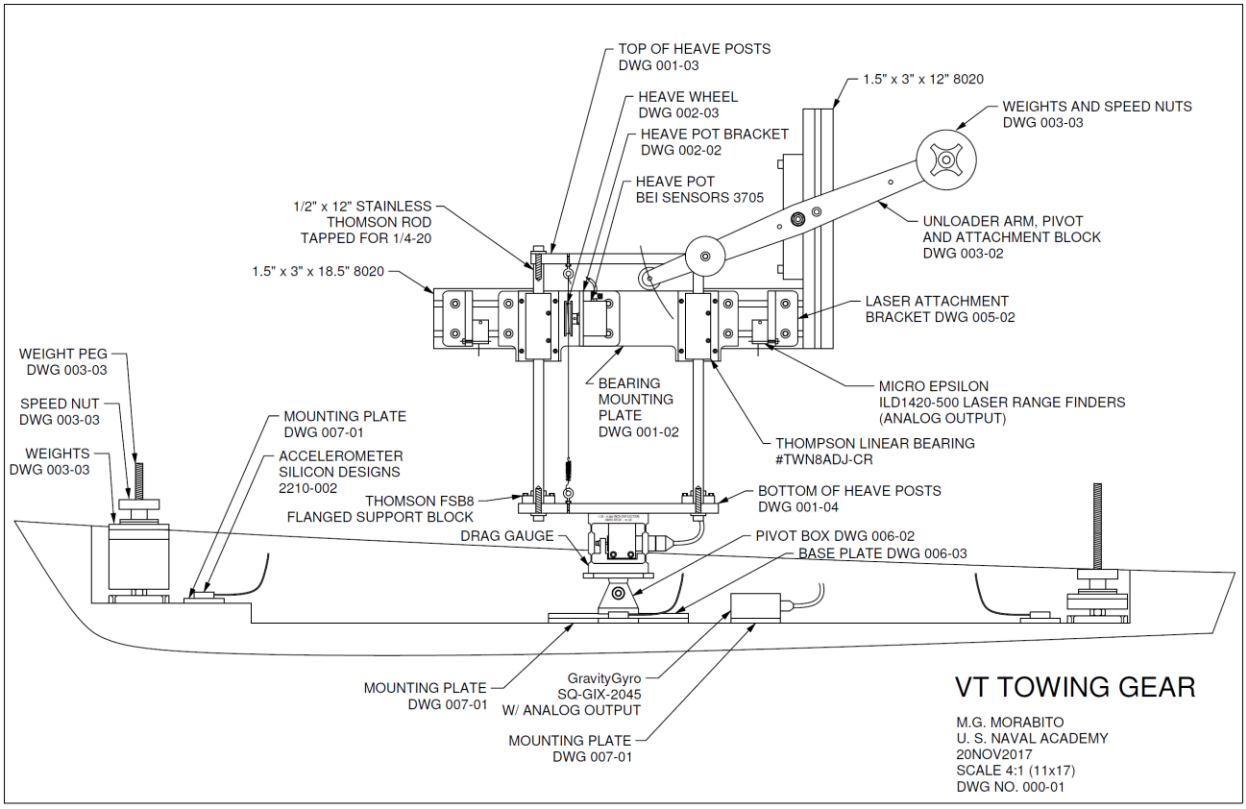

Figure 5-3: Schematics of the towing rig (courtesy of Dr. Morabito from the USNA)

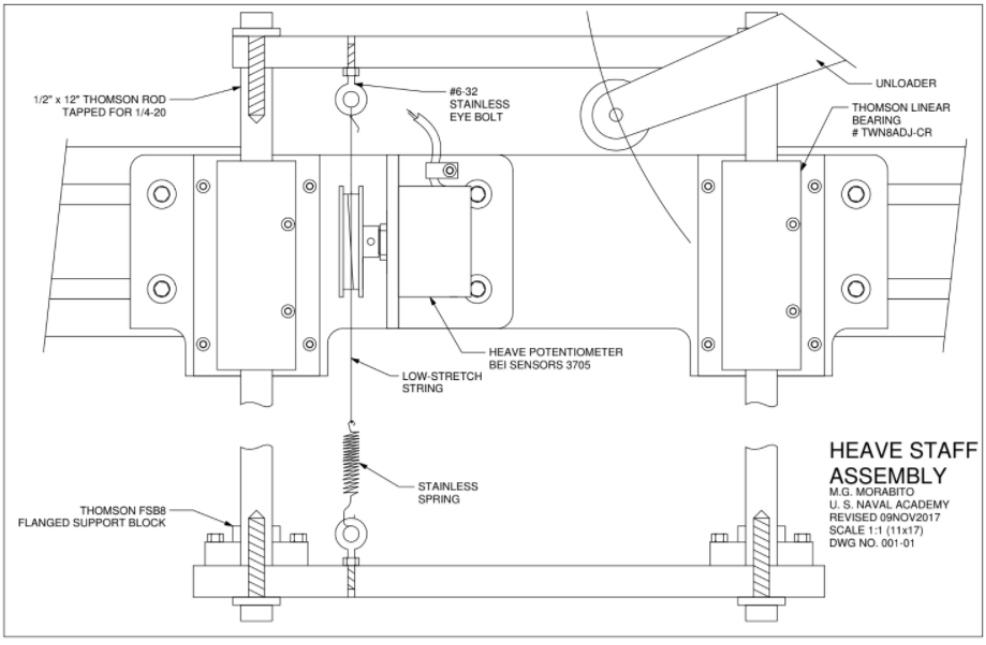

(a)

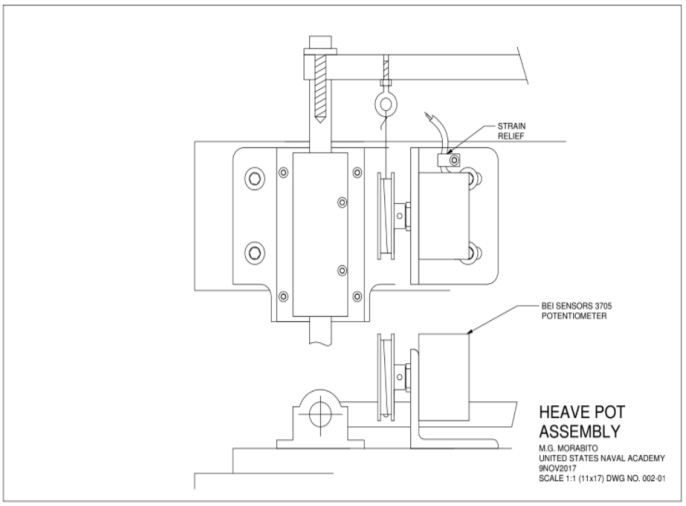

(j)

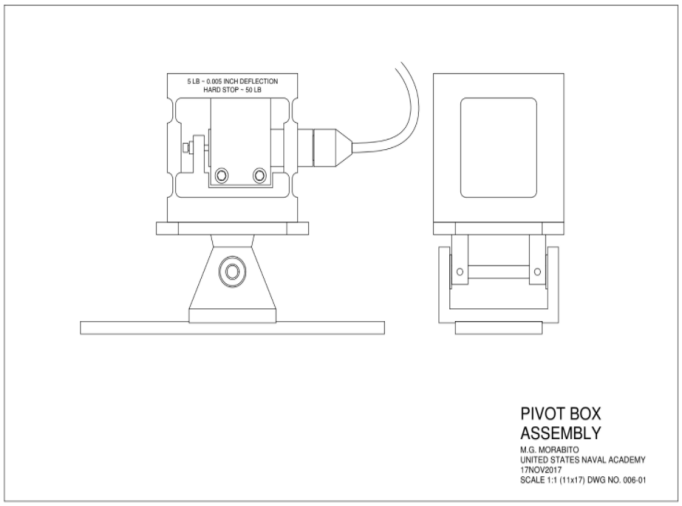

(c)

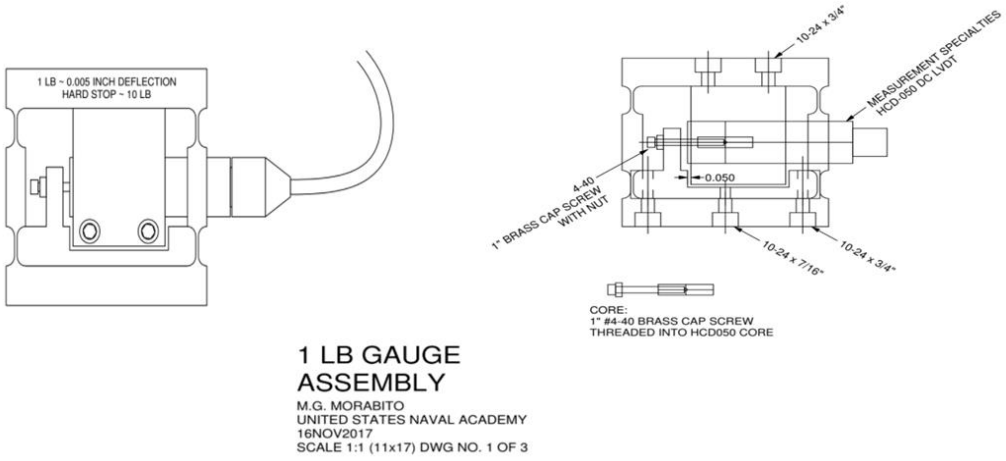

(d)

Figure 5-4: Schematics of the towing rig components (courtesy of Dr. Morabito from the USNA)

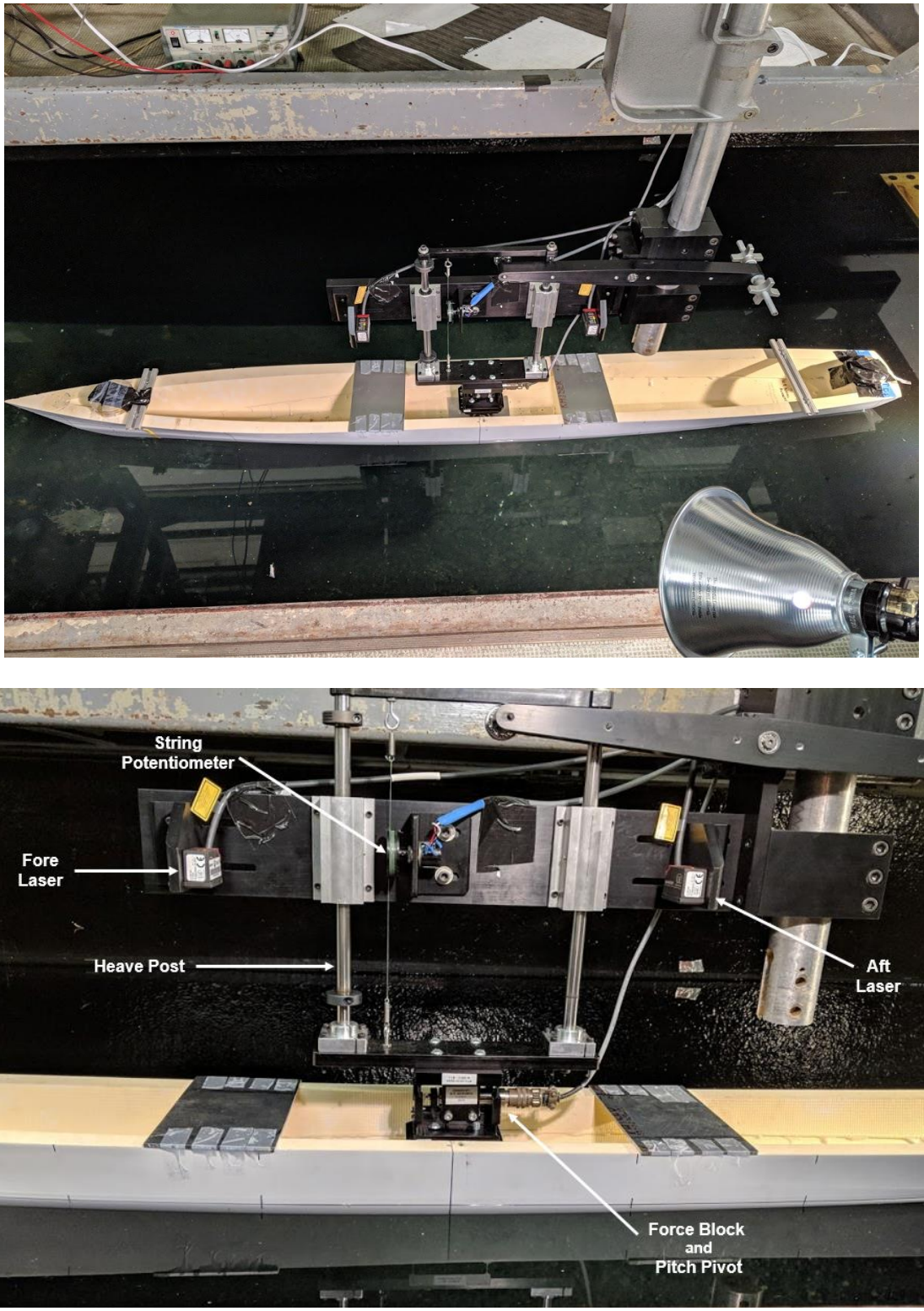

Figure 5-5: Towing rig

5.3 Signal Acquisition and Processing

The sensors on the hull are connected to a data acquisition box which transmits the data from the sensors to a laptop on the towing carriage. Control signals are sent, and the experimental data is acquired using the software LabVIEW. Each individual sensor was calibrated before the model tests, and calibration constants were determined for each. The data acquired from the sensors were in voltage and were converted to the required form (resistance, pitch and heave), by using the calibration constant. Lasers were used to measure the trim angle, since that would enable the acquisition of data without having any cable connections on the model, which would be observed if we were to use accelerometers or inclinometers instead.

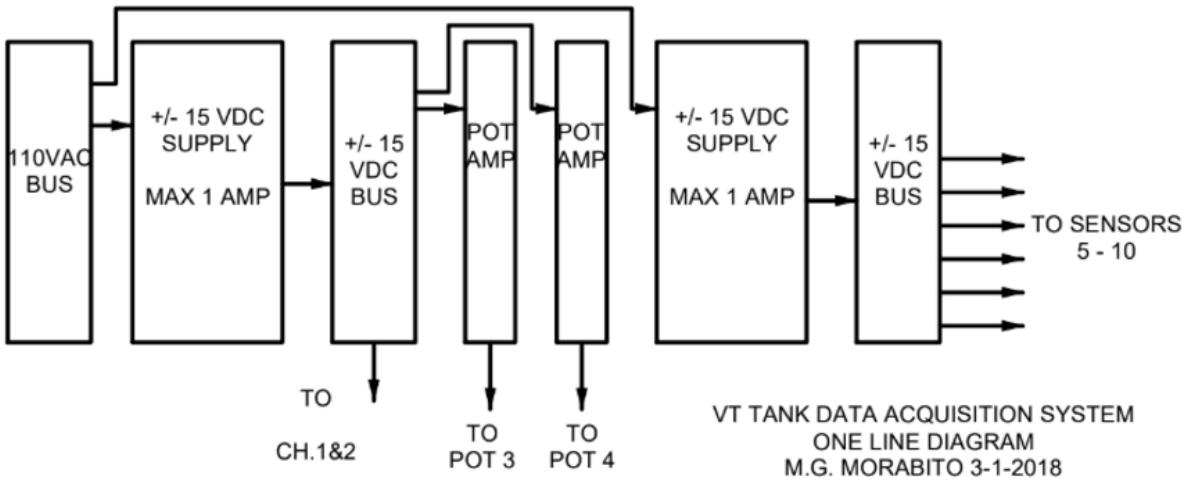

Figure 5-6: Initial drawing for the data acquisition system (courtesy Dr. Morabito from the USNA)

An initial drawing of the data acquisition system is given in Figure 4-6. The sensors on the towing rig are connected to the data acquisition system, which is then connected to a laptop on the towing carriage. The signals are processed using LabVIEW, where the readings of the sensors are plotted over time. A sample of the LabVIEW plots is given in Figure 4-7 and Figure 4-8.

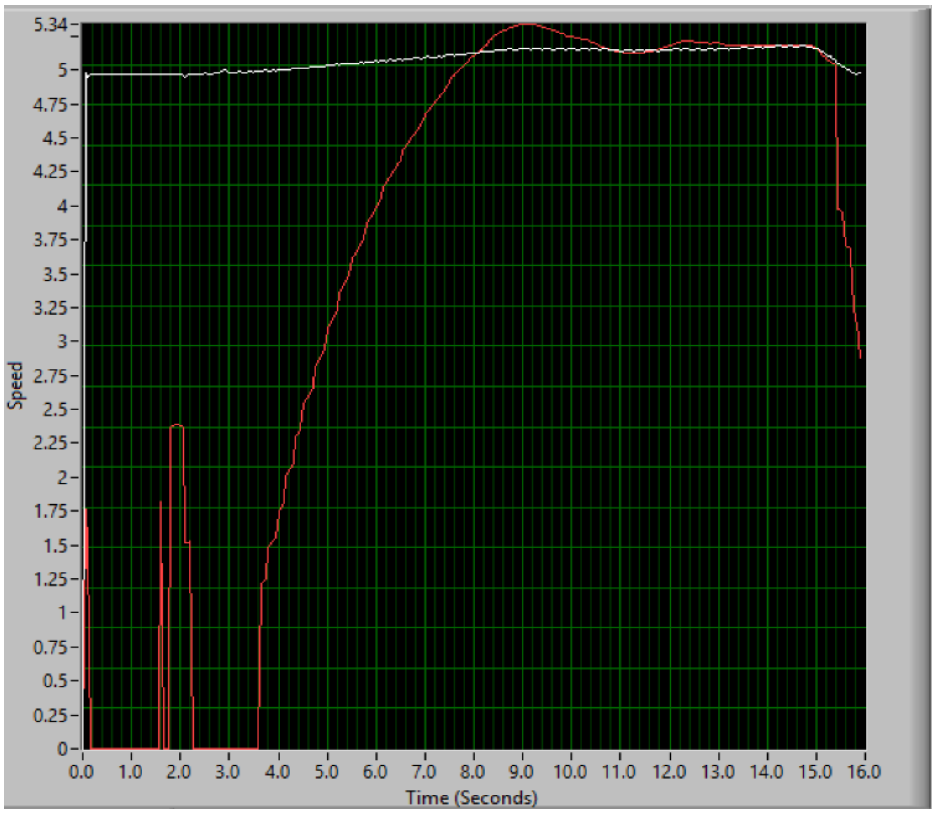

Figure 5-7: LabVIEW speed plot (red line) for Fr = 0.405

In Figure 4-7 we can see the plot of the carriage speed (in ft/s) that is obtained in LabVIEW. The carriage speed (red line in Figure 4-7) is measured by recording a timing pulse produced by a wheel on the carriage that runs along the inner rail. The data acquisition system measures the time between pulses and converts that to a speed. We can observe from the plot, the acceleration of the carriage before it reaches a steady speed. The required data values of the trim, sinkage and resistance are calculated for this duration of the constant speed. The speed of Fr = 0.405 was the highest speed for this facility where we could get a sufficient period of constant speed of at least 1 second, as can be seen in Figure 4-7.

Figure 4-8 shows the plot of the sensor outputs of the potentiometer, load cell and the 2 lasers for a speed of Fr = 0.405. The plotted values are the voltage outputs of the sensors, which are then converted to the relevant format using the calibration constant of the sensors. The same time duration where a constant speed is observed from Figure 4-7 is used to average these values.

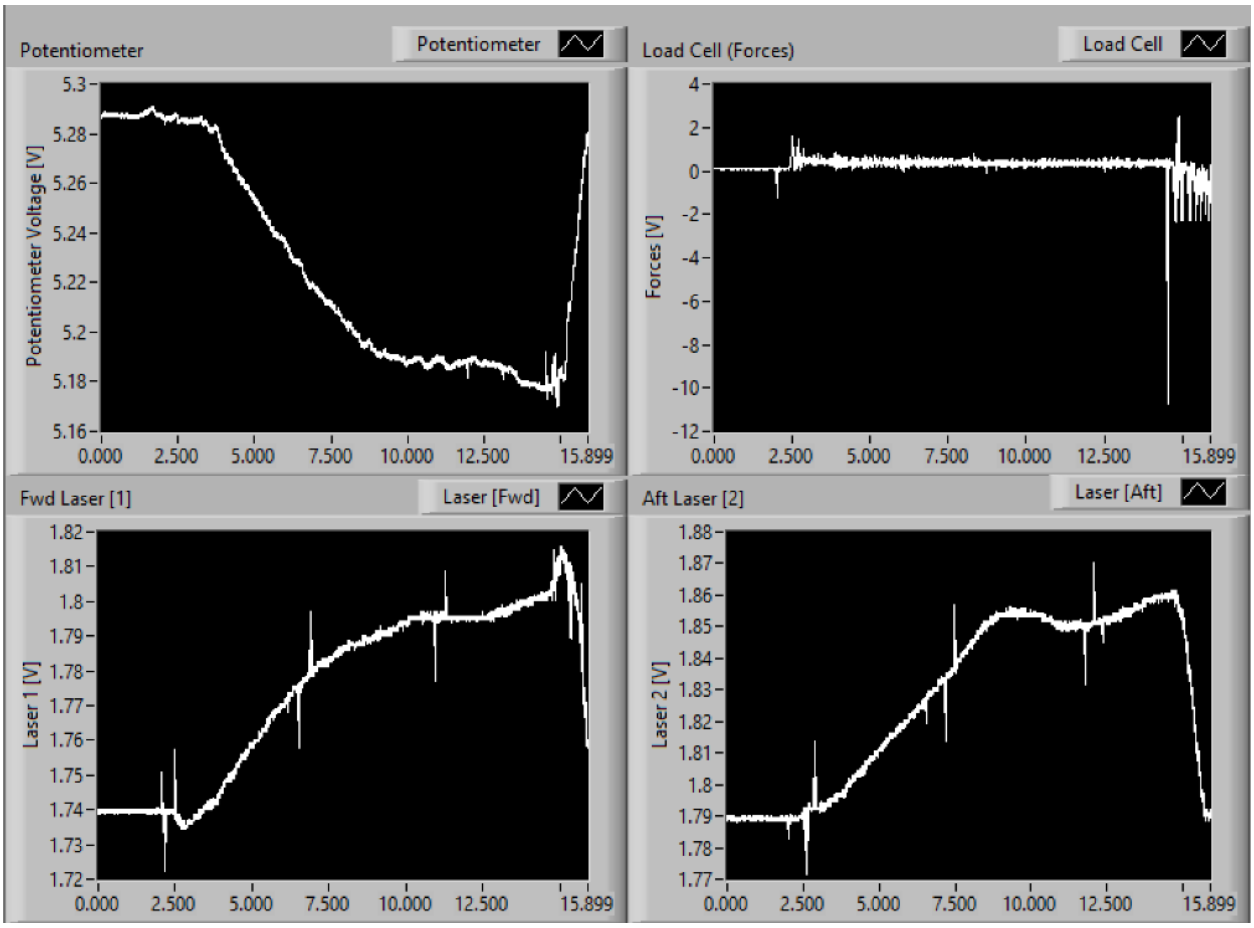

Figure 5-8: LabVIEW sensor plots for Fr = 0.405

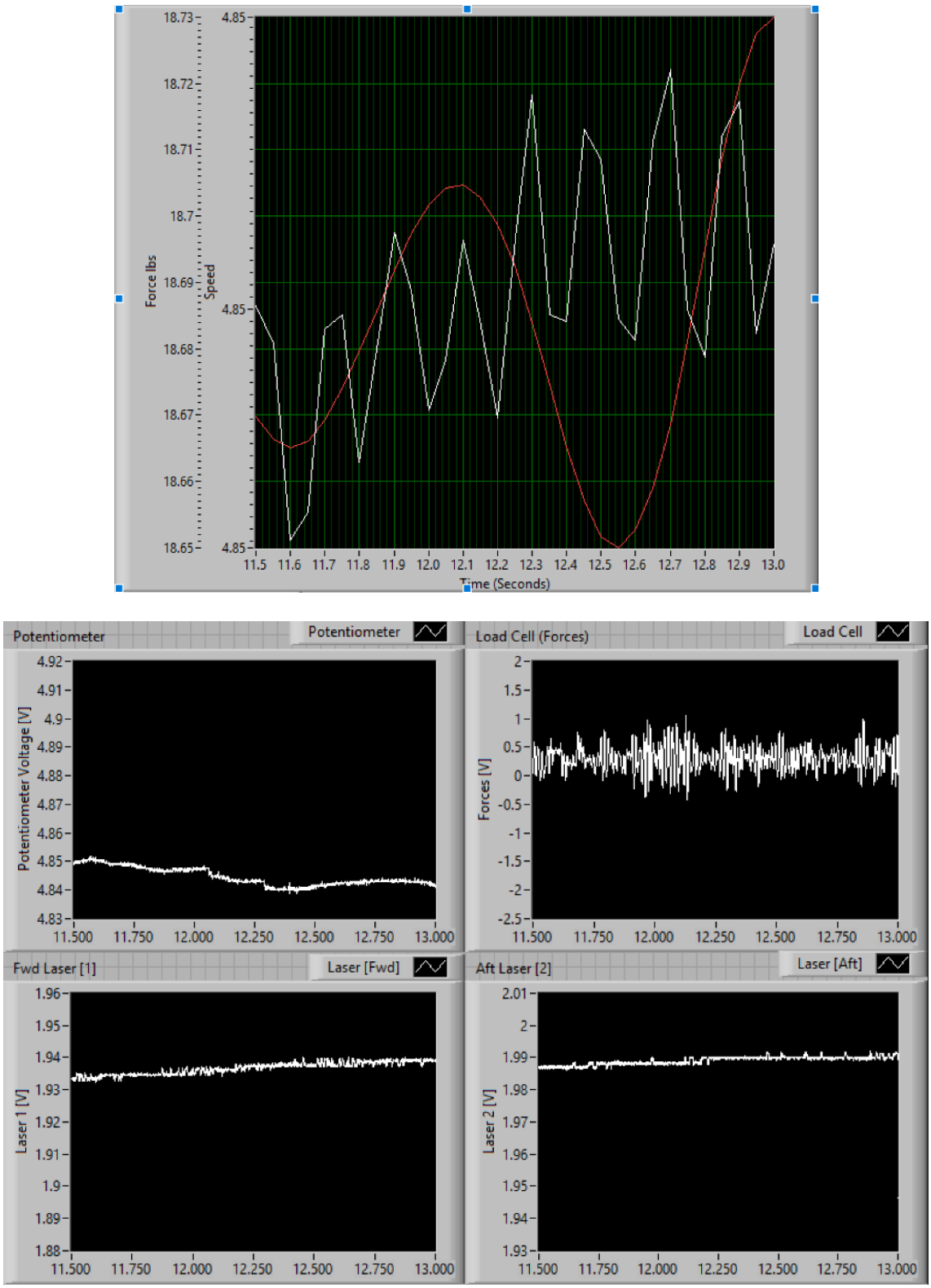

Figure 5-9: LabVIEW speed (top) and sensor (bottom) plot results for constant speed duration

5.4 Stimulating turbulence

The flow around the full scale FFG-7 ship for the speeds tested in this study will be turbulent, and therefore the conditions for the model tests have to be simulated to match that of the full scale. There are various turbulence stimulators that can be utilized to achieve a turbulent flow around the model.

For this study, the FFG-7 model has been borrowed from the NAHL where the turbulence stimulation is done using Hama strips. The Hama strips are made from electrical tape, and cut into a triangular shape which causes a vortex loop at the trailing edge thereby tripping the flow and causing the turbulence. A study was conducted at the NAHL to determine the required thickness of the Hama strips [11]. The required thickness of the Hama strips was determined, and 7 Hama strip layers of 0.005 in thickness each are used. This was determined to cause the turbulent flow around the model, while adding the least drag at higher speeds. Figure 4-9 shows a picture of the Hama strips used for the turbulence stimulation in the model tests.

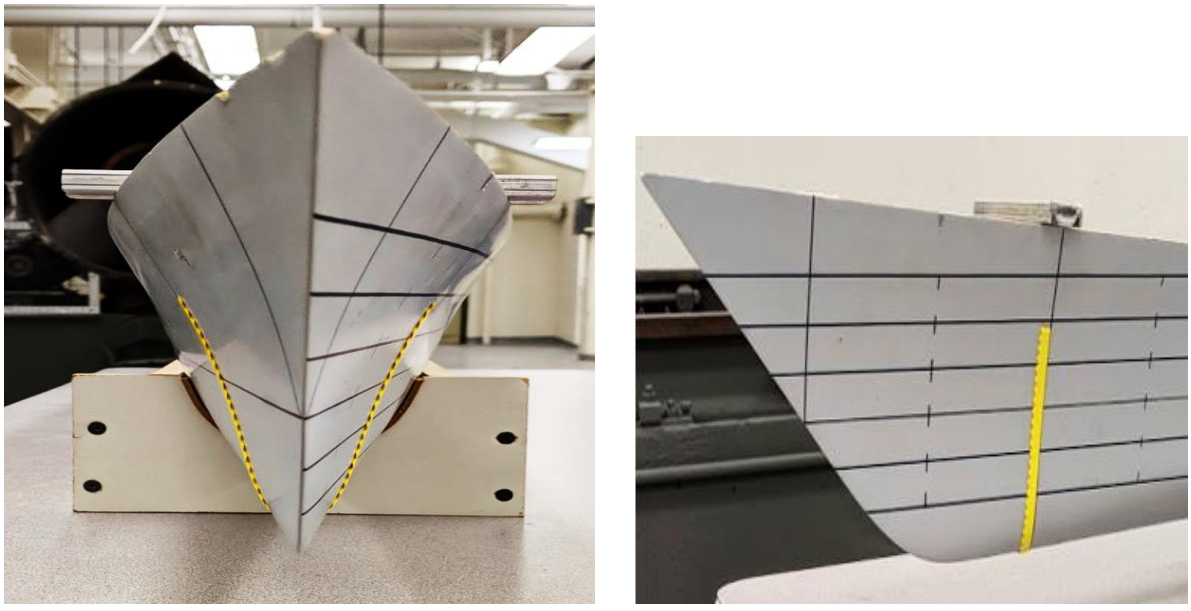

Figure 5-10: Hama strips used on the model

CHAPTER 6

EXPERIMENTAL RESULTS

Calm water experimental tests are conducted for a speed range of Froude number 0.205 to 0.405, so as to be within the speed range simulated in OpenFOAM, while staying within the limits of the facility to attain accurate results. The tests for the barehull model is initially conducted, and the results are verified with the OpenFOAM results as well as the results of the model tests conducted at the NAHL. After verifying the accuracy of the tests, calm water tests for the model with interceptors is conducted. Four different interceptors with varying heights and spans are tested across the speed range to ascertain which interceptor would provide the best results at a particular speed.

6.1 Resistance

The resistance data measured from the model tests is used to calculate the total resistance co-efficient, friction resistance co-efficient and the residuary resistance co-efficient for the model.

The *total resistance co-efficient* (C_{T_m}) of the model is calculated as:

$$C_{T_m} = \frac{R_{T_m}}{0.5 * S * \rho * V^2} \tag{6.1}$$

where, R_{T_m} is the total model resistance, S is the nominal wetted surface area (as defined in Section 3.1.2), ρ is the density of the water in the tank, and V is the velocity of the model.

The *friction resistance co-efficient* (C_{F_m}) for the model is calculated as per the ITTC-57 formula:

$$C_{F_m} = \frac{0.075}{(\log Re_m - 2)^2} \tag{6.2}$$

where, Re_m is the Reynolds number at the particular speed.

The corrections made to the resistance coefficients in Section 3.1.2 are applied here as well. In order to get the residuary resistance, the friction resistance on the model is calculated and then subtracted from the total model resistance. The new wetted surface area (S^N) is calculated using ParaView is used to calculate the *corrected friction resistance* (R_{F_m}) of the model:

$$R_{F_m} = {C_{F_m}}^{ITTC} * 0.5 * S^N * \rho * V^2 \tag{6.3}$$

The *corrected residuary resistance* (R_{R_m}) of the model is:

$$R_{R_m} = R_{T_m} - R_{F_m} \tag{6.4}$$

The *residuary resistance co-efficient* (C_{R_m}) of the model is calculated as:

$$C_{R_m} = \frac{R_{R_m}}{0.5 * S * \rho * V^2} \tag{6.5}$$

6.2 Verifying barehull model data with OpenFOAM

Comparative plots of the resistance co-efficients vs. Froude number are given in Figure 5-1 to 5-3, comparing the barehull model test data to the numerical results from OpenFOAM.

The correction specified in the previous section is used to calculate the residuary resistance and the corrected C_{R_m} is compared to the numerical data in Figure 5-3.

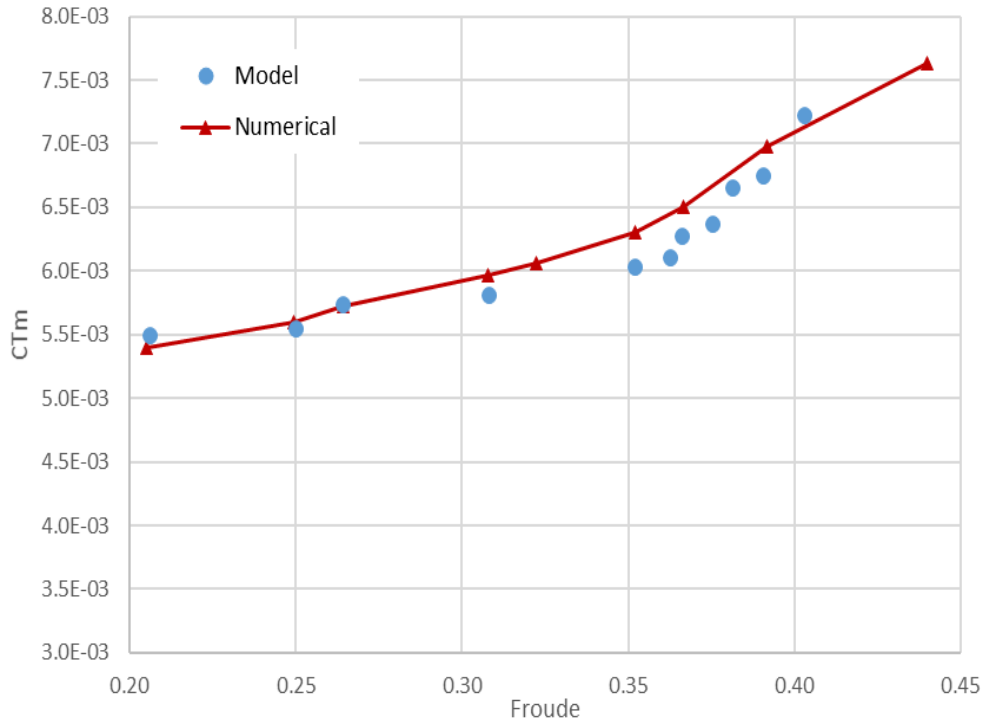

Figure 6-1: Total resistance coefficient vs Froude number

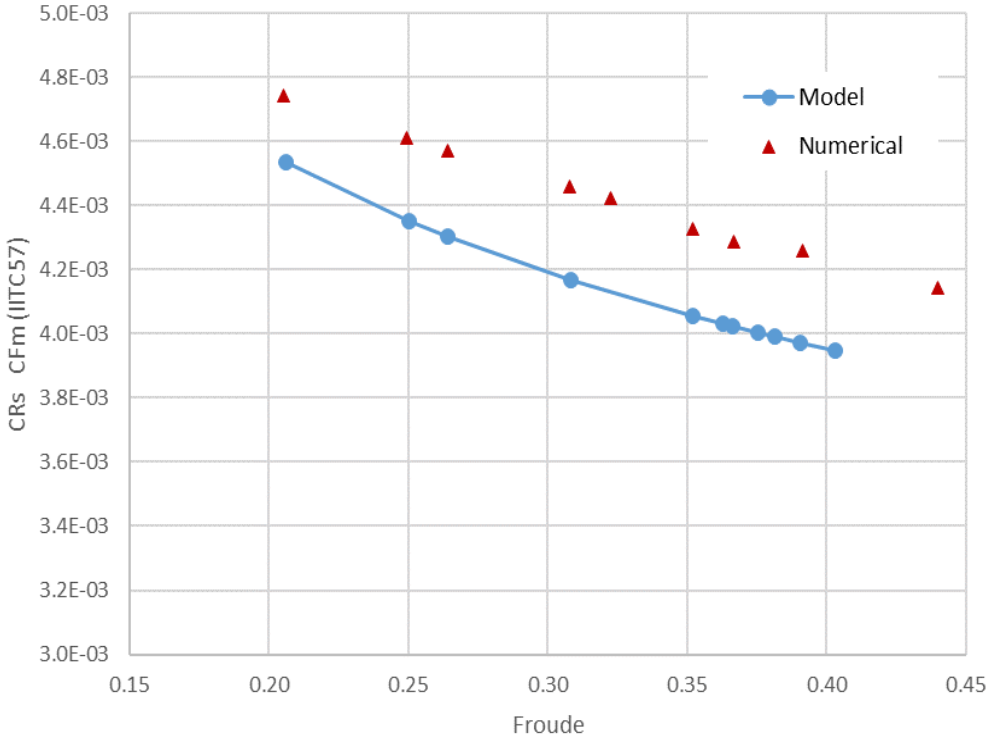

Figure 6-2: Friction resistance coefficient vs Froude number

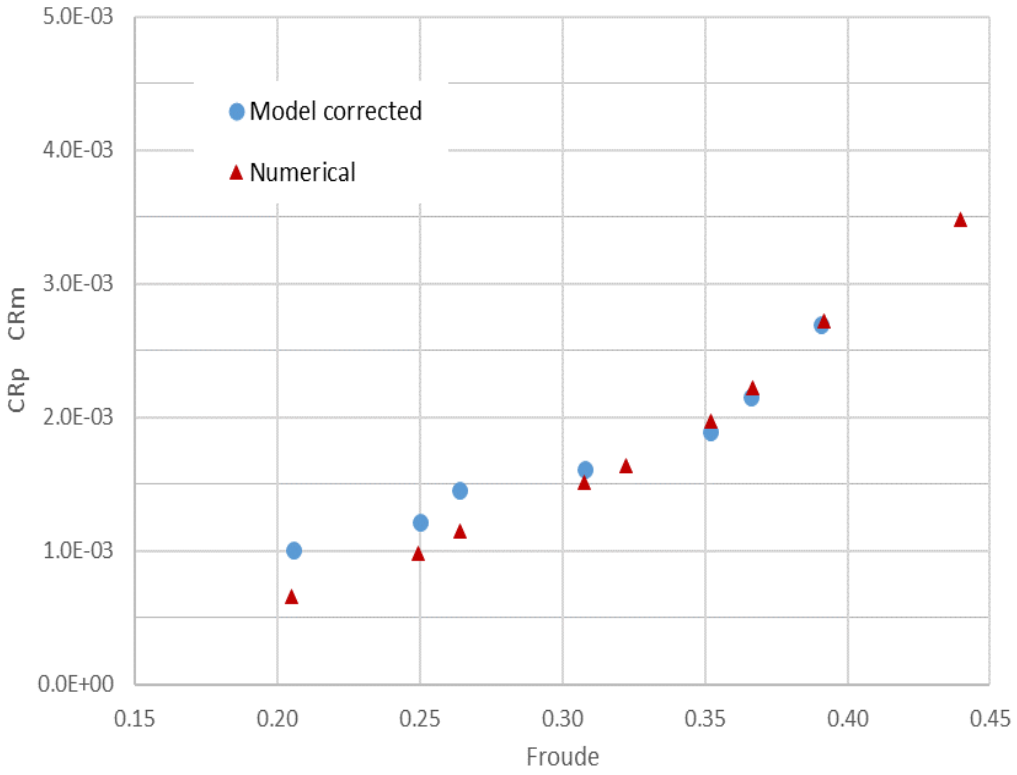

Figure 6-3: Corrected Residuary resistance coefficient vs Froude number

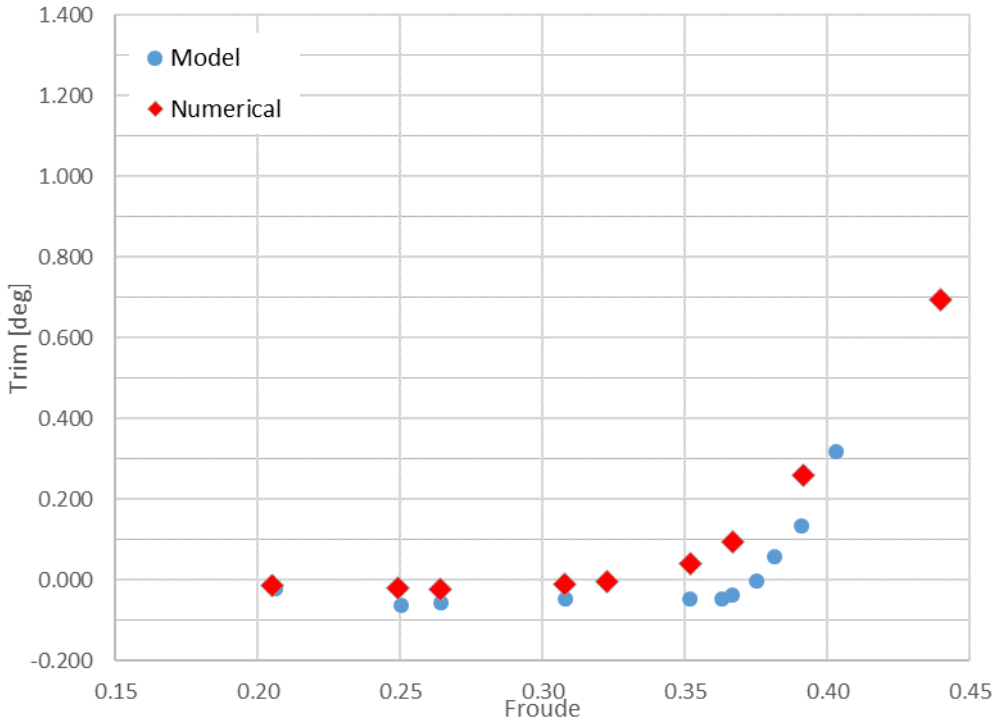

Figure 6-4: Trim (degrees) vs Froude number

From the comparison plots (Figure 5-1 to 5-3), we observe good correspondence for the resistance results obtained with that of the numerical data. From the total resistance co-efficient (Figure 5-1) and the residuary resistance co-efficient (Figure 5-3), we observe that the model resistance values closely match and follow a similar trend as the numerical values.

The friction resistance coefficient for the model tests is calculated using the ITTC-57 formula, which gives us the same results as that observed in Section 3.1.3, where the USNA model data is compared to the numerical OpenFOAM data. The maximum form factor is observed to be 0.07, which is within the acceptable range of 0.15.

Therefore, these plots verify the accuracy of the barehull resistance calculation for the model tests conducted. Figure 5-4 shows good correspondence in the trim measurement (in degrees) between the model and numerical data.

6.3 Verifying barehull model data with USNA data

Comparative plots of the total resistance and total resistance co-efficient vs. Froude number comparing the barehull model test data to the USNA model test data are given in Figure 5-5 and 5-6.

From the comparison of the total resistance (Figure 5-5), we observe that the resistance values measured in the tests conducted at the Virginia Tech towing tank facility closely match the values measured at the USNA, across the tested speed range. The values for the trim measured (Figure 5-7) also seems to follow a similar trend as the USNA data.

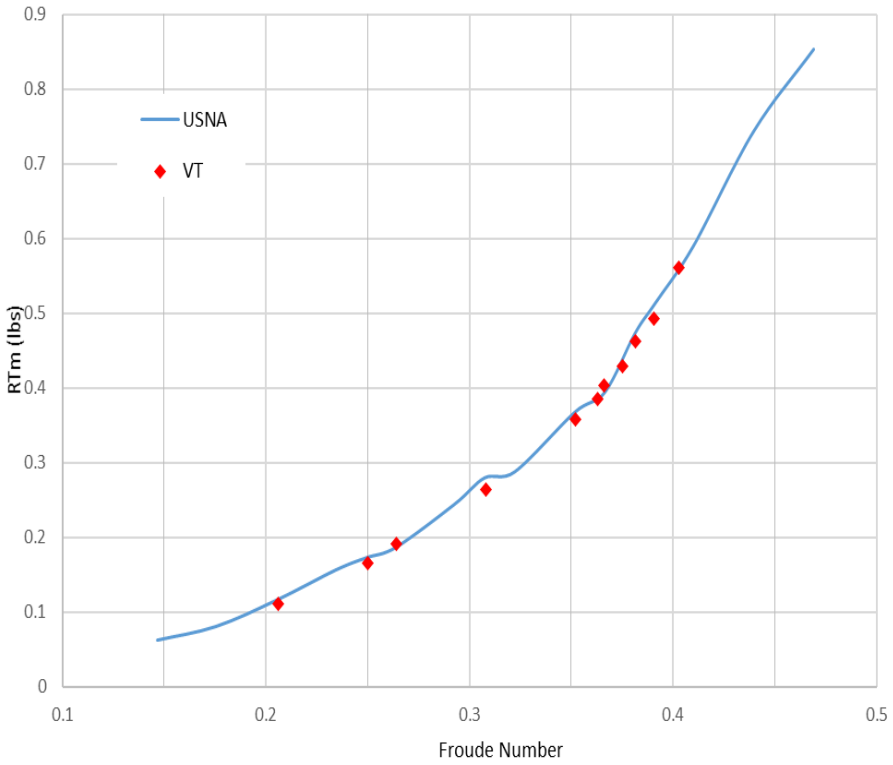

Figure 6-5: Total resistance (lbs) vs Froude number

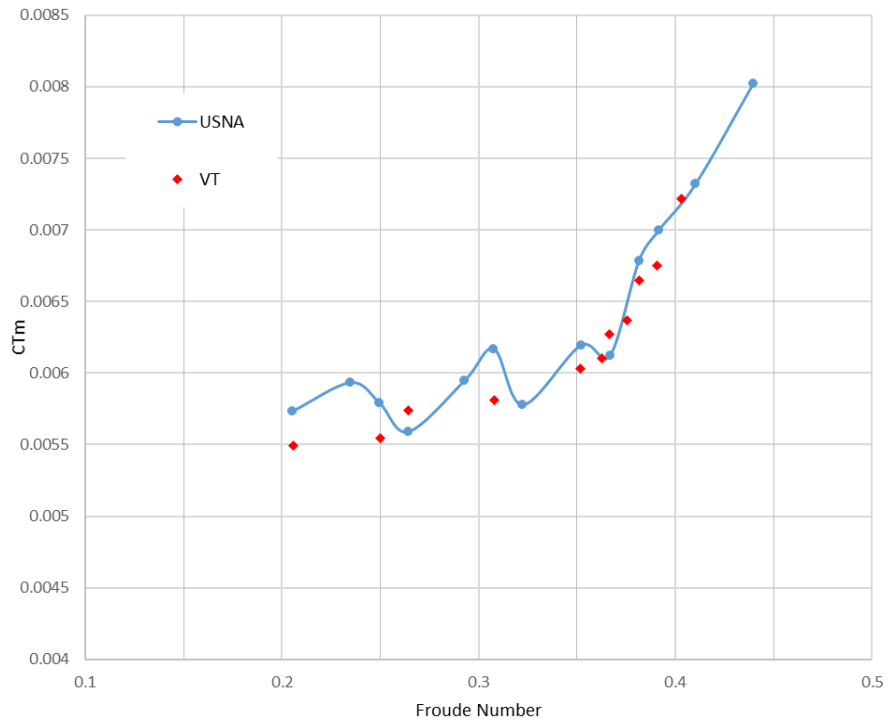

Figure 6-6: Total resistance coefficient vs Froude number

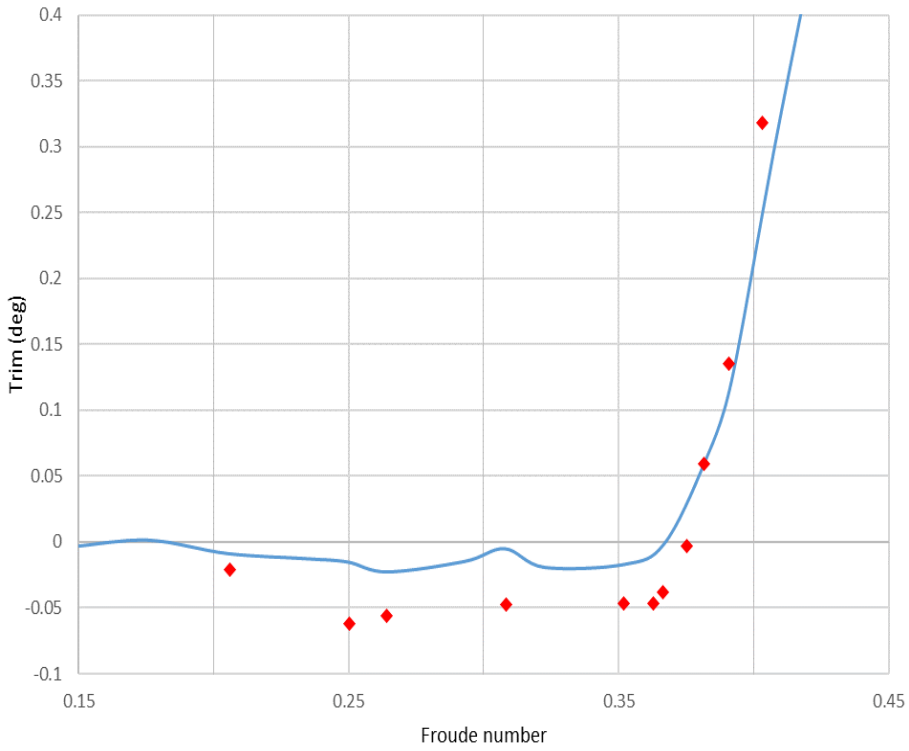

Figure 6-7: Trim (degrees) vs Froude number

6.4 Uncertainty in model tests

For the Virginia Tech experimental model tests, multiple runs were conducted at each speed to check the accuracy of the results. After each run, the tank was left to rest for 15-20 minutes in order to ensure that the water in the tank would settle down and that there were no turbulent vortices in the tank when the tests were conducted.

A minimum of 3 tests were conducted at each speed, and some uncertainty was observed for the resistance and sinkage results of the model tests. The standard deviation observed in the repeated runs was calculated and plotted to observe the uncertainty in the results.

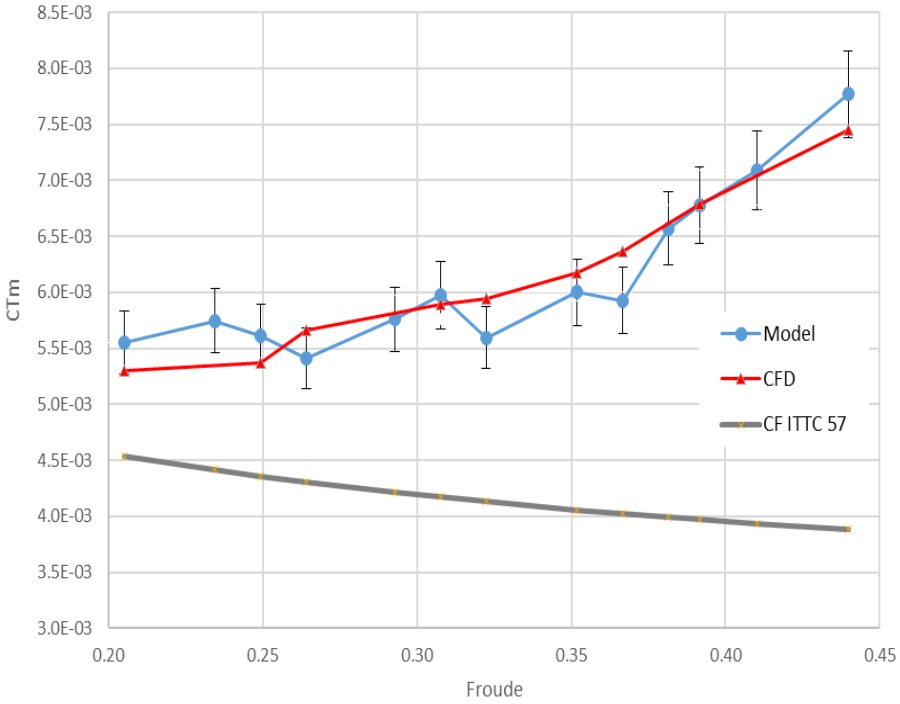

Figure 6-8: Uncertainty in Total resistance of model tests

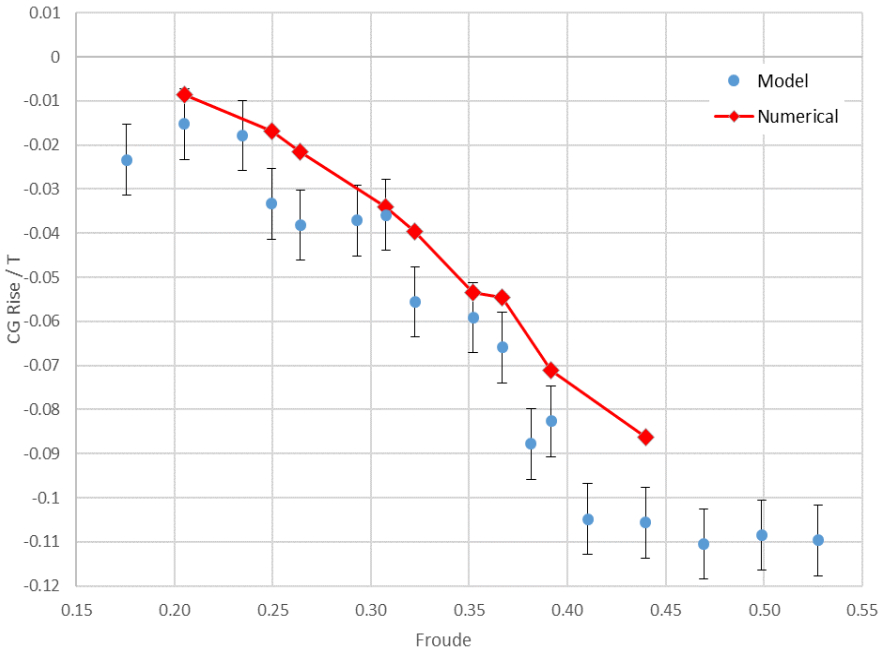

Figure 6-9: Uncertainty in sinkage of model tests

6.5 Interceptor

For the interceptor model tests, the interceptors were prepared such that the height and span of the interceptors matched the dimensions used during the simulations in OpenFOAM. Therefore four different interceptors were made using two different heights of 0.0025 m and 0.00375 m, and two different spans of 0.07747 m and 0.05164 m. The interceptors used are listed in Table 5.1.

Table 6-1: Dimensions of the Interceptors

Interceptor No.	Type	Height (m)	Span (m)
1	Large Height, Large Span (LH LS)	0.00375	0.07747
2	Large Height, Small Span (LH SS)	0.00375	0.05164
3	Small Height, Large Span (SH LS)	0.0025	0.07747
4	Small Height, Small Span (SH SS)	0.0025	0.05164

The interceptors were made using 1/16 Aluminium sheets as can be seen in Figure 5-8. The interceptors were attached in a way so as to ensure that the interceptor plate would not move or bend due to the pressure of the water even at high speeds.

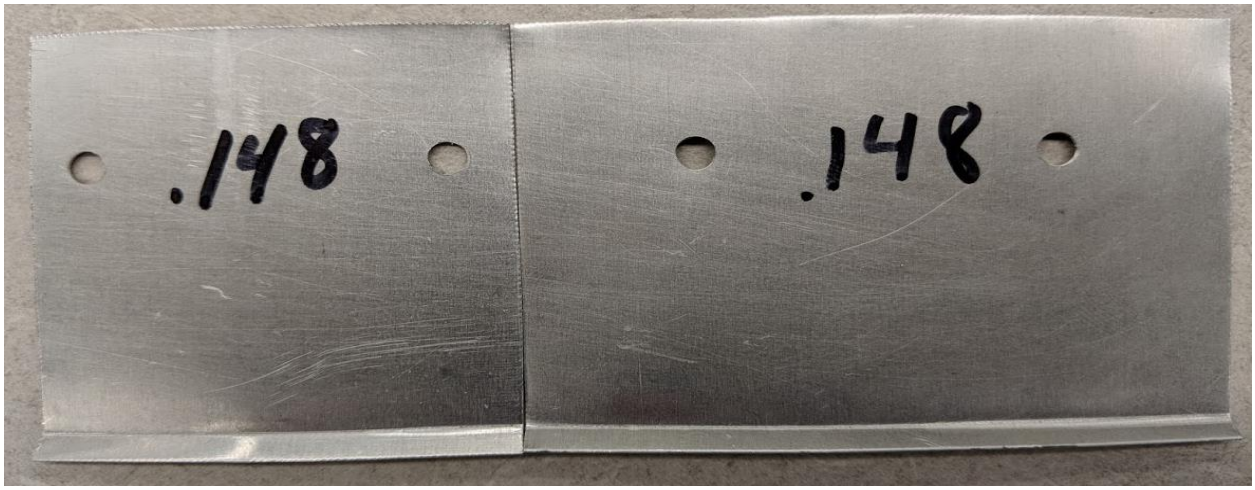

Figure 6-10: Interceptor plates showing the difference in height (top) and span (bottom)

6.6 Interceptor tests validation with CFD

Initially to ensure the accuracy of the resistance measured during the model tests with the interceptor, the results are validated with the OpenFOAM interceptor results. The interceptor data used for validation is Interceptor 1 (Large height and large span).

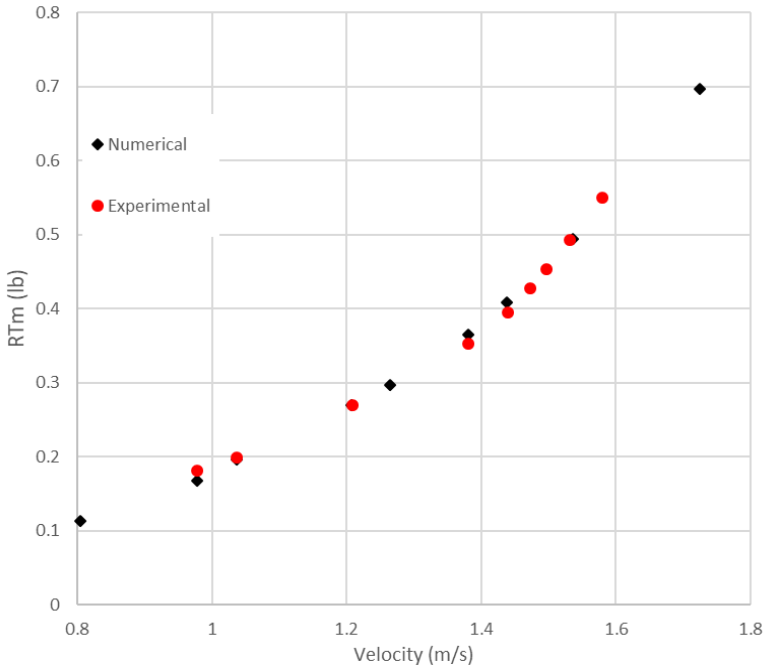

Figure 6-11: Validation of Total resistance (lb) for Interceptor 1 numerical and experimental results

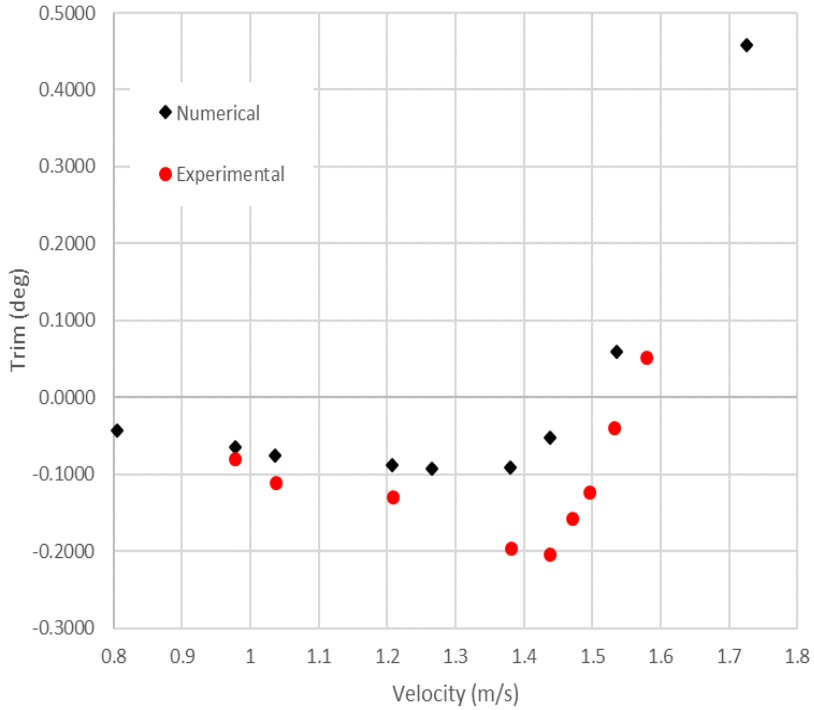

Figure 6-12: Validation of Trim (deg) for Interceptor 1 numerical and experimental results

From Figure 6-9, the Total resistance for the numerical simulations (OpenFOAM) and the experimental tests (model towing tank tests), seem to have agreement across the tested speed range. The trim results (Figure 6-10) on the other hand vary significantly. Multiple model test runs were conducted at each speed and it was observed that there was a high degree of uncertainty in the readings between each run. Since the values for these readings are of a very small magnitude, this uncertainty could be a result of the tolerance of the instrumentation.

6.7 Investigation of interceptor effects

The results of the different geometries of the interceptors are plotted below.

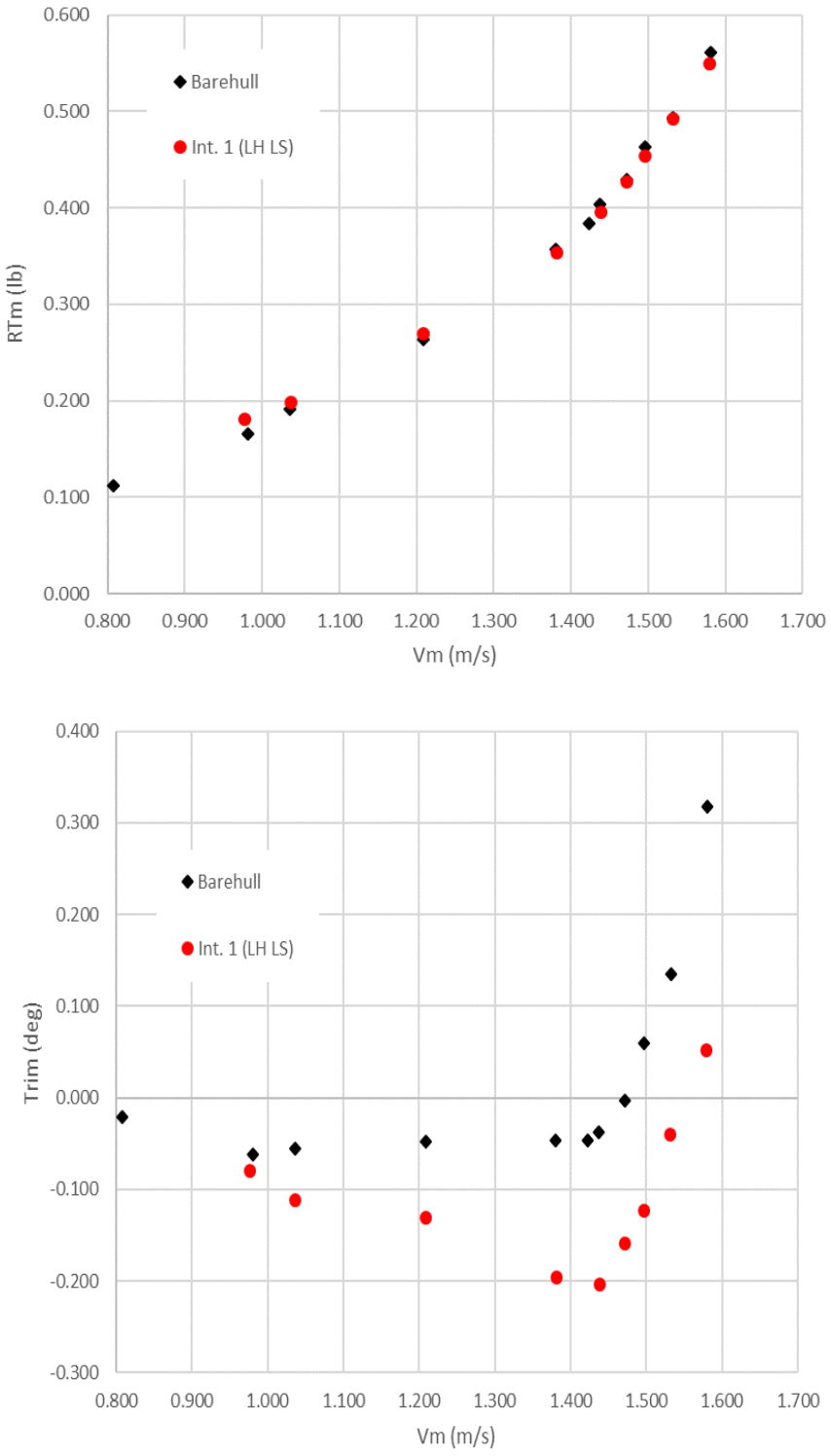

Figure 6-13: Total resistance (top) and Trim (bottom) comparison for Interceptor 1 (LH LS) with barehull

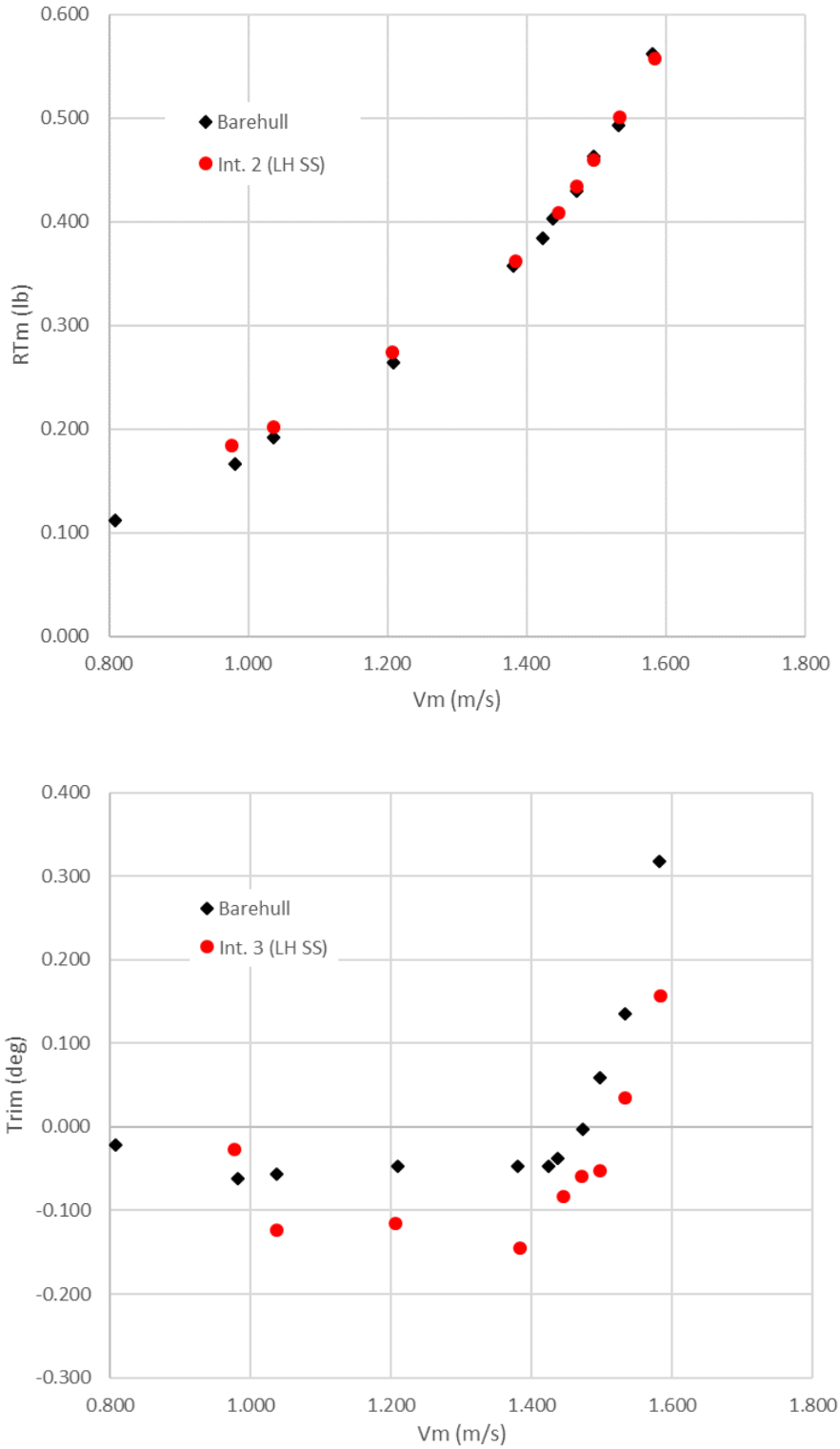

Figure 6-14: Total resistance (top) and Trim (bottom) comparison for Interceptor 2 (LH SS) with barehull

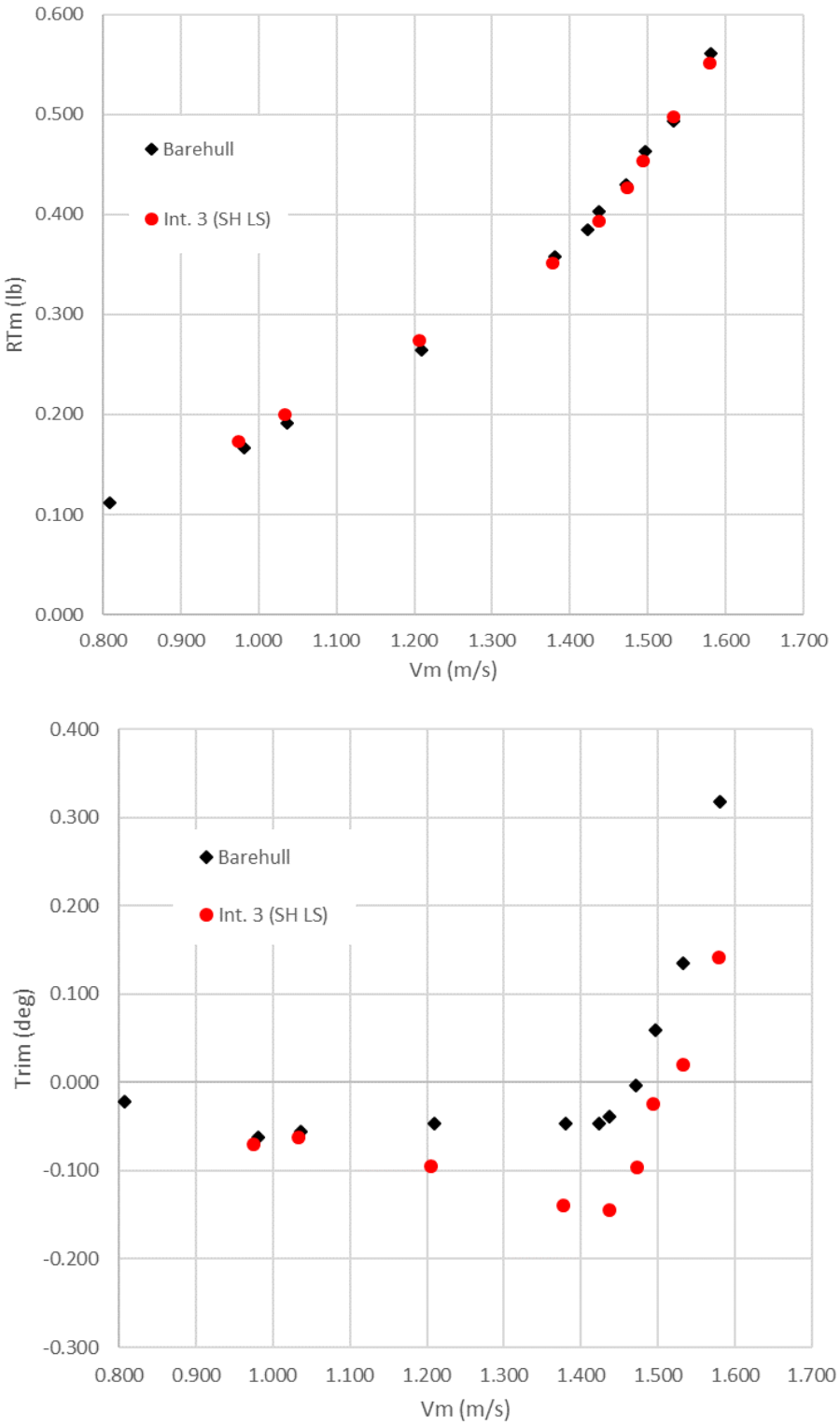

Figure 6-15: Total resistance (top) and Trim (bottom) comparison for Interceptor 3 (SH LS) with barehull

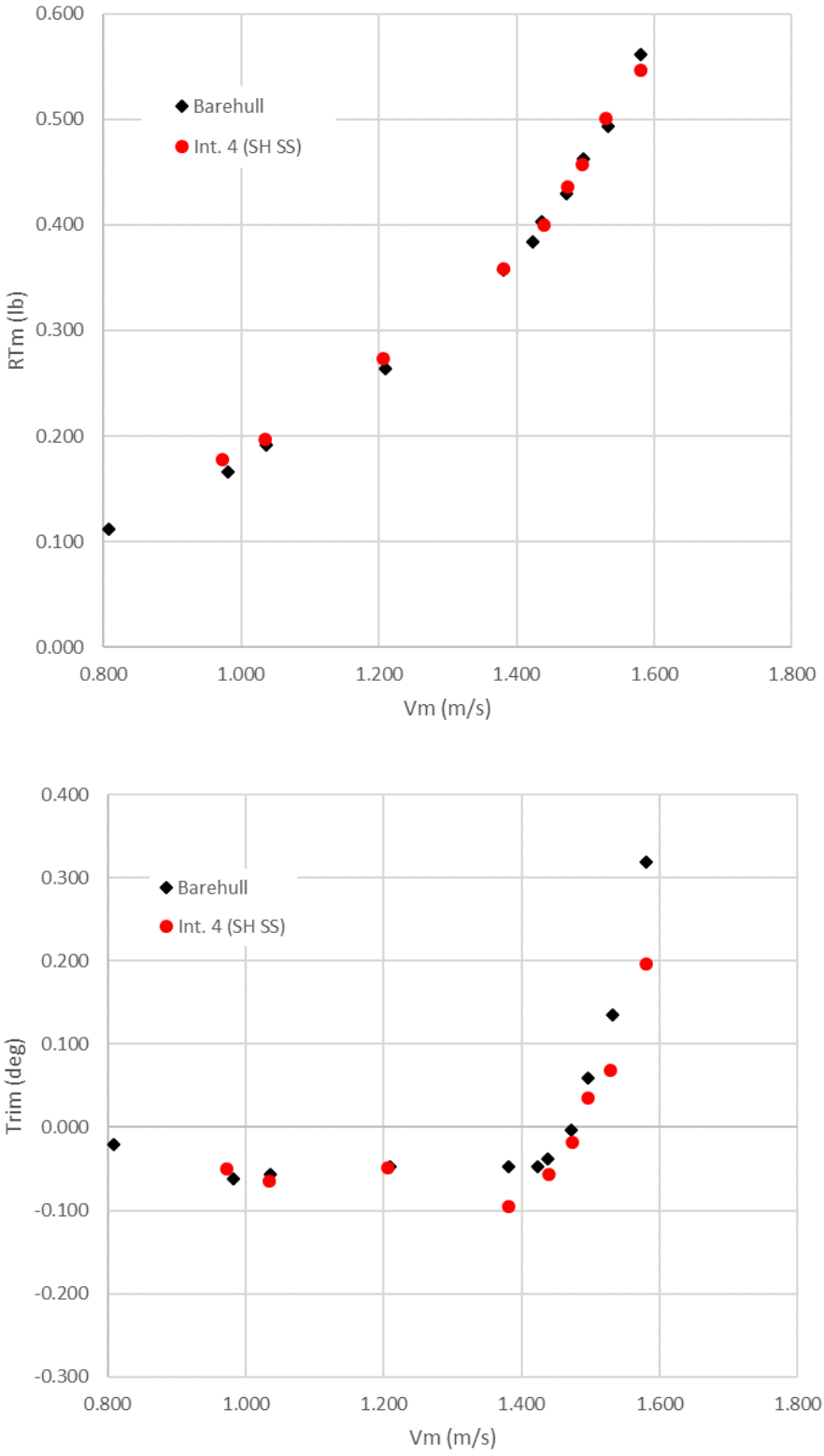

Figure 6-16: Total resistance (top) and Trim (bottom) comparison for Interceptor 4 (SH SS) with barehull

The total resistance plots for the interceptors, as expected, show an increase in total resistance at low speeds, whereas there is a decrease at higher speeds. There is also a reduction in trim across the speed range with the use of the different geometries of the interceptor. The performance improvement for Interceptor 1 (LH LS) is found to be the most significant.

CHAPTER 7

CONCLUSION

A series of high fidelity numerical simulation with OpenFOAM is used to characterize the hydrodynamic properties of a transom mounted interceptor. A numerical bare hull FFG-7 model is validated using the model test results obtained at the United States Naval Academy Hydromechanics Laboratory (NAHL).

The interceptor is found to increase the total resistance at low speeds, while decreasing the resistance at high speeds. This result is consistent with the findings in previous research conducted. The high pressure region created by the interceptor corrects the running trim of the hull, as it resolves the large negative pressure that is observed in the bare hull.

The highest drag reduction is observed at a speed of 0.392 Fr, where the total resistance reduces by 3.76% and the trim is reduced by 0.2 degrees. The improvement in the performance at high speeds can be attributed to the reduced trim and sinkage which decreases the wetted surface area of the hull, thereby significantly reducing the shear resistance.

The calculated EHP for a bare hull prototype at 0.392 Fr is 15,250 hp, whereas with an interceptor the EHP is calculated to be 14,390 hp. This 5.6% decrease suggests that the usage of interceptors at high speeds would be very economically beneficial and would result in a considerable amount of emission and fuel being saved. Numerical studies for various geometries of the interceptor are conducted by varying the height and span of the interceptors.

Experimental model tests with transom mounted interceptors are conducted at Virginia Tech towing tank facility. The experimental results are used to verify the

numerical results from OpenFOAM, which further suggests a performance improvement in the self-propulsion while using the transom mounted interceptor.

Bibliography

[1] B. F.C., "Comment and Discussion of technical session papers," *Naval Engineers Journal,* p. 91, May 1987.

[2] J. J. e. a. Kehoe, "U.S. and Foreign Hull Form, Machinery, and Structure Design Practices.," *Naval Engineers Journal,* Nov. 1983.

[3] C. D. L. G. Karafiath G., "Stern Wedges and Stern Flaps for Improved Powering - U.S. Navy Experience.," *SNAME Transactions,* vol. 107, pp. 67-99, 1999.

[4] J. a. B. H. Zseleczky, "FFG-7 Model Powering Test With and Without a Stern Wedge," *U.S. Naval Academy Report,* 1984.

[5] D. Cusanelli, "Stern Flaps - A Chronicle of Success at Sea (1989-2002)," *SNAME Innovations in Marine Transportation,* May 2002.

[6] D. K. G. Cusanelli, "Hydrodynamic Energy Saving Enhancements for DDG 51 Class Ships.," in *ASNE Day 2012*, Crystal City, Arlington, VA, 2012.

[7] B. S., "Hydrodynamic Analysis of Interceptors with CFD Methods.," in *FAST 2003, 7th Int. Conference on Fast Sea Transportation,* 2003.

[8] K. v. O. p. M. N. v. O. P. G. Z. K. S. Uithof, "An Update on the Development of the Hull Vane," in *International Conference on High Performance Marine Vehicles,* 2014.

[9] B. S. Molini A., "Hydrodynamics of Interceptors: A Fundamental Study.," in *International Conference on Maritime Research and Transportation, ICMRT 2005.*, Ischia (Italy), 2005.

[10] C. C. A.H. Day, "An experimental study of interceptors for drag reduction on high-performance sailing yachts," *Ocean Engineering 38,* 2011.

[11] B. S. B. W. White J., "Effect of Inverted Bow on the Hydrodynamic Performance of Navy Combatant Hull Forms.," *SNAME Transactions 2016.,* 2016.

[12] I. a. D. S. C. William L. Cave, "Effect of Stern Flaps on Powering Performance of the FFG-7.," *Marine Technology,* vol. 30, Jan. 1993.

[13] a. H. J. Tsai J., "Study On The Effect Of Interceptor On High Speed Craft," *Journal of The Society of Naval Architects and Marine Engineering,* vol. 22, pp. 95- 101, 2003.

[14] F. Menter, "Two-equation eddy-viscosity turbulence models for engineering applications.," *AIAA Journal*, August 1994.

[15] G. F. S. Karafiath, "The effect of stern wedges on ship powering performance," *Naval Eng. Journal*, pp. 27-38, 1987.